

ABSTRACT

LEE, SUGJOON. Long-Term Performance Assessment of Asphalt Concrete Pavements Using the Third Scale Model Mobile Loading Simulator and Fiber Reinforced Asphalt Concrete (Under the direction of Dr. Y. R. Kim, Dr. R. H. Borden, and Dr. J. P. Rust).

Long-term pavement performance such as fatigue and rutting is investigated using the third scale Model Mobile Loading Simulator (MMLS3). Prediction algorithms are proposed that can account for the loading rate of MMLS3 and temperature variation along the depth of pavement. In a separate study, influence of fibers on the fatigue cracking resistance is studied.

In this research, laboratory asphalt pavement construction technique, sensor instrumentation, and test conditions are evaluated to establish effective test protocols for fatigue cracking and rutting evaluation using the MMLS3. The investigated results present that: (1) the MMLS3 with wheel wandering system can induce the realistic fatigue (alligator pattern) cracks; (2) using wavelet correlation method (WCM), fatigue damage growth and microdamage healing are observed; (3) the algorithm for the fatigue life prediction of laboratory pavement is established using the indirect tension testing program and linear cumulative damage theory; (4) the MMLS3 performs a rapid assessment of the rutting potential under controlled conditions; (5) the predictive algorithm predicts rutting performance of asphalt pavements loaded by the MMLS3 using the repetitive cyclic triaxial compression testing program.

It was found that fiber inclusion can improve the mechanical properties of asphalt concrete. Single nylon fiber pullout test was used to investigate debonding and pulling

behavior. As for indirect tension strength tests, asphalt concrete containing nylon fibers showed the potential of improving fatigue cracking resistance by an increase of the fracture energy.

**LONG-TERM PERFORMANCE ASSESSMENT
OF ASPHALT CONCRETE PAVEMENTS USING
THE THIRD SCALE MODEL MOBILE LOADING SIMULATOR
AND FIBER REINFORCED ASPHALT CONCRETE**

by

SUGJOON LEE

A dissertation submitted to the Graduate Faculty of
North Carolina State University
in partial fulfillment of the
requirements for the Degree of
Doctor of Philosophy

**DEPARTMENTS OF CIVIL ENGINEERING
AND
FIBER AND POLYMER SCIENCE**

North Carolina State University

2003

APPROVED BY:

Dr. Y. R. Kim

Co-Chair of Advisory Committee
in Department of Civil Engineering

Dr. J. P. Rust

Co-Chair of Advisory Committee
in Fiber and Polymer Science

Dr. R. H. Borden

Co-Chair of Advisory Committee
in Department of Civil Engineering

Dr. H. Hamouda

Dr. M. N. Guddati

DEDICATION

With love and thanks

To my family

BIOGRAPHY

Sugjoon “Joon” Lee was born in South Korea on January 1967. Once he graduated Yong-san high school in Seoul, he began studying Textile Engineering in March of 1986. As an undergraduate at Hanyang University, Korea, he participated in college mission activities at each of the following organizations: Campus Crusade for Christ and Youth With A Mission. He received a Bachelor of Science degree in Textile Engineering from Hanyang University in February 1993. In May 1995, he was lucky to get married with Moonjung, his lovely wife, with God’s blessing before his graduate study in abroad. In January of 1996, he began graduate studies in Textile Engineering at North Carolina State University in Raleigh, NC, where he received a Master of Science degree in December 1998, in the area of “fabrication and development for on-line yarn mass measurement system”. In 1999, he got his precious son, Jaewon, in February and then he entered the Ph.D. program in civil engineering with the aid of his advisor, Dr. Kim, in May. Three years later, he was approved to pursue co-major Ph.D. in Fiber and Polymer Science (FPS) as well as civil engineering from graduate school. While he has been serving as a research assistant, he was able to complete his course work and conduct heavy-duty experimental and analytical research. Sugjoon finally earned his Doctoral degree in Civil Engineering and Fiber Polymer Science through an 8-year’s journey of graduate life at North Carolina State University on December 17th 2003.

ACKNOWLEDGEMENTS

I would like to express my appreciation to my advisor, Dr. Y. Richard Kim, of civil engineering for his support and direction for this research work. I would also like to thank my co-chair, Dr. Jon P. Rust, of Fiber and Polymer Science. Also, my special appreciation should be delivered to Dr. Roy H. Borden because of his endless prayer and support as a co-chair of civil engineering as well as a spiritual father. My appreciation also goes to Dr. H. Hamouda and Dr. M. N. Guddati for serving on my committee. Several friends have been helpful throughout the various stages of this work, whether through assistance of technical issues or simply with helpful cooperation on the process of getting a doctorate. In particular, I would like to acknowledge Youngguk Seo, Jusang Lee, Shane Underwood, Mark King, Claire Kohlmann, Ghassan Chehab, Jerry Atkinson, William Dunleavy, and Renee Howard.

I do not know how to express my bottomless and heartfelt gratitude to my family. I appreciate the constant support of beloved parents, dad, mom, father-in-law, and mother-in-law. Above all, I would like to express my sincere appreciation to my lovely wife, Moonjung, for her incredible patience and unchanging trust and to Jaewon, my son. He is my stress-reliever and fullness of joy.

All thanks and praise are due to God the most gracious the most righteous.

“Put your hope in God, for I will yet praise him, my Savior and my God”

TABLE OF CONTENTS

LIST OF TABLES.....	ix
LIST OF FIGURES.....	xi
CHAPTER	
1. INTRODUCTION.....	1
1.1 Long-Term Pavement Distress Evaluation.....	1
1.2 Research Objectives.....	2
2. THE THIRD SCALE MODEL MOBILE LOADING SIMULATOR.....	4
2.1 Introduction.....	4
2.2 Background.....	4
2.2.1 Wheel Trafficking Devices.....	4
2.2.2 Dimensional Analysis.....	6
2.3 Principal Features of The MMLS3.....	7
2.4 Characterization of MMLS3 Dynamic Wheel Loads.....	9
3. EXPERIMENTAL TESTING PROGRAM.....	12
3.1 Introduction.....	12
3.2 Material tested.....	12
3.3 MMLS3 Experimental Procedures.....	15
3.3.1 Laboratory Preparation.....	16
3.3.2 Model Pavement Preparation.....	17
3.3.3 MMLS3 Testing Description.....	20
3.4 FRAC Experimental Procedures.....	22
3.4.1 Single Fiber Pullout Test.....	22
3.4.2 Indirect Tension Strength Test (IDST).....	24
3.5 Instrumentation Considerations.....	24
3.6 Summary.....	26

4. STRESS WAVE ANALYSIS USING WAVELET CORRELATION	
METHOD.....	27
4.1 Introduction.....	27
4.2. Background.....	28
4.2.1 Surface Wave Propagation.....	28
4.2.2 Short Kernel Method (SKM).....	29
4.3 Wavelet Correlation Method (WCM).....	30
4.3.1 Wavelet Construction.....	30
4.3.2 Implementation of WCM.....	32
4.3.3 Evaluation of WCM Accuracy with Synthetic Data.....	35
4.3.4 Strength and Weakness of Wavelet Correlation Method.....	53
4.4 Testing Setup and Instrumentation.....	54
4.5 Components of Stress Wave Analysis.....	56
4.5.1 Dispersion Analysis.....	56
4.5.2 Representative Frequency Determination.....	57
4.5.3 Microdamage Healing.....	60
4.5.4 Nondestructive Stiffness Evaluation on Thin Pavement.....	63
4.6 Summary.....	65
5. FATIGUE PERFORMANCE INVESTIGATION.....	66
5.1 Introduction.....	66
5.2 Background.....	68
5.2.1 Asphalt Institute Fatigue Life Prediction Model.....	68
5.2.2 Indirect Tension Testing (IDT).....	69
5.3 Fatigue Laboratory Pavement Construction Development.....	70
5.3.1 Evolution of Pavement System for the MMLS3.....	70
5.3.2 Structural Analysis for Fatigue Pavement using Multi-Layer Elastic Program.....	73
5.4 Evaluation of Fatigue Performance.....	76
5.4.1 Analysis of Pavement Responses.....	76
5.4.2 Indirect Tension Fatigue Tests (IDFT).....	83

5.4.3 Cumulative Damage Analysis.....	86
5.4.4 Fatigue Life Prediction Algorithm using IDT Testing Program.....	91
5.5 Summary.....	102
6. RUTTING PERFORMANCE INVESTIGATION.....	103
6.1 Introduction.....	103
6.2 Permanent Deformation Empirical Model.....	104
6.3 Rutting Slab Construction Development.....	105
6.4 Evaluation of Rutting Performance.....	106
6.4.1 Pavement Temperature Control.....	106
6.4.2 Analysis of Rutting Profiles.....	108
6.4.3 Pavement Service Life Analysis.....	118
6.5 Permanent Deformation Prediction Algorithm.....	120
6.6 Summary.....	133
7. FIBER REINFORCEMENT ASPHALT CONCRETE (FRAC).....	134
7.1 Introduction.....	134
7.2 Background.....	135
7.3 Mechanical Properties of Fiber-Reinforcement Cement.....	140
7.3.1 Fiber-Cement Interaction Mechanism: Stress Transfer.....	140
7.3.2 Fiber Length Effect.....	142
7.3.3 Critical Fiber Volume Fraction.....	142
7.4 Fiber-Asphalt Pullout Test.....	143
7.4.1 Specimen Preparation.....	143
7.4.2 Test Configurations.....	144
7.4.3 Pullout Test Results.....	146
7.5 Fiber Reinforced Asphalt Concrete Strength Tests.....	150
7.5.1 Specimen Preparation.....	150
7.5.2 Indirect Tension Strength Test (IDST).....	151
7.5.3 Test results.....	152
7.6 Summary.....	160

8. CONCLUSIONS AND RECOMMENDATIONS FOR THE FURTHER	
RESEARCH.....	161
8.1 Conclusions.....	161
8.2 Recommendations for the further research.....	164
REFERENCES.....	166
APPENDICES.....	166
Appendix A	
Impact Method and Generated Frequency Ranges for Stress Wave	
.....	171
Appendix B	
Dynamic Modulus Test.....	172
Appendix C	
Fatigue Failure Analysis.....	175
Appendix C.1 Cumulative Damage Analysis.....	175
Appendix C.2 Mathematical Expression of N_f For MMLS3	
System.....	178
Appendix C.3 Mathematical Expression of k_3 For MMLS3	
System.....	179
Appendix D	
Permanent Deformation Regression Parameter Determination.....	180

LISTS OF TABLES

Table 3.1	MMLS3 Testing Programs.....	13
Table 3.2	Aggregate Gradations and Asphalt Content for the Four Mixes Used in this Study.....	14
Table 3.3	FRAC Testing Programs.....	23
Table 4.1	Elements of Synthetic Waves for Effect of Damage.....	36
Table 4.2	(a) Phase Velocity Calculations for CASE I and II Based on WCM	43
	(b) Phase Velocity Calculations for Cases I and II Based on SKM	43
Table 4.3	Elements of Synthetic Wave for Nearby Frequency Effect.....	44
Table 4.4	(a) Phase Velocity Calculations for CASE III and IV Based on WCM	52
	(b) Phase Velocity Calculations for Cases III and IV Based on SKM	52
Table 5.1	Fatigue Life Analysis.....	78
Table 5.2	IDT Fatigue Testing Results.....	86
Table 5.3	Pavement Failure Prediction using Measured Initial Tensile Strain	90
Table 5.4	Pavement Failure Prediction using Measured Dynamic Modulus	90
Table 5.5	Uniaxial Dynamic Moduli.....	95
Table 5.6	Determination of N_f Based on Tensile Strain Profiles.....	97
Table 5.7	Regression Coefficients, k_1 and k_2 , Determination for IDT specimen Using I19-C-A Mixtures.....	98
Table 5.8	Summary of Cumulative Damage Analysis Using Eq. 5.14.....	100
Table 5.9	Values of k_3 for the Fatigue Model.....	101
Table 6.1	Analysis of Permanent Deformation for RI-1 and RI-2 Pavements	113
Table 6.2	Structural Deformation Results.....	119

Table 6.3	Loading Frequencies at Measuring Depths.....	116
Table 6.4	Dynamic Modulus Computation Using Uniaxial Testing Program	126
Table 6.5	Computation Method for Reduced Temperatures at 10 Hz Loading Equivalent to Temperatures at Different Loading Frequencies	127
Table 6.6	Representative Resilient Strain Values of ϵ_{RM} and ϵ_{RP}	128
Table 6.7	Regression Constants for Temperatures and Air Void Content.....	129
Table 6.8	Results of Rut Depths (RD) Using Prediction Algorithm.....	132
Table 7.1	Pullout Testing Results.....	149
Table 7.2	IDST Resulted Data.....	155
Table 7.3	Statistical Analysis for Fiber Effect.....	156
Table A.1	Generated Frequency Ranges.....	171
Table C.1	8.9% Cumulative Damage Analysis Chart.....	175
Table C.2	9.8% Cumulative Damage Analysis Chart.....	176
Table C.3	10.4% Cumulative Damage Analysis Chart.....	176
Table C.4	11.1% Cumulative Damage Analysis Chart.....	177

LISTS OF FIGURES

Figure 2.1	MMLS3 Schematics.....	8
Figure 2.2	Flexiforce [®] Pressure Sensor and Voltage Excitation System.....	10
Figure 2.3	MMLS3 Static Load Distribution.....	10
Figure 2.4	Measured Data for MMLS3 Dynamic Loading.....	11
Figure 3.1	Testing Facility.....	16
Figure 3.2	Schematic of Layered Structures and Instrumentation for Fatigue Pavement Testing.....	18
Figure 3.3	Schematic of Layered Structures and Instrumentation for Rutting Pavement.....	19
Figure 3.4	Behavior of Load Measurement under Controlled Ram Displacement	24
Figure 4.1	Sample Wavelet Kernel.....	31
Figure 4.2	Illustration of WCM Transformation Implementation.....	33
Figure 4.3	Power Spectrum of: (a) Actual Surface Wave and (b) WCM Transformed Wave.....	34
Figure 4.4	(a) Component Waves for CASE I and CASE II.....	37
	(b) Composite Waves for CASE I and CASE II.....	38
	(c) Frequency Analysis for Case I and Case II.....	38
Figure 4.5	(a) Case I: WCM Transformed Waves.....	39
	(b) Case I: SKM Transformed Waves.....	40
Figure 4.6	(a) Case II: WCM Transformed Waves.....	41
	(b) Case II: SKM Transformed Waves.....	42
Figure 4.7	(a) Component and Composite Waves for CASE III.....	45
	(b) Component and Composite Waves for CASE IV.....	46
	(c) Frequency Analysis for Case III and IV.....	47
Figure 4.8	(a) Case III: WCM Transformed.....	48
	(b) Case III: SKM Transformed.....	49
Figure 4.9	(a) Case IV: WCM Transformed Waves.....	50
	(b) Case IV: SKM Transformed Waves.....	51

Figure 4.10	Schematic Diagram of Stress Wave Experimental Setup.....	55
Figure 4.11	Dispersion Curve by WCM for RI-1 Pavement.....	58
Figure 4.12	Dispersion Curve in Wavelength and Phase Velocity Relationship for RI-1 Pavement.....	58
Figure 4.13	Changes in Phase Velocity during Fatigue Loading for I19C-A Pavement (8.7% AV Section)	61
Figure 4.14	(a) Changes of Healing Index along Rest Period at different Load Levels for RI-1 Pavement.....	62
	(b) Slope Parameter from Regression Analysis for Healing Indices and Cumulative Crack Length Profile as a Function of Wheel Applications for RI-1 Pavement.....	62
Figure 4.15	Phase Velocities versus Cracking.....	64
Figure 4.16	Phase Velocity (No Rest Period) and Cumulative Surface Crack Length as a Function of Number of Wheel Applications	65
Figure 5.1	Schematics of the IDT.....	69
Figure 5.2	Overview of Constructed Pavements.....	72
Figure 5.3	Pavement Profiles for Structural Analysis.....	74
Figure 5.4	Compressive Stresses along Depth of Pavements at Center of Wheel Path.....	75
Figure 5.5	Tensile Strain Profiles at Different Air Voids Using I19C-A Mix...	77
Figure 5.6	Example of Determination in Fatigue Life.....	77
Figure 5.7	Relationships between Air Void Contents and Number of Wheel Applications at Failure.....	78
Figure 5.8	Crack Propagation at Different Air Void Contents Using I19C-A Mix.....	80
Figure 5.9	Fatigue Alligator Cracking Pattern after 250,000 Wheel Applications on the surface of RI-1 Pavement.....	81
Figure 5.10	Fatigue Alligator Cracking Pattern in RI-1 Pavement.....	82
Figure 5.11	Initial Horizontal (Tensile) Strain versus Number of Load Repetitions.....	83

Figure 5.12	Fatigue Life Profiles Using RI-1 Mix.....	85
Figure 5.13	Regression Analysis for Coefficients, k_1 and k_2 , of Fatigue Life Prediction Model.....	85
Figure 5.14	Schematics of Lateral Wheel Wandering.....	88
Figure 5.15	Framework for Prediction of Fatigue Failure.....	91
Figure 5.16	Reduction of Air Void Contents Using Field Cores.....	94
Figure 5.17	Loading Frequency Variation along Depths.....	95
Figure 5.18	Correction of N_{fh} by Excluding Healing Effect.....	96
Figure 5.19	Regression Analysis for k_1 and k_2 in Fatigue Model.....	99
Figure 5.20	Determination of k_3 as a Function of Air Void Content.....	101
Figure 6.1	Temperature Profile in RI-1 Pavement.....	107
Figure 6.2	Lateral Rutting Profile for RI-1 Slab.....	109
Figure 6.3	Rut Depth Growth Using Reference Method for RI-1 Slab.....	110
Figure 6.4	Rut Depth Growth for RI-2 Slab at 40°C.....	111
Figure 6.5	Rut Depth Growth for RI-2 Slab at 55°C.....	112
Figure 6.6	Permanent Strain Growth as a Function of Temperature from RI1 Slab	115
Figure 6.7	Permanent Strain Growth as a Function of Air Void Content from I19C Slab.....	116
Figure 6.8	Permanent Strain Model Coefficients as a Function of Air Void Contents for I19C-A Slab.....	116
Figure 6.9	Aging Effect on I19C pavements.....	118
Figure 6.10	Layer Characteristics of I19C-A Pavement for Permanent Deformation Prediction Based on Temperature Variation on Half Space.....	121
Figure 6.11	Framework for Prediction of Rut Depth.....	122
Figure 6.12	Loading Frequency Variation along Depths.....	125
Figure 6.13	Temperature Variation in Depth of Pavement for I19C-A.....	125
Figure 6.14	Comparison of Measured / Predicted Rut Depths for 3-layer Structure at Air Void Contents.....	131
Figure 7.1	Illustration of Tufted Carpet Structure.....	137

Figure 7.2	Pull-out Geometry to Simulate Fiber-Matrix Interaction.....	141
Figure 7.3	Pull-out Displacement Curve with a Transition from Elastic Stress Transfer to a Constant Frictional Stress Transfer.....	141
Figure 7.4	Pullout Testing Device.....	145
Figure 7.5	Nylon Pullout Test Setup.....	146
Figure 7.6	Illustration of Relationships between Pullout Load and Fiber Extension Using 6 mm Embedded Fiber Tested.....	147
Figure 7.7	Embedded Fiber Length versus Pullout Load.....	148
Figure 7.8	IDST Setup.....	151
Figure 7.9	Tensile Stress-Strain Curve for a Fresh and a Fiber Composite (12 mm L_f , 1% V_f) Specimen.....	153
Figure 7.10	Schematic for Work Potential Theory.....	153
Figure 7.11	Total (or Fracture) Energy of Fiber Composite Asphalt Concrete...	157
Figure 7.12	Dissipated Energy of Fiber Composite Asphalt Concrete.....	157
Figure 7.13	Strain Energy of Fiber Composite Asphalt Concrete.....	158
Figure 7.14	Relationships between Field Performance and Energy.....	159
Figure 7.15	Maximum Tensile Stress of Fiber Composite Asphalt Concrete....	160
Figure B.1	Haversine Loading Pattern for Dynamic Modulus Test.....	172
Figure B.2	Complex Modulus Schematic Diagram.....	174
Figure D.1	Relationships between Temperatures and Parameters at Air Void Contents.....	181

CHAPTER 1

INTRODUCTION

1.1 LONG-TERM PAVEMENT DISTRESS EVALUATION

An asphalt-aggregate mixture is a viscoelastic material whose deformation behavior is one of the most significant factors contributing to common load-related distresses, such as rutting (permanent deformation) and fatigue cracking, in asphalt concrete pavement systems. Therefore, significant efforts have been made in laboratory characterization of asphalt concrete. Once material models are developed, the predictions from these models need to be transferred to the performance of asphalt parameters in the field. This transfer has been considered difficult due to complex environmental and traffic variations that cannot be adequately represented in the laboratory tests. Therefore, it is sometimes unclear to sort out whether the inaccurate prediction of pavement performance by the laboratory models is due to the problems with the model or the problems in transferring the laboratory data to the field performance. This difficulty can be helped by the Accelerated Pavement Testing (APT).

APT is an increasingly popular area of research in pavement engineering. APT describes a testing process that evaluates the long-term pavement performance in a short period by increasing the damage growth rate. APT also allows specific variables, such as temperature that has a considerable effect on pavement performance but is difficult to regulate in the field, to be controlled directly. With this accelerated capability, the effects of changes within the pavement structure on the performance of the pavement can then be examined in a timely fashion. In addition, information obtained using APT in a controlled

testing environment allows for verification / calibration of pavement response and performance prediction models. This research presents the experience and findings gained at N.C. State using the MMLS3 for fatigue cracking and rutting evaluation of laboratory asphalt pavements.

In order to aid the interpretation of the MMLS3 test results, other tests are performed including stress wave test and indirect tension test for fatigue cracking and the triaxial repetitive permanent deformation test for rutting. Also, pavement responses are measured using sensors embedded in the pavement. These tests are performed on different asphalt pavements, including the ones with varying air void contents to investigate the effect of air void content on the pavement performance. The findings from this study are presented in different chapters. After the details of the MMLS3 are given in chapter 2, the experimental testing program is described in chapter 3. Chapter 4 presents the test and analysis results from the surface wave testing in the fatigue experiments. Findings from the fatigue cracking and rutting evaluation are given in chapter 5 and 6, respectively. Chapter 7 summarizes the work on the fiber reinforced asphalt concrete, which has been done independent from the MMLS3 study. Finally, conclusions and recommendations on fatigue work are presented in chapter 8.

1.2 RESEARCH OBJECTIVES

This study was formulated to investigate the long-term performance of asphalt-aggregate mixtures using the MMLS3 laboratory testing program and to demonstrate the influence of incorporating fibrous composite material. The primary objectives of the proposed research are:

- (1) to refine/develop fatigue and rutting performance testing methods for HMA mixes using the MMLS3;
- (2) to develop the stress wave test and analysis methods to nondestructively monitor damage growth of thin asphalt concrete pavements;
- (3) to develop predictive algorithms for fatigue cracking and rutting under the MMLS3;
- (4) to determine pavement performance as a function of mixture deficiencies in air void content; and
- (5) to investigate the cracking resistance of a polymeric fiber-HMA composite material.

CHAPTER 2

THE THIRD SCALE MODEL MOBILE LOADING SIMULATOR

2.1 INTRODUCTION

The stress conditions in a pavement as a loaded wheel passes are extremely complicated and cannot be precisely replicated in a simple laboratory test on a sample of HMA. Hence it is difficult to accurately predict the pavement performance solely using a laboratory model. In this study, the MMLS3 is used to provide help in bridging this gap. In the following sections, the details of the MMLS3 are described.

2.2 BACKGROUND

2.2.1 WHEEL TRAFFICKING DEVICES

Wheel trafficking devices have been developed to better investigate the effects of a rolling wheel on the pavement and to better understand the cracking phenomenon. Van Dijk (1975) presented a pneumatic wheel-tracking tester. His results included the development of hairline cracks, real cracks, and finally failure of the slab. He also suggested that laboratory controlled-stress tests appear to provide conservative results.

Since then, several full-scale testers have been developed, including The Federal Highway Administration's ALF (Accelerated Loading Facility), The Texas Model Loading Simulator (TxMLS), introduced by Hugo (1990), and the Heavy Vehicle Simulator (HVS) currently used in California (NCHRP synthesis 235, 1996). However, the high initial investment, maintenance costs, and required supplementary laboratory testing provided driving force for development of scaled-down APT devices.

The Model Mobile Loading Simulator (MMLS) was designed to apply scaled loads to a scaled pavement structure and to complement full-scale pavement testing (Hugo, 1990). Pilot tests were conducted on a laboratory asphalt pavement with the tenth scale MMLS to evaluate the device for low temperature fatigue cracking (McDaniel, 1997). Further improvement of the MMLS resulted in the third scale MMLS (MMLS3) which has advantages over the tenth scale device including, most importantly, the ability to test a full-scale pavement.

As for rutting performance evaluation, the Hamburg Wheel-Tracking Device (HWTD) was developed by Helmut-Wind Inc. of Hamburg, Germany. It is used as a specification requirement to evaluate rutting and stripping for some of the most traveled roadways in Germany. The WesTrack forensic team (Epps, 2001) conducted a study on the rutting performance of coarse graded mixes at WesTrack sections using the HWTD.

The Asphalt Pavement Analyzer (APA) is a modification of the Georgia Loaded Wheel Tester (GLWT) and was first manufactured in 1996. The APA has been used in an attempt to evaluate rutting, fatigue, and moisture resistance of HMA mixtures. In this device, a loaded wheel is placed on a pressurized linear hose which sits on the test specimen. The wheel is then tracked back and forth along the hose to induce damage in the pavement (Brown, 2001)

Among the various devices available for APT studies, NCSU chose the MMLS3 for its promise as a simulator. The following sections present the logic behind scaling relationships and the features of the MMLS3.

2.2.2 DIMENSIONAL ANALYSIS

Since the MMLS3 development was challenged to bridge the gap between lab testing and full scale testing, all elements with given material properties and physical dimensions needed to represent at the similar properties from the full scale testing. A primary principle in the use of a scaled down loading device is that when pavement structural components are scaled down, elastic stress-strain relationships in the scaled down model are expected to be similar as those in the full scale pavement (Smit et al., 1996).

According to Kim's research (1998), the significant pavement variables consist of layer thickness, mass density and elastic property, such as Young's modulus and Poisson's ratio. The loading variables also include magnitude, contact area, and velocity of the load application. Using these variables, viscoelastic and inertial dynamic effects can be considered. To provide for similar viscoelastic effects, dynamic/inertia effects regarding load duration and velocity should be negligible. Since the MMLS3 pavement structure does not include a subgrade layer, only load duration must be addressed. It was found by Kim (1998) that once the load duration exceeds 50 msec, the pavement surface displacement was found to be basically constant.

According to the previous MMLS3 study done at NCSU (Kohlmann, 2002), the load duration is approximately 27.8 msec (7.5 km/hr). Due to load duration requirements, the load duration for a corresponding full scale device would to be 27.8 msec multiplied by the scaling factor of three, or 83.4 msec, which is over the threshold limit. Thus, the inertial effects can be assumed negligible. In the case of velocity, values under 100 km/hr do not significantly increase the maximum displacement from a stationary loading.

Therefore, loading at rates less than 100 km/hr causes inertia effects that is nearly negligible.

By using full scale pavement materials, mass density and elastic moduli of the layers do not need to be scaled. Therefore, the final scaling issues are loading magnitude and area of application such that the contact pressure on the full scale and 1/3rd scale are the same. The contact area of an MMLS3 tire scaled from a full-scale tire is approximately 51 cm² (for details see Section 2.4). The measured static loading of the MMLS3 was 2.9 kN with a tire pressure of 700 kPa. Using the scaling factor, N (=3), the full scale load is reduced by a factor of $\frac{1}{N^2}$. Therefore, the 2.9 kN corresponds to a full scale wheel load of about 26 kN. This is approximately 1/3rd of a typical dual wheel single axle load of 80 kN (18,000 lbs.).

2.3 PRINCIPAL FEATURES OF THE MMLS3

The MMLS3 was developed in South Africa for testing HMA in either the laboratory or field. This APT device, shown in Figure 2.1, is a third scale unidirectional vehicle-load simulator that uses a continuous loop for trafficking. It comprises four bogies with only one wheel per bogie. Each wheel simulates the loading of one tire in a standard American truck's dual tire system. The scaled static load of 2.9 kN is approximately one-ninth of the load on a single tire of an equivalent single axle load carried on dual tires. These wheels are pneumatic tires that are 300 mm in diameter, approximately one-third the diameter of standard truck tires.

The bogies and link sections are connected together to form a chain loop with a total of 48 guide wheels and 4 trafficking wheels. The guide wheels move along the two

sets of guide rails. While a bogie moves along the bottom section of the rails, the pneumatic tire is in contact with the underlying pavement, applying a load.

The trafficking wheel of each bogie has an adjustable suspension system by which the wheel load can be applied. The suspension system provides that the wheel load is practically independent of displacement within the 20 mm range. Building on lessons learned from previous full-scale APT devices, it was determined that a spiral transition curve was advantageous to eliminate the dynamic impulses caused by change in acceleration. This style of loading required a continuous ramp and transition zone at the junction of the circular and straight sections to allow for smooth introduction of the wheel to the pavement. Other benefits of the continuous rolling system approach were the enhanced safety and mechanical operation, prevention of spinout damage to axles, and noise reduction (MMLS3 Manual, 1999).

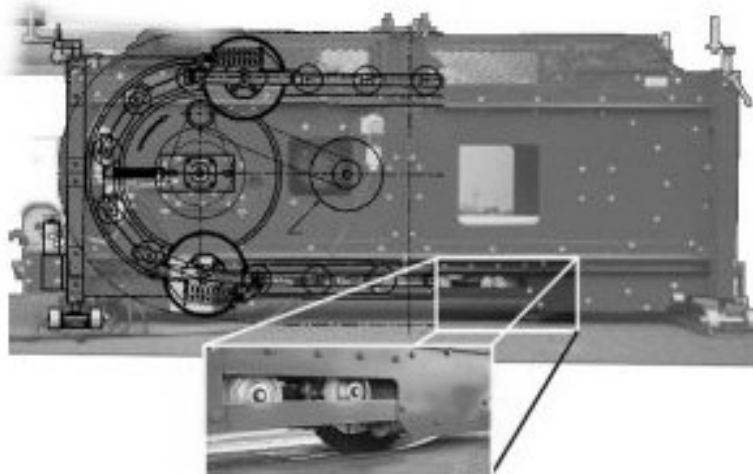


Figure 2.1 MMLS3 Schematics (MMLS3 Manual, 1999)

2.4 CHARACTERIZATION OF THE MMLS3 DYNAMIC WHEEL LOADS

The wheel load during the MMLS3 operation is measured in this study. Recent research has developed means of making valid direct measurements of the moving wheel load in the laboratory. Actual dynamic force of the MMLS3 in motion on the surface of pavements is measured by a 2.2 kN (500 lb) Flexiforce[®] pressure sensor (Figure 2.2) that is 0.127 mm thick and 203 mm long. The active sensing area is a 10 mm diameter circle at the end of the sensor. To integrate the force sensor into an application, a force-to-voltage circuit (Figure 2.2) is incorporated to convert the output from the sensor into the appropriate engineering units. Prior to the application in dynamic loading, the contour of static load from one wheel, which was inflated to 700 kPa at 20°C, was measured, with its distribution is shown in Figure 2.2. It may allow that the contact shape of the MMLS3 wheels on pavement surface is to be circular.

When the MMLS3 is set up at a signal input dial reading of 40 on the control panel, the wheels actually are circulated at a rate of 1.67 Hz, which is equivalent to 5,500 wheel applications per hour. On the other hand, this actual loading frequency of 3.3 Hz, where one period consists of loading of 0.3 sec and rest of 0.3 sec, in action was verified by the data shown in Figure 2.3. It was observed that the mean value of maximum dynamic loads from the four wheels, approximately 3.57 kN, was about 123% of the 2.9 kN static load. With the contact area of approximately 34 cm² from loading of wheels inflated to 700 kPa, surface contact stress was calculated to be approximately 1049 kPa.

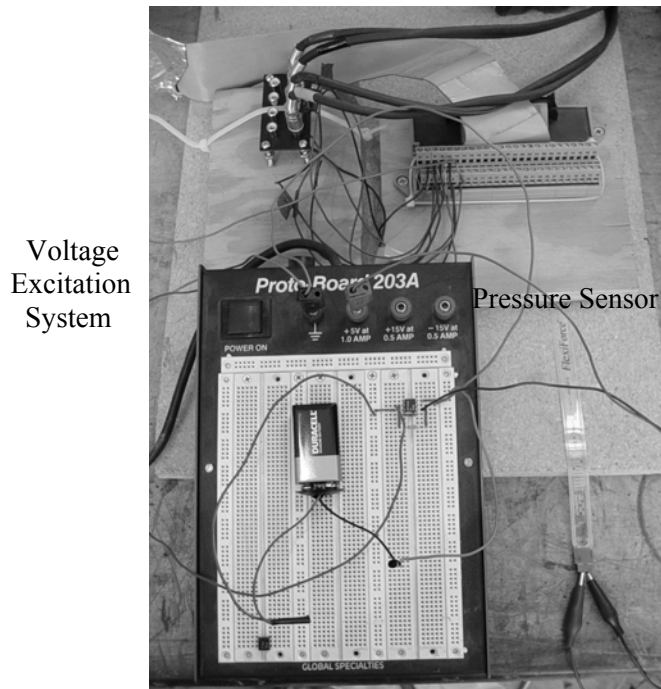


Figure 2.2 Flexiforce® Pressure Sensor and Voltage Excitation System

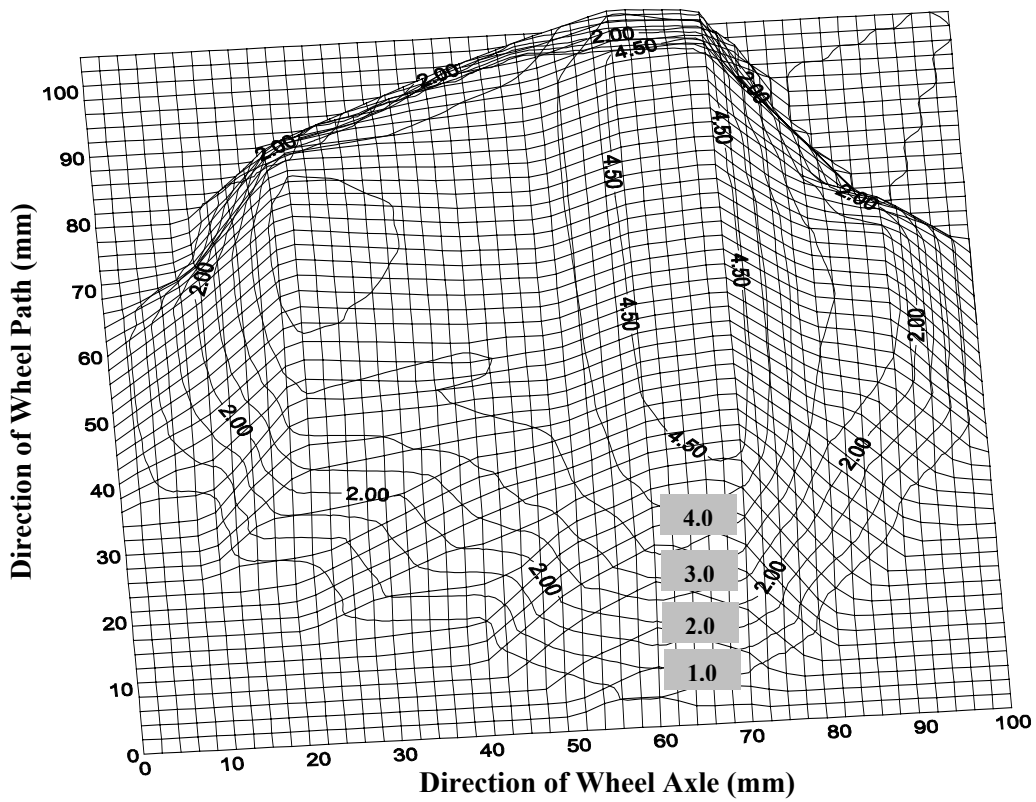


Figure 2.3 MMLS3 Static Load Distribution (under air pressure of 700 kPa at 20°C)

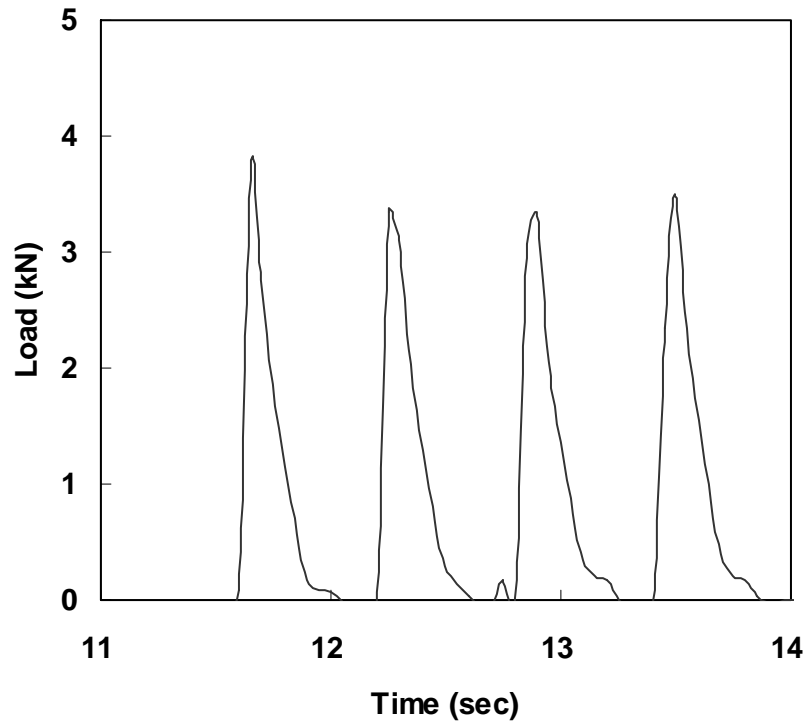


Figure 2.4 Measured Data for MMLS3 Dynamic Loading:
0.3 sec Loading and 0.3 sec Rest Period

CHAPTER 3

EXPERIMENTAL TESTING PROGRAM

3.1 INTRODUCTION

In order to achieve the objectives outlined in Chapter 1, a laboratory test program was developed. This program incorporated MMLS3 on fourteen model pavements and testing for cracking resistance using fiber composite asphalt specimens. Table 3.1 presents the MMLS3 tests to evaluate both fatigue cracking and rutting. According to preliminary trial testing experience, the MMLS3 loading condition, pavement construction technique, sensor instrumentation and measurement scheme were established. The experimental procedures for the MMLS3 testing will be described in Section 3.3.

3.2 MATERIAL TESTED

For the MMLS3 testing, four different North Carolina Superpave mixes are used. They are RI-1, RI-2, S9.5C, and I19C mixes. First three mixes are Superpave 9.5 mm mixes, and the I19C mix is the Superpave 19 mm mix. The aggregate gradation and asphalt contents for these mixes are summarized in Table 3.3. These mixes were designed using the Superpave volumetric mix design and were prepared using the aging procedure of 4 hours at 135°C. As was previously discussed, an important advantage of the MMLS3 over the tenth scale MMLS (McDaniel, 1997) is that the aggregate gradation does not have to be scaled down.

Table 3.1 MMLS3 Testing Programs

Distress	Mixture Type	Temp. (°C)	Static Load (Loading Rate)	Objectives
Fatigue	RI-2	20	2.9 kN (3.33 Hz)	<ul style="list-style-type: none"> ▪ Testing configuration / method
	RI-1			<ul style="list-style-type: none"> ▪ Cumulative damage analysis
	I19C-A			<ul style="list-style-type: none"> ▪ Air void contents effect ▪ Performance predictive algorithm
Rutting	RI-2	55/40	2.9 kN (3.33 Hz)	<ul style="list-style-type: none"> ▪ Testing configuration / method
	RI-1	55/40		<ul style="list-style-type: none"> ▪ Temperature effect
	I19C-OA ^a	40		<ul style="list-style-type: none"> ▪ Aging effect
	I19C-A ^b	40		<ul style="list-style-type: none"> ▪ Air void content effect ▪ Performance predictive algorithm

Note: a. I19C-OA stands for I19C mix prepared with over aging for 7 hours
 b. I19C-A stands for I19C mix prepared with aging for 4 hours

Table 3.2 Aggregate Gradations and Asphalt Contents for the Four Mixes
Used in this Study

	Sieve Size (mm)	RI-1	RI-2	I19C	S9.5C
% Passing	25.0	100	100	100	100
	19.0	100	100	99	100
	12.5	98	98	89	100
	9.50	95	95	78	95
	4.75	69	80	43	65
	2.36	51	63	28	47
	1.18	40	-	22	39
	0.60	-	-	16	30
	0.43	25	28	-	-
	0.30	-	-	10	18
	0.18	12	13	-	-
	0.15	-	-	8	12
	0.075	2.2	6.1	4.9	5.4
	AC Content (%)	5.8	6	4.7	5.2

Note: I19C and S9.5C mixes are prepared through the aging process

3.3 MMLS3 EXPERIMENTAL PROCEDURES

3.3.1 LABORATORY PREPARATION

The construction of asphalt slabs was undertaken at the Constructed Facilities Laboratory (CFL) at North Carolina State University. At the start of the laboratory preparation, a 6 m deep circular pit was filled with sand compacted near its maximum dry density, 1762 kg/m³ (110 PCF), which was verified by a nuclear density gauge. For fabrication of asphalt slabs, an industrial oven and a rolling vibratory compactor capable of compacting small-scaled pavements were also installed. It is known that rolling wheel compaction is close to field compaction conditions (Dijk, 1975), and therefore, the distribution of the aggregate particles and density of the mixture is similar to that produced by field compaction.

A vibrating force of 8.3 kN was applied to the roller axle inside the drum at a frequency of 50 Hz. After its compaction, the slab, which was compacted off to the side, was positioned between the guide rails which support the compaction roller. Then, a temperature chamber whose ducts were connected to a heating/cooling unit was placed on top of the MMLS3 to maintain the desired pavement temperature while the pavement was loaded by MMLS3. Figure 3.1 shows an overview of the testing facility in the laboratory.

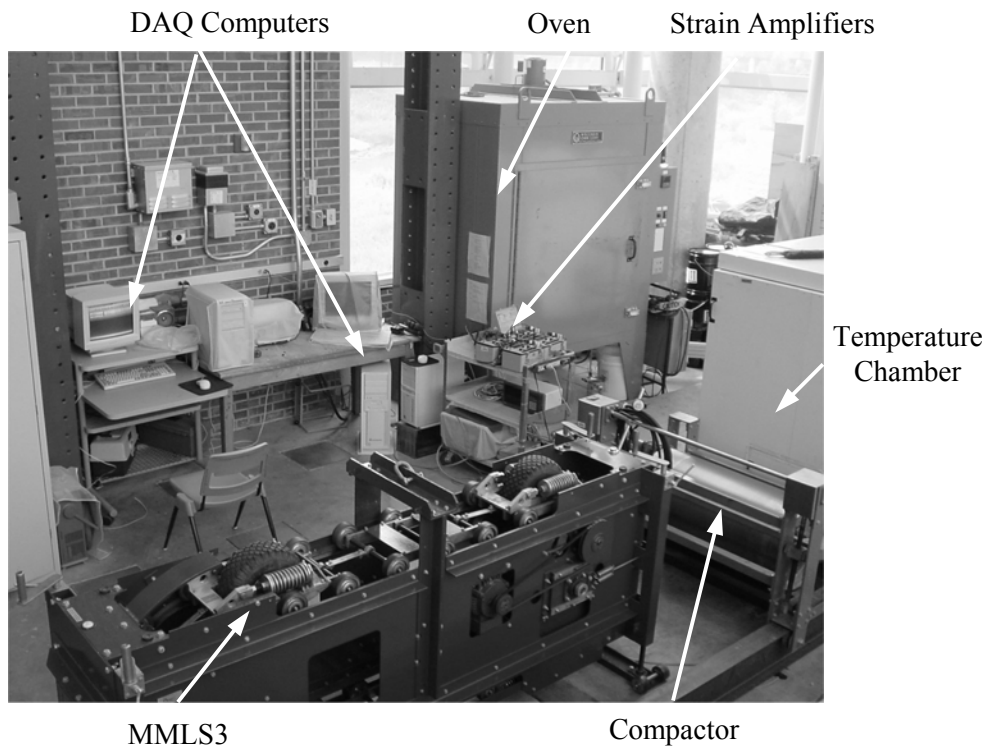


Figure 3.1 Testing Facility

3.3.2 MODEL PAVEMENT PREPARATION

For the fatigue testing, a 740 mm wide, 1,480 mm long, and 40 mm thick AC layer was constructed on the 20 mm thick steel plate. After compacted by a compaction roller, the asphalt concrete was cooled and taken out of the testing mold. Figure 3.2 presents the layered structure and instrumentation used for testing the fatigue model pavement. Once the total of 75 mm layer of neoprene rubber (= 3 x 25 mm high neoprene sheet) was positioned on the steel plate, strain gauges and thermocouples were placed on the surface of the neoprene. An MC-25 agent was applied as a coating at a rate of 0.5 litre/m² on the surface of neoprene layer. Then, the prepared asphalt slab was quickly cooled with dry ice to 10°C in order to stiffen the slab to avoid possible damage during movement to place it on the neoprene layers between the guide rails.

For rutting testing, a 550 mm wide, 1480 mm long, and 60 mm thick lift AC layer was directly constructed on the steel plate in the position where it was to be tested. As the rutting tests were performed on thicker pavements and the neoprene layers were not used, they did not need to be prepared off to the side and moved into position as were those for fatigue testing. After the compaction for the first lift, a tack coat was applied on the first lift. The second lift was then compacted on the first lift. The pavement structure profile for rutting testing is shown in Figure 3.3 (a), which is of help to understand the surface and mid-depth profile measurements. Figure 3.3 (b) presents dimensions and testing grid on the pavement surface.

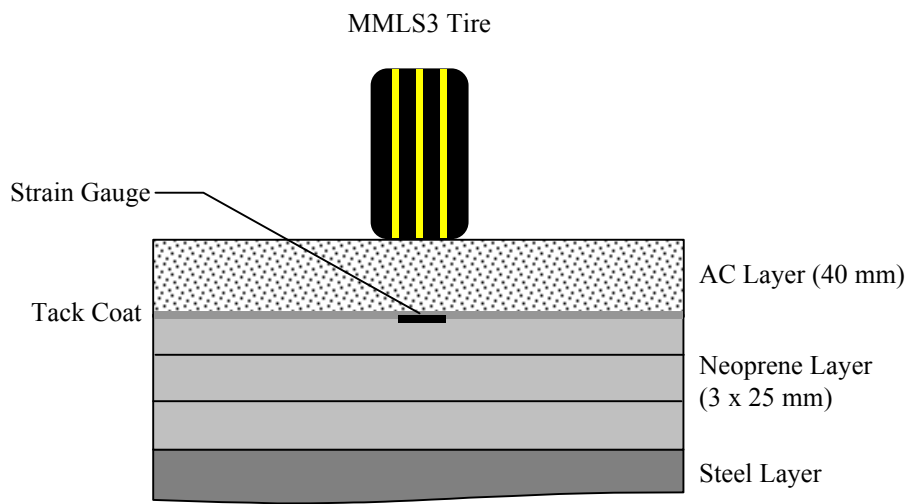
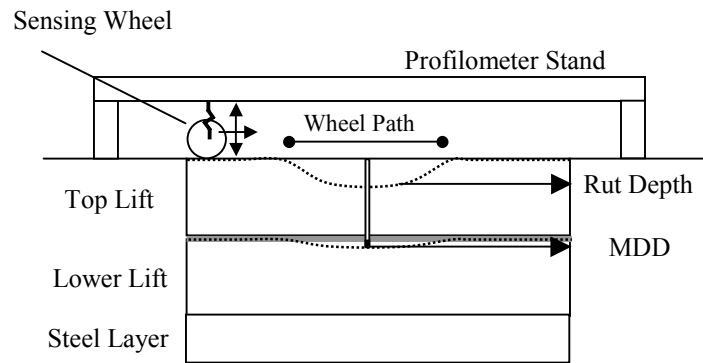
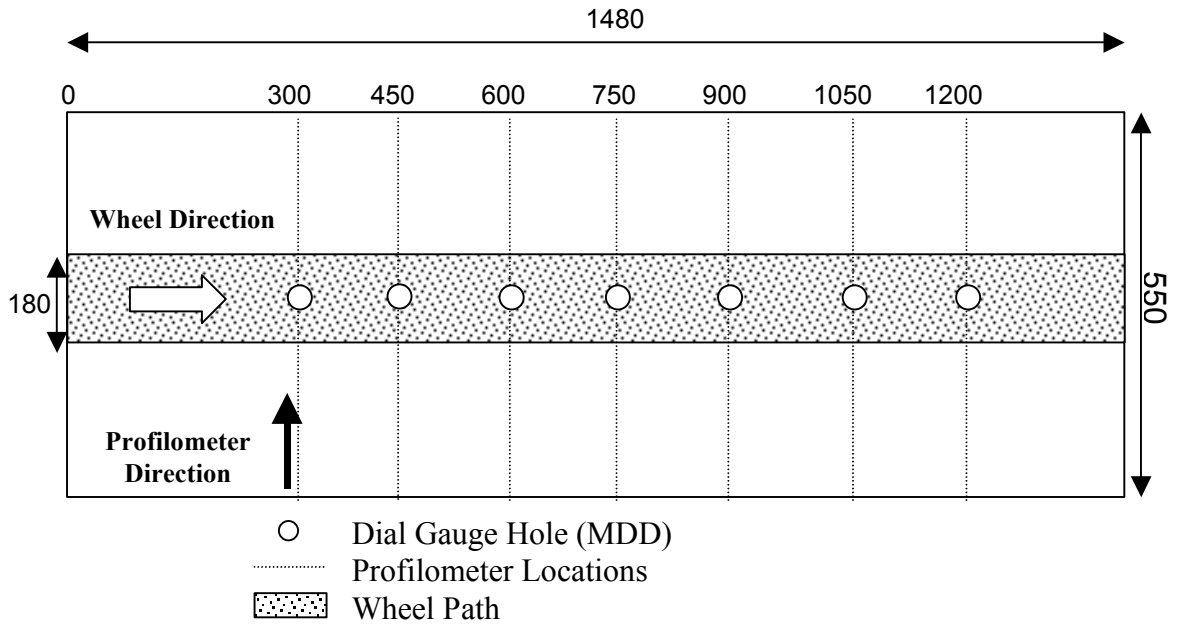


Figure 3.2 Schematic of Layered Structure and Instrumentation for Fatigue Pavement Testing.



(a) Cross-section Showing Profilometer and MDD Measurement Illustration
(not to scale)



(b) Plan View of General layout used for the MMLS3 rutting tests
(numbers are in 'mm')

Figure 3.3 Schematic of Layered Structures and Instrumentation for Rutting Pavement

3.3.3 MMLS3 TESTING DESCRIPTION

The first fatigue test using the RI-2 pavement was performed at 20°C to refine the testing configuration and methodology and to understand the general fatigue phenomenon in a laboratory thin pavement. 50 mm sensor spacing and Wavelet Correlation Method (WCM) were determined to be appropriate to apply stress wave technique to monitor stiffness change at loading stages on a 40 mm thin AC layer structure. The development of these procedures is discussed in chapter 4.

Using RI-1 pavement, fatigue damage analysis associated with both MMLS3 and core testing was carried out and a fatigue service life prediction procedure was considered. Changes in fatigue performance due to air void content deficiency was investigated and IDT laboratory fatigue testing using specimens prepared with a gyratory compactor were used along with the results from the MMLS3 on pavement I19C in order to complete the fatigue service life prediction algorithm.

Stress wave testing in MMLS3 fatigue testing was undertaken. The stress wave experiments were composed of two phases. The first program was to investigate fatigue damage effects on the laboratory pavement. Repetitive wheel loads using the MMLS3 were applied. For the entire test periods, pavement temperature was maintained at 20°C. The surface wave tests were conducted at the following times: before any loads were applied, immediately after each group of the MMLS3 loading was interrupted, and at the end of each one hour rest period. Surface wave data were collected from the center of the wheel path. Visual surface condition was periodically surveyed so that cracks on the pavement surface were monitored and crack lengths measured throughout the fatigue life.

The second phase of the experimental program was designed to investigate the magnitude of microdamage healing that occurred during periods of rest. A marble impact was conducted on RI-1 pavement at 90 or 180 seconds interval.

Rutting performance was first evaluated using the RI-2 pavement. Tests were conducted at 55°C and 40°C to develop testing procedures, e.g., slab preparation, actual heater temperature set up, temperature maintenance, and measurement skill etc. Base on this knowledge, three factors, temperature, air void contents, and aging, that greatly gave a critical effect on rutting performance were studied on RI-1 and I19C pavements.

RI-1 pavement with approximately 5.5% air void content was prepared and then tested at 55°C and 40°C monitoring changes of rut depth at increments throughout the MMLS3 loading. Parametric analysis enabled a quantitative analysis of the effect of temperature on performance. Mix I19C was prepared through aging procedure at 135°C. To see the effect of aging, prior to compaction the mixes were aged for 4 hours and 7 hours, respectively. The MMLS3 rutting test without lateral wandering system was applied and the resulted rut depths were compared for sections of similar air void contents, 10.2% (4-hour aging) versus 11.3% (7-hour aging). As for the effect of density deficiency, I19C-A pavements in 8.7, 9.7, and 10.2% of air void contents were tested and rutting performance was compared.

Triaxial permanent deformation tests on specimen prepared in the laboratory with the I19C-A mixture were used to provide the empirical constants and resilient strain needed in the prediction model. The multi-layer elastic program, EverStress, was used to find the resilient strains that were used in the rut depth prediction algorithm to predict the I19C-A pavement performance during MMLS3 testing at 40°C.

3.4 FRAC EXPERIMENTAL PROCEDURES

Table 3.2 shows conditions and testing program for fiber reinforced asphalt concrete (FRAC) tests that consist of two phases: (a) single fiber pullout testing and (b) IDT strength testing. For the FRAC testing, 15-denier nylon fibers were manufactured and provided by Mini Fibers, Inc. The fibers were cut and to 100 mm long for single fiber pullout tests, and 12 mm and 6 mm long for IDT strength tests. Asphalt binder PG 70-22, manufactured by Citgo, Willington, NC, was used as a matrix for these pullout tests. Table 3.2 summarizes the mix design characteristics and material specifications used for these tests. The surface course was composed of a fine grade North Carolina Superpave mix using 9.5 mm nominal maximum size of aggregate (NMSA), referred to as S9.5C-A. An asphalt content of 5.8% of the total weight of mixture was used for all specimen with fibers.

3.4.1 SINGLE FIBER PULLOUT TEST

Prior to strength testing of fiber embedded asphalt concrete, the interaction between single nylon fibers and an AC binder was investigated using pullout tests. The tensile properties of the nylon fibers were tested according to ASTM D2256. Then, fibers of five different lengths, 2, 4, 8, 10, or 20 mm, were embedded into AC binder filled containers at a desired. According to standard yarn tensile strength tests based on ASTM D2256, a pullout test rate of 300 mm/min at 30 mm gauge length was applied. The recording of load and displacement, along with visual observation, allowed the determination of either fiber rupture or pullout load to be determined.

Table 3.3 FRAC Testing Programs:

(a) Single Fiber Pullout Testing

Parameter	Description
Loading Mode	Constant Elongation Rate
Binder	PG 70-22
Fiber Type	Nylon
Embedded Fiber Length (mm)	2, 4, 8, 10, and 20
Gauge Length (mm)	30
Temperature (°C)	20
Loading Rate (mm/min)	300
Loading Device	STM

(b) Indirect Tension Strength Testing

Parameter	Description
Mixture Type	S-9.5
Loading Mode	Monotonic
Loading Rate (mm/min)	50.8
Fiber Type	Nylon
Fiber Length (mm)	6 and 12
Temperature (°C)	20
Linear Density (denier)	15
Fiber Volume Fraction (%)	0, 0.25, 0.5, and 1
Loading Device	Universal Testing Machine (UTM)

3.4.2 INDIRECT TENSION STRENGTH TEST (IDST)

According to Wen's dissertation work (2001), the IDST was designed to apply a load on a specimen at a constant rate of elongation. Figure 3.4 shows a schematic of the IDST. Values of strain were calculated using the measured displacement across the 50.8 mm gauge length. A constant-crosshead-rate monotonic test was performed at a ram movement of 50.8 mm/minute. While the ram travels as shown in Figure 3.4, the load level reached its peak value and was decreasing. However, the test was stopped before the specimen was completely split to protect the LVDT sensors from possible damage.

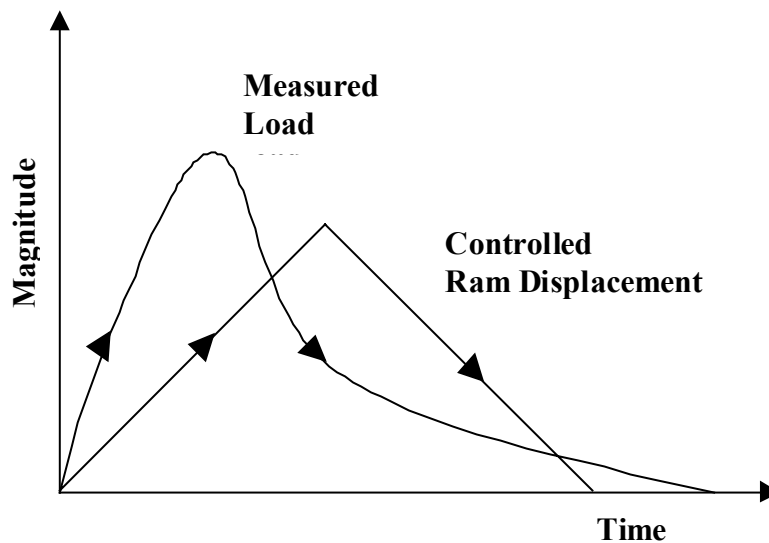


Figure 3.4 Behavior of Load Measurement under Controlled Ram Displacement
(Schematic Illustration of IDST)

3.5 INSTRUMENTATION CONSIDERATIONS

Temperature and Strain: The gauges embedded in the pavements include K-type thermocouples to monitor/control pavement temperatures at different depths and strain gauges to measure the tensile strain amplitude at the bottom of the AC layer. The

sensing probe of thermocouple is approximately 10 mm long. In general, for strain measurements on non-homogeneous material, it is preferable to select a gauge length that is several times larger than the nominal size of the aggregate. To satisfy this criterion, a strip-type strain gauge with a 50 mm gauge length was chosen and placed transverse to the traffic direction.

Stress Wave: Surface wave testing was performed with four PCB A402 accelerometers. The accelerometers have magnetic adapters that allow them to couple to a steel disk glued to the AC pavement at 50 mm intervals. Sensors were connected to a Tektronix oscilloscope that acquired the data once the first accelerometer was triggered by a signal produced from an impact hitting the pavement. Next, the data were stored in the computer through the Stress Wave Analysis Program (SWAP). Testing configuration and detail instrumentation will be discussed in Chapter 4.

Fatigue Cracking: Fatigue crack length was determined using image analysis at different stages of testing. The cracks on pavement were physically drawn on Plexiglas by pens of different color at each measurement interval and pavement surface images were taken using a digital camera. By image analysis software, the cumulative crack length can be measured corresponding to actual scale.

Rut Depth: To fully understand pavement distresses occurring under MMLS3 loading, the rut depths were also measured and compared using the profilometer and electronic indicator. Transverse profile is one of the key measurements in this research to evaluate the rutting increment performance. A Mitutoyo profilometer using RS-232C communication consists of a measurement stand and a vertical reader unit. The stem of the vertical reader slides freely in a slot to obtain the rut depth reading. Ten mm-spaced

transverse profile measurements with a tolerance of ± 2 mm were conducted. The profilometer provides a comparison of the surface of the AC layer's initial measurements with measurements made at intervals during testing. A CDI electronic indicator that has a sensitivity of 0.01 mm was used to measure permanent deformation along the surface layer depth. This indicator also enables determination of the deformation within the surface layer by subtracting the deformation in underlying layers from the deformation measured on the pavement surface. The change in these measurements throughout testing provides information related to the rutting evolution of the slab.

Air Void Content. Air void content was measured by a vacuum chamber, CoreLokTM, which was developed due to the increase in the use of coarse and open graded mixes which created a need for a more reliable and accurate method of bulk-specific gravity measurement of laboratory specimens. Following ASTM (2001), the vacuum chamber system was used with specially designed polymer bags to completely seal the cored asphalt samples from water during the bulk-specific gravity measurements. This system was also used to determine the maximum specific gravity of loose samples.

3.6 SUMMARY

The experimental program described in this chapter was designed for evaluation of fatigue and rutting performance. Accelerated pavement testing (APT) using the MMLS3 was programmed to perform on model pavements. As a further fatigue study, fiber composite asphalt concretes testing was planned for fatigue cracking resistance.

CHAPTER 4

STRESS WAVE ANALYSIS USING WAVELET CORRELATION METHOD

4.1 INTRODUCTION

Nondestructive evaluation (NDE) of an existing pavement can provide information required for efficiently administering pavement management systems. Once the results of NDE are correlated to actual visible cracks, engineers may then have a tool that enables them to constantly monitor a pavement and increase the life of the pavement by providing the needed maintenance at the appropriate time (Rosenblad et al, 1993, Gucunski and Woods, 1995, Kim et al, 1998). Surface wave analysis using many different methods, e.g., static deflection, steady-state dynamic deflection, impact load response etc., and wave propagation, has been proposed for determining the elastic properties and thickness of pavement systems (Nazarian et al, 1995). Since the wave speeds of a dispersive signal depend on material properties of the pavement, a change in its properties, as may be caused by deterioration or damage, results in changed wave speeds for the representative frequency in a signal. For this reason, to compute wave speeds, the Short Kernel Method (SKM), a digital signal processing algorithm, was developed by researchers at North Carolina State University (Chen and Douglas, 1994). This noninvasive monitoring and analysis has been proven to be an effective technique that allows the quantitative determination of stiffness changes in the asphalt layer due to fatigue damage and healing. It has been found that there is a significant reduction of AC stiffness before visible cracks appear on the pavement surface, possibly indicating the importance of microcracking (Kim, 1998). The SKM method using wavelet kernel for a

pavement consisting of a thin AC surface layer of 40~60 mm thick is presented in this chapter.

4.2 BACKGROUND

4.2.1 SURFACE WAVE PROPAGATION

The elastic properties of the surface layer in a multi-layered system can be deduced from measurements of the wavelength and velocity of imposed vibrations of known frequency. In a solid half-space like the surface of a pavement, an elastic surface wave may occur. When the half-space is a layered medium, surface waves are dispersive in nature. Dispersion is the phenomenon in which the velocity of a propagating wave at a particular frequency is dependent on the wavelength of that frequency.

Surface waves propagate along a cylindrical wavefront near the surface of a half space and the particle motion of the surface waves is in the vertical and horizontal directions and varies with depth (Richart, 1960, Kim, 1998). Surface waves contain vastly more energy and travel slightly slower than the shear wave, whose wave speed is about 60 percent of the longitudinal wave speed. The relationship between the surface and shear wave velocities arises from the solution of the two dimensional equations of motion for a continuum. The solution relates the surface wave speed to the shear wave speed (Kolsky, 1963):

$$\alpha^6 - 8\alpha^4 + 8\left(3 - \frac{1-2\nu}{1-\nu}\right)\alpha^2 - 16\left(1 - \frac{1-2\nu}{1-\nu}\right) = 0 \quad (4.1)$$

where, α = the ratio of the surface wave speed to the shear wave speed, and
 ν = Poisson's ratio.

In an elastic, isotropic medium, the elastic constants are determined from the surface wave velocity according to the following relationships:

$$V_s = V_R / \alpha \quad (4.2)$$

$$G = \rho \cdot V_s^2 = \left(\frac{\gamma}{g} \right) \cdot V_s^2 \quad (4.3)$$

$$E = 2G(1 + \nu) \quad (4.4)$$

where,

V_s	=	Shear wave velocity
V_R	=	Surface wave velocity
ρ	=	Density of the material in the layer
G	=	Shear modulus
γ	=	Unit weight
g	=	Acceleration of gravity
E	=	Elastic modulus

These relationships allow the elastic modulus to be calculated from a surface wave velocity measured using the stress wave test.

4.2.2 SHORT KERNEL METHOD (SKM)

The SKM is a frequency-dependent operation based on the cross-correlation procedure. By implementing the SKM, the undesirable frequencies can be filtered for the purpose of calculating the time needed for the wave to travel between spaced sensors.

Data sent through the SKM at a set frequency are mathematically defined as follows:

$$SKM(j, k) = \sum_{i=1}^{N_2-N_1} f(\tau_i) \cdot g[(\tau_i + j \cdot \Delta t), k] \cdot \Delta t \quad (4.5)$$

where,

$SKM(j, k)$ = the j th term of the cross-correlation currently being performed
at the k th frequency,

f = the time record from one accelerometer,

g = the fragment of kernel used to perform the cross-correlation,

N_2 = the number of data points in f , and

N_1 = the number of data points in $g(t)$.

The Short Kernel Method was explained by Chen (1995), showed how to determine the velocity of a frequency in a timber pile.

4.3 WAVELET CORRELATION METHOD (WCM)

4.3.1 WAVELET CONSTRUCTION

A wavelet is a waveform of effectively limited duration that has an average value of zero. While sinusoids are smooth and predictable, wavelets tend to be irregular. It is well known that an arbitrary square integrable function $x(t)$ can be reconstructed from another square integrable function $g(t)$ when $g(t)$, a kernel of wavelet, satisfies two conditions (Li and Ma, 1999):

If $g(t)$ is square integrable,

$$\int |g(t)|^2 dt < \infty \quad (4.6)$$

and, it practically satisfies the *admissibility* condition that $g(t)$ has a zero mean value:

$$\int g(t) dt = 0 \quad (4.7)$$

The wavelet analysis assesses the *similarity* between the stress wave and the wavelet kernel, $g(t)$. Since the vibration energy of seismic waves is dissipated during their

propagation by material damping, it is acceptable to choose a decaying exponential function as a kernel. Accordingly, the following basic wavelet is proposed:

$$g(t) = \frac{1}{\sqrt{f}} e^{(-\sigma t)} \sin(w_o t) \quad (4.8)$$

where, $w_o = 2\pi \cdot f$ (f: frequency).

An attenuation coefficient, σ , of 0.9 was determined by compromise in performance between general attenuation shape of stress waves at high frequency and emphasizing a center peak, using high diminishing rate from a center peak toward both ends, for easy selection of corresponding peak at each sensor. A sample wavelet kernel is plotted in Figure 4.1 with a filtering frequency, f , of approximately 19 kHz.

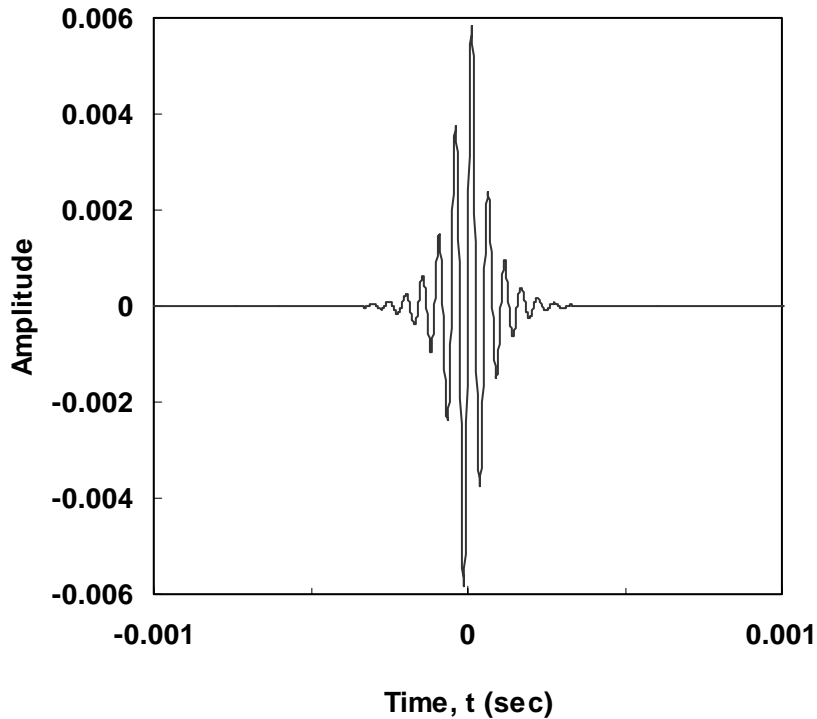
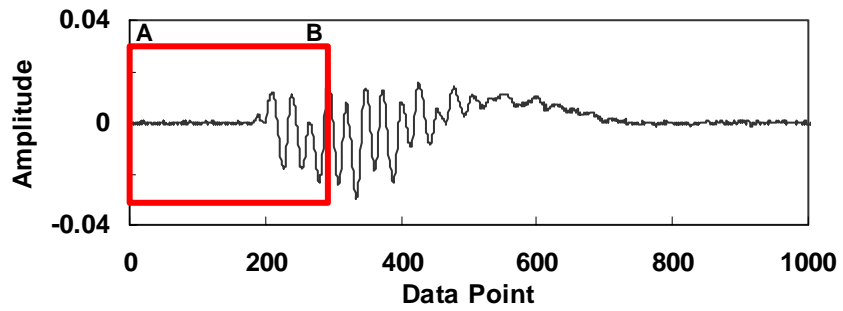


Figure 4.1 Sample Wavelet Kernel
(Frequency (f) = 19 kHz, Attenuation Coefficient (σ) = 0.9)

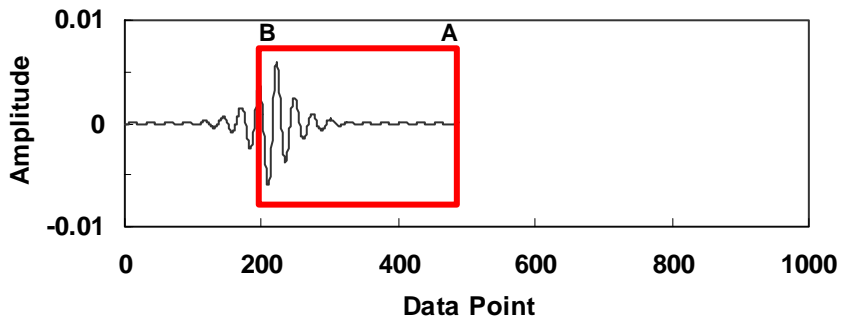
4.3.2 IMPLEMENTATION OF WCM

WCM transform procedure is graphically illustrated in Figure 4.2. Figure 4.2 (a) is actual data $x(t)$; Figure 4.2 (b) is a kernel WCM $g_k(t)$ at a designated kernel frequency k , and Figure 4.2 (c) is the same WCM kernel with time shifting. The WCM transform $g_k(t)$ is calculated by lining up signal $x(t)$ and the WCM kernel $g_k(t)$, i.e., the first point at $x(t)$ is lined up with the first point at $g_k(t)$ and so on, multiplying $x(t)$ by $g_k(t)$ point by point. The sum of the products is the value of the first point of the WCM transform $W_k(t)$. The same process is continued until all of the $W_k(t)$ values are found.

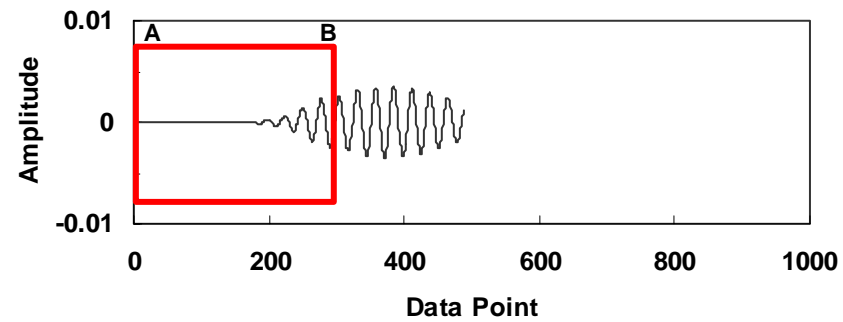
The actual stress wave for RI-1 pavement was acquired and transformed by WCM using the wavelet kernel of 19 kHz in Figure 4.1. This WCM-transformed stress wave was re-analyzed by the Fast Fourier Transform (FFT) to see how well the WCM filtered out undesirable frequencies. As shown in Figure 4.3, the WCM is successfully implemented. As a result, undesirable frequencies lower than 16 kHz diminished.



(a) Surface Wave ($x(t)$)



(b) Wavelet Kernel ($g_K(t)$)



(c) WCM Transformed Wave ($W_K(t)$)

Figure 4.2 Illustration of WCM Transformation Implementation

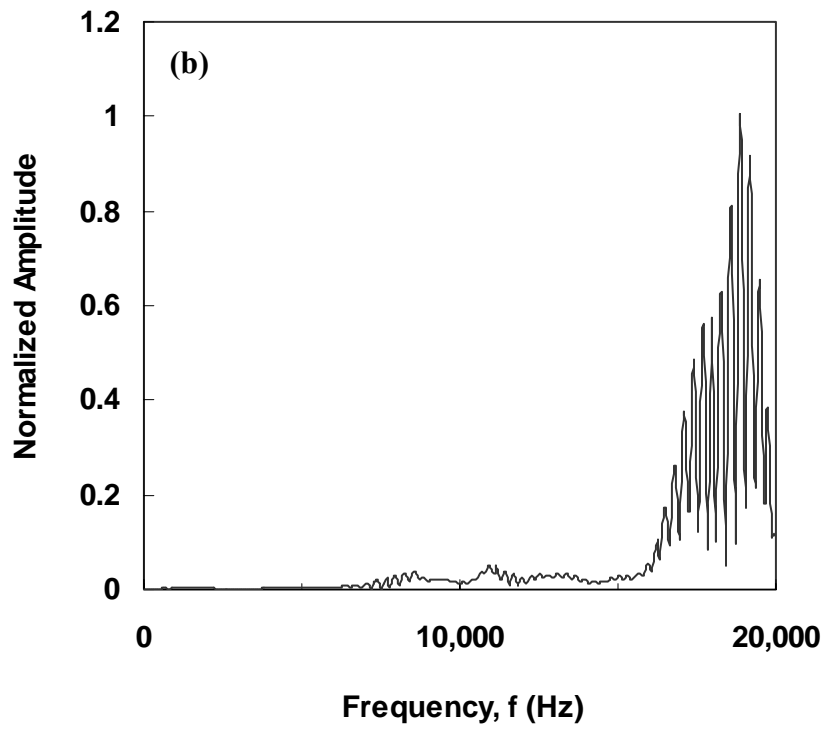
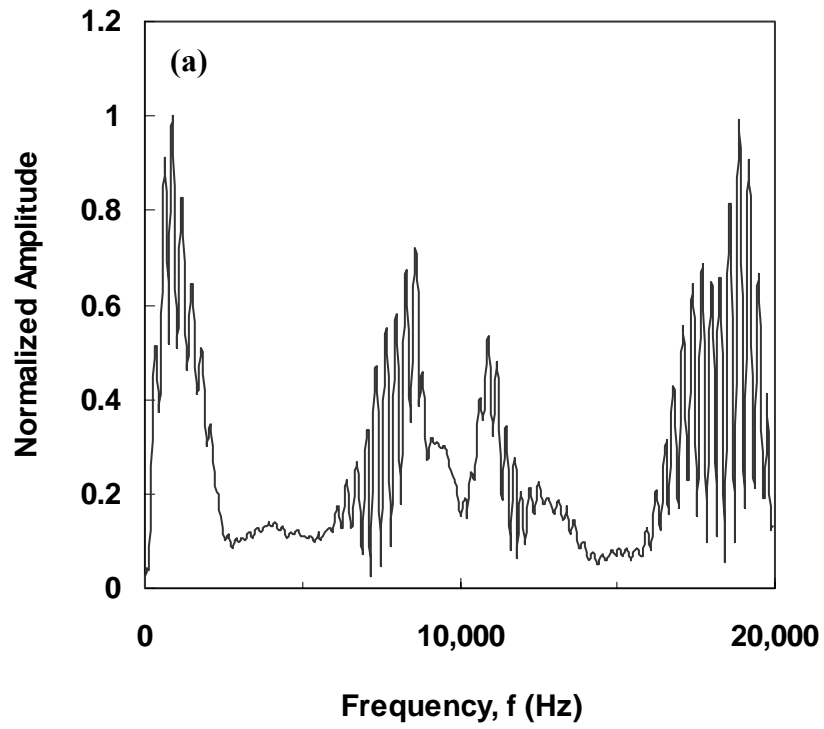


Figure 4.3 Power Spectrum of:
(a) Actual Surface Wave and (b) WCM Transformed Wave

4.3.3 EVALUATION OF WCM ACCURACY WITH SYNTHETIC DATA

To explore the performance of the WCM transformation, the accuracy of the phase velocity computation is evaluated with synthetic data. The artificial wave was constructed with the following elements:

- Selected 5 sine waves with different frequencies
- White noise (0.025 amplitude)
- Assumed phase velocities and attenuation coefficients
- Time delay based upon given phase velocities
- 400 μ sec pre-triggering period
- Data acquisition from 3 accelerometers

Table 4.1 presents the parameters used to construct each of the component waves used to make the composite waveforms. The frequency, phase velocity and attenuation data apply to both cases, whereas amplitudes of the 19 kHz components were alternated.

For these analyses, the first two cases were designed to demonstrate the ability of the WCM to extract a wave of a specified frequency, specifically 19 kHz, out of a composite wave. To do this, a frequency range and wave construction elements were devised to simulate the power spectrum (Figure 4.3 (a)) of the stress wave acquired from the R11 pavement. In order to simulate the observation that high frequency energy tends to diminish with increasing pavement deterioration, the composite wave included a high frequency component whose magnitude could be reduced. Case I shows a surface wave composed of 5 major frequencies (Figure 4.4 (a)): 1, 5, 9, 12, and 19 kHz. Case II was designed to model the surface wave from a damaged pavement, where approximately

70% energy at 19k Hz was lost as shown in Figure 4.4 (c). The components used and resulting composite waves are shown in Figure 4.4 (a) and (b).

Figures 4.5 (a) and 4.6 (a) show the transformed WCM plots at three sensors at 50 mm spacing for cases I and II, respectively. The WCM was performed to verify the ability of the method to extract the correct phase velocity at 19 kHz. Table 4.2 (a) presents the time at which the peak amplitude occurs at the first and second sensors. From the time and the gauge spacing, the phase velocities should be calculated. The results show that the WCM method found the phase velocity with only about 0.8 % error for 19 kHz for both cases I and II. In comparison with WCM, performance of SKM transformation, as shown in Figures 4.5 (b) and 4.6 (b), was evaluated. The SKM resulted in about 3.0 % error in prediction in Table 4.2 (b).

Table 4.1 Elements of Synthetic Waves for Effect of Damage

Dominant Frequency, f , (kHz)		1	5	9	12	19
Phase Velocity, λ_{vph} , (m/sec)		600	750	850	940	1050
Attenuation Coefficient, σ		1	0.9	0.5	0.3	0.3
Amplitude	Case I	0.1	0.6	0.3	0.3	1
	Case II	0.1	0.6	0.3	0.3	0.3

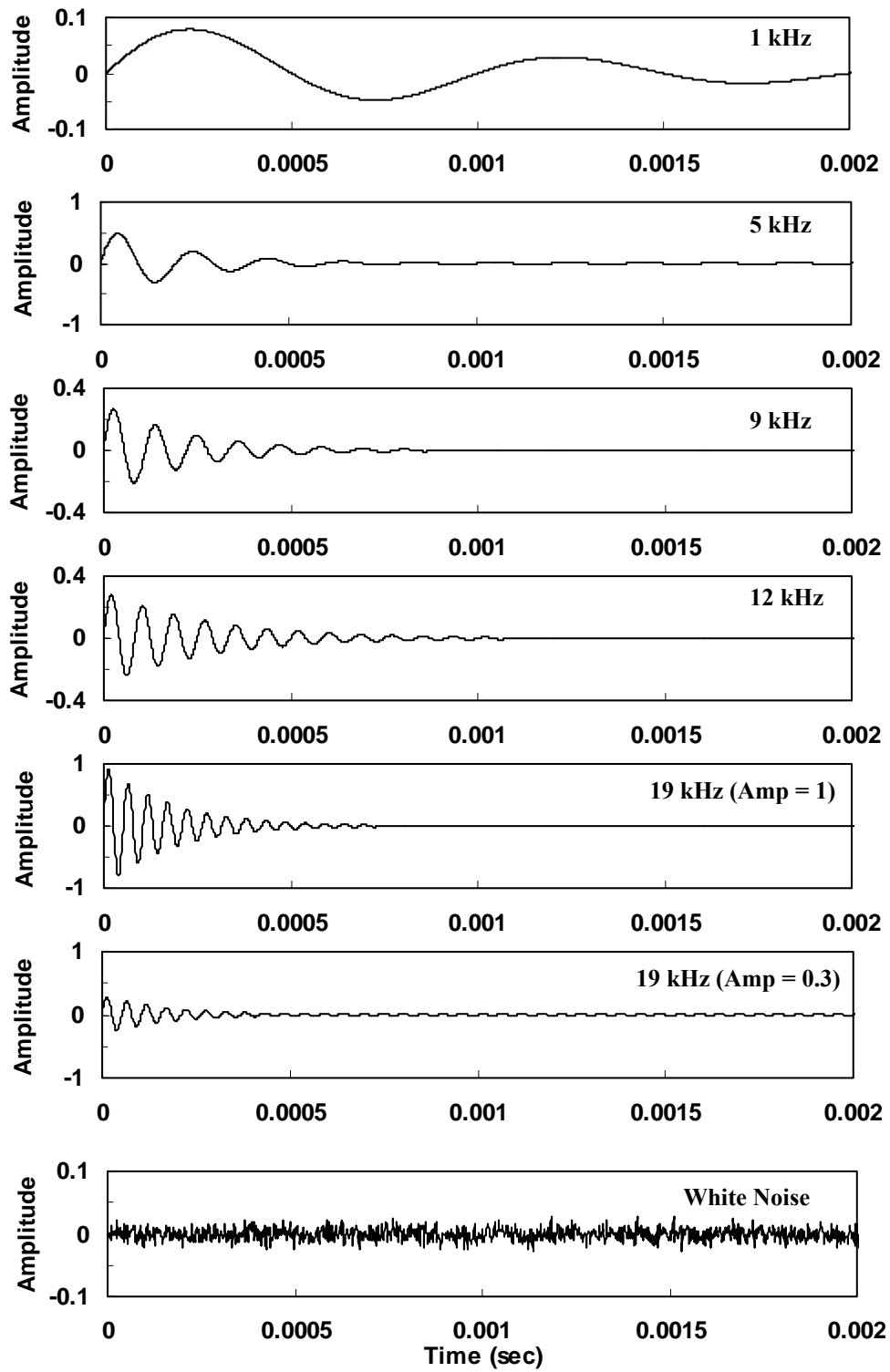


Figure 4.4 (a) Component Waves for Case I and Case II
(Amp stands for Amplitude)

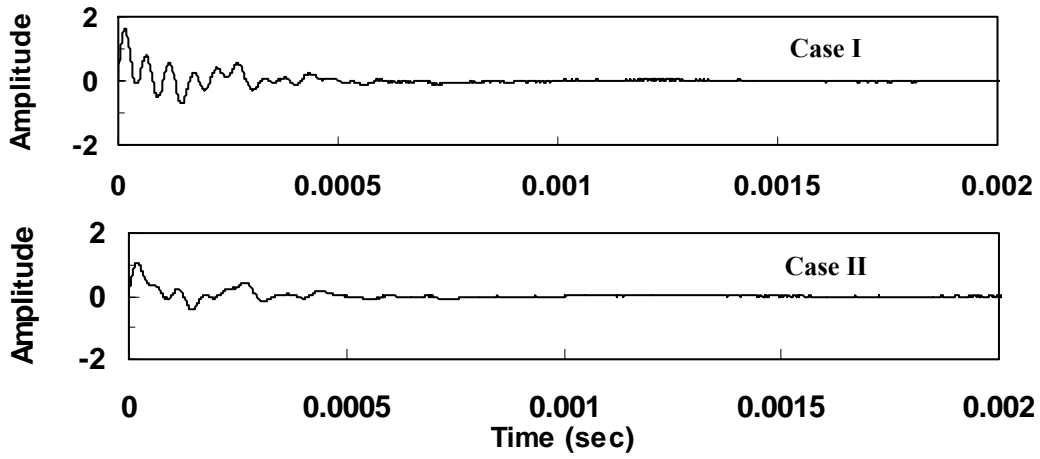


Figure 4.4 (b) Composite Waves for Case I and Case II

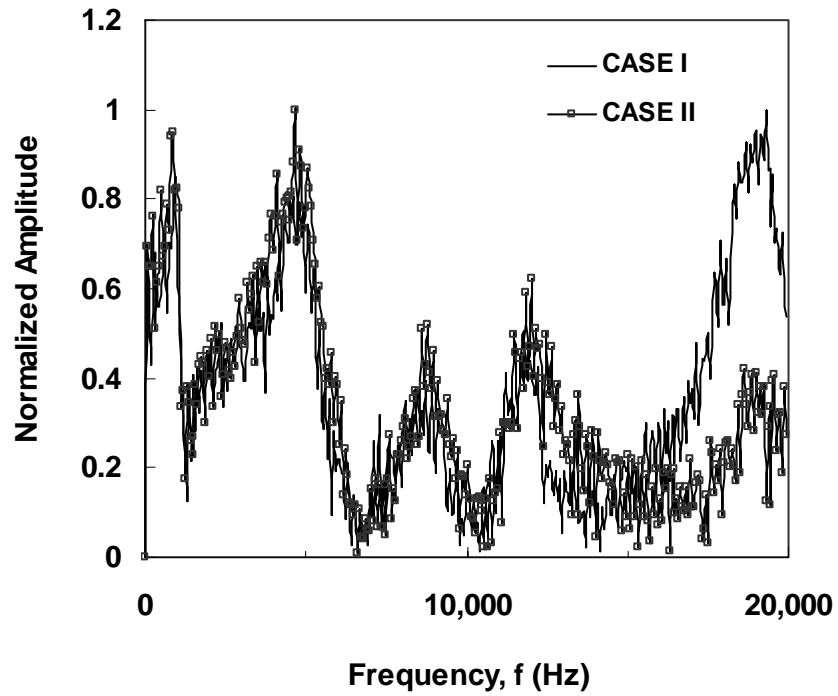


Figure 4.4 (c) Frequency Analysis for Case I and Case II

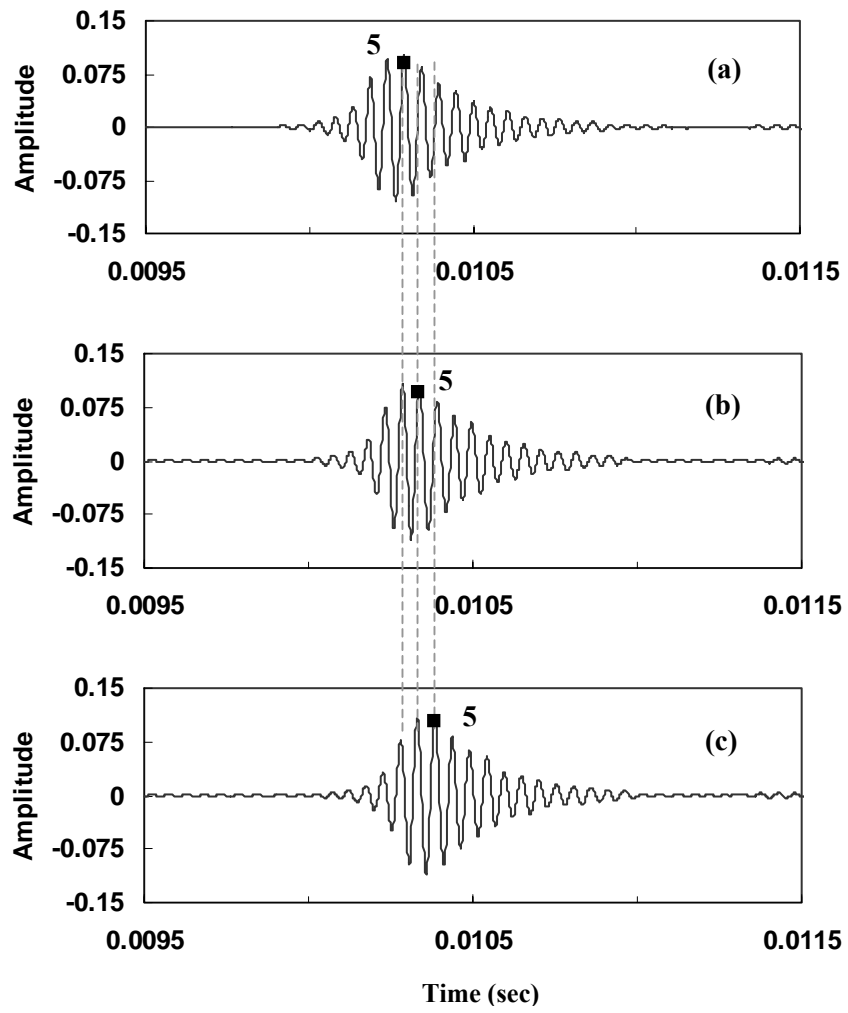
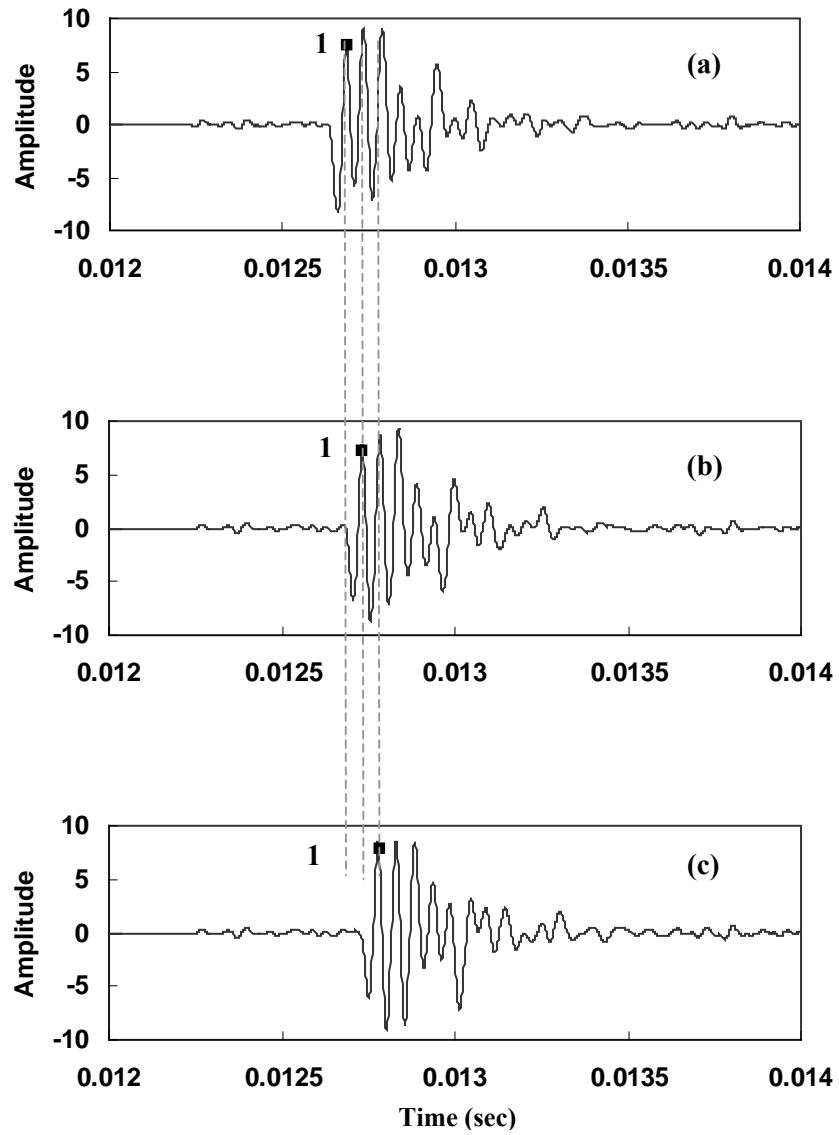


Figure 4.5 (a) Case I: WCM Transformed Waves at:
 (a) 1st channel (b) 2nd channel (c) 3rd channel



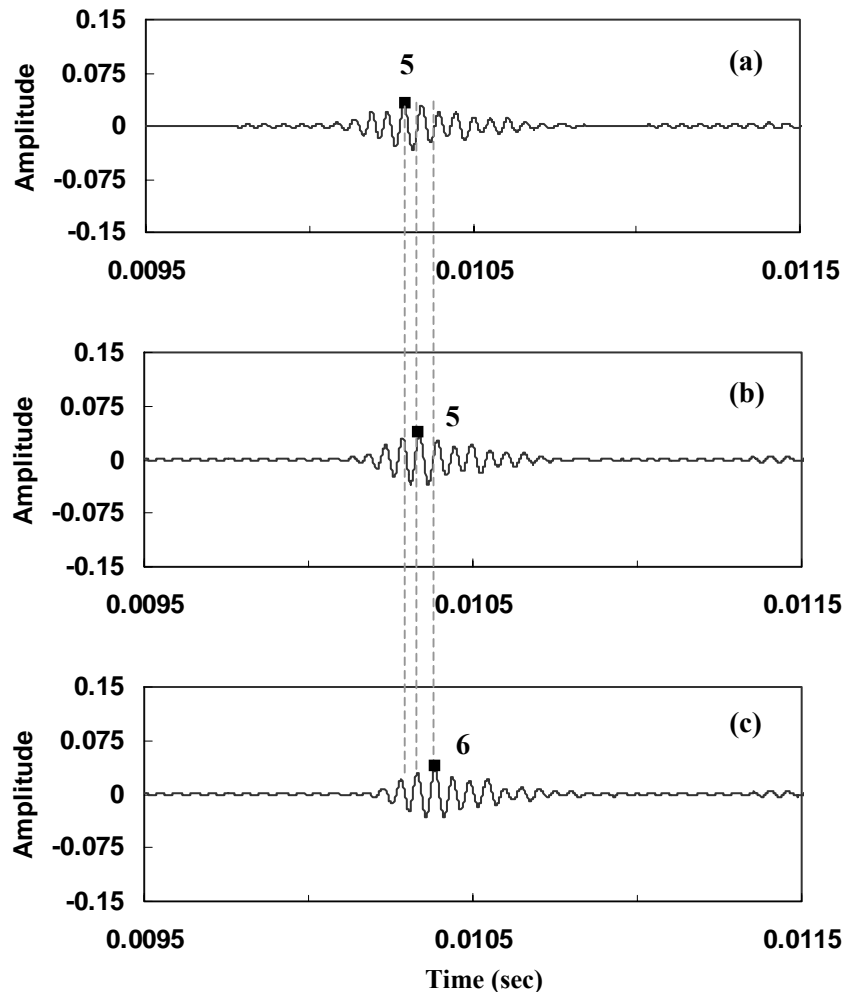


Figure 4.6 (a) Case II: WCM Transformed Waves at:
 (a) 1st channel (b) 2nd channel (c) 3rd channel

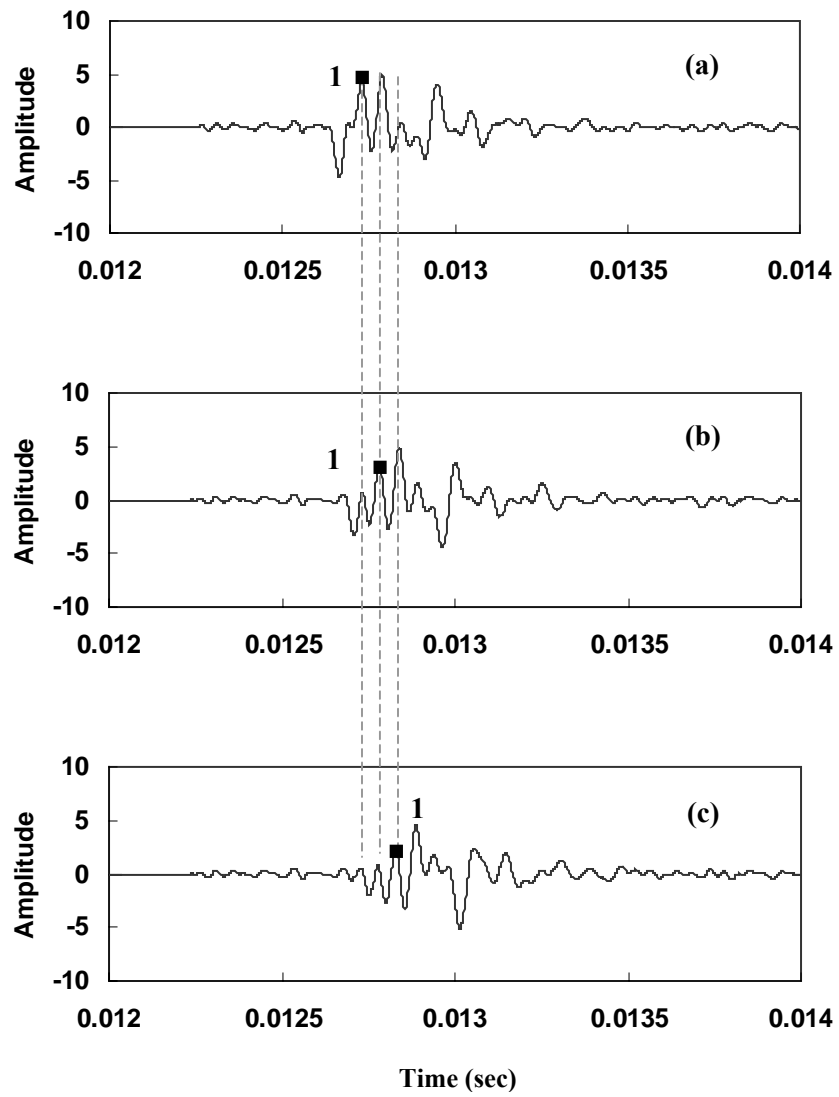


Table 4.2 (a) Phase Velocity Calculations for Cases I and II Based on WCM

CASE	PEAKS	Sensors				Predicted Velocity ($0.05 / \Delta_{t1-2}$) (m/sec)	Input Velocity (m/sec)
		1	Δ_{t1-2} (10^{-5})	2	3		
		Arrival Time (sec)					
I	444	0.01024	4.8	0.010288	0.010334	1042	1050
	555	0.010292	4.8	0.010340	0.010386	1042	
	666	0.010346	4.8	0.010394	0.010444	1042	
II	554	0.010240	4.8	0.010288	0.010334	1042	
	665	0.010292	4.8	0.01034	0.010388	1042	
	776	0.010346	4.8	0.010394	0.010442	1042	

Note: Δ_{ti-j} = traveling time (sec) between channel i and channel j

Table 4.2 (b) Phase Velocity Calculations for Cases I and II Based on SKM

CASE	PEAKS	Sensors				Predicted Velocity ($0.05 / \Delta_{t1-2}$) (m/sec)	Input Velocity (m/sec)
		1	Δ_{t1-2} (10^{-5})	2	3		
		Arrival Time (sec)					
I	111	0.012688	4.6	0.012734	0.01278	1087	1050
	222	0.012736	5.0	0.012786	0.012832	1000	
	333	0.012792	4.8	0.01284	0.012886	1042	
II	245	0.012732	5.2	0.012784	0.012832	962	
	356	0.01279	5.0	0.01284	0.01289	1000	

Note: Δ_{ti-j} = traveling time (sec) between channel i and channel j

The effect of nearby frequencies was assessed using synthetic waves as well. Cases III and IV were designed using 5 major frequencies (Figures 4.7 (a) and (b)): 7, 9, 11, 13, and 15 kHz. In order to observe the change of phase velocity of surface wave at 15 kHz, a wavelet kernel in 15 kHz was made. The composite wave includes larger energy at 15 kHz in case III. This combination of energy of frequencies might be changed as the MMLS3 loading increased. Case IV simulates that largest energy of frequency moves toward lower frequency and, instead, amplitude at 15 kHz decreased by 70% in Figure 4.7 (c). The corresponding WCM plots at three sensors at 50 mm spacing are presented from Figure 4.8 and 4.9. It was observed that the WCM worked well to find a correct phase velocity for 15 kHz with 3.7 ~ 5.3% any error in the cases III and IV.

Table 4.3 Elements of Synthetic Wave for Nearby Frequency Effect

Dominant Frequency, f, (kHz)		7	9	11	13	15
Phase Velocity, λ_{vph} , (m/sec)		800	850	900	950	1,000
Attenuation Coefficient, σ		0.3	0.3	0.3	0.3	0.3
Amplitude	Case III	0.3	0.5	0.6	0.8	1
	Case IV	0.4	1	0.6	0.5	0.3

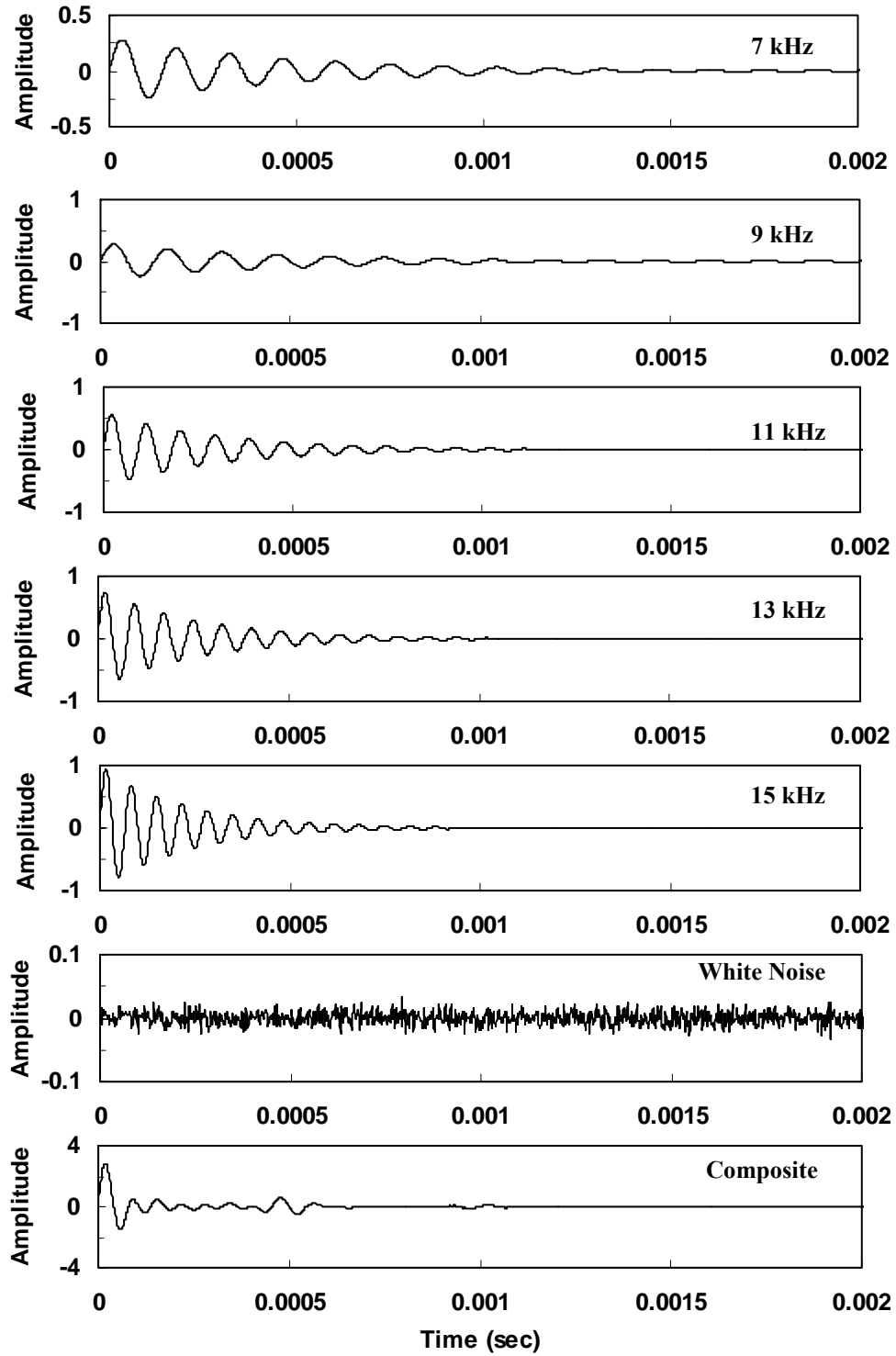


Figure 4.7 (a) Component and Composite Waves for Case III

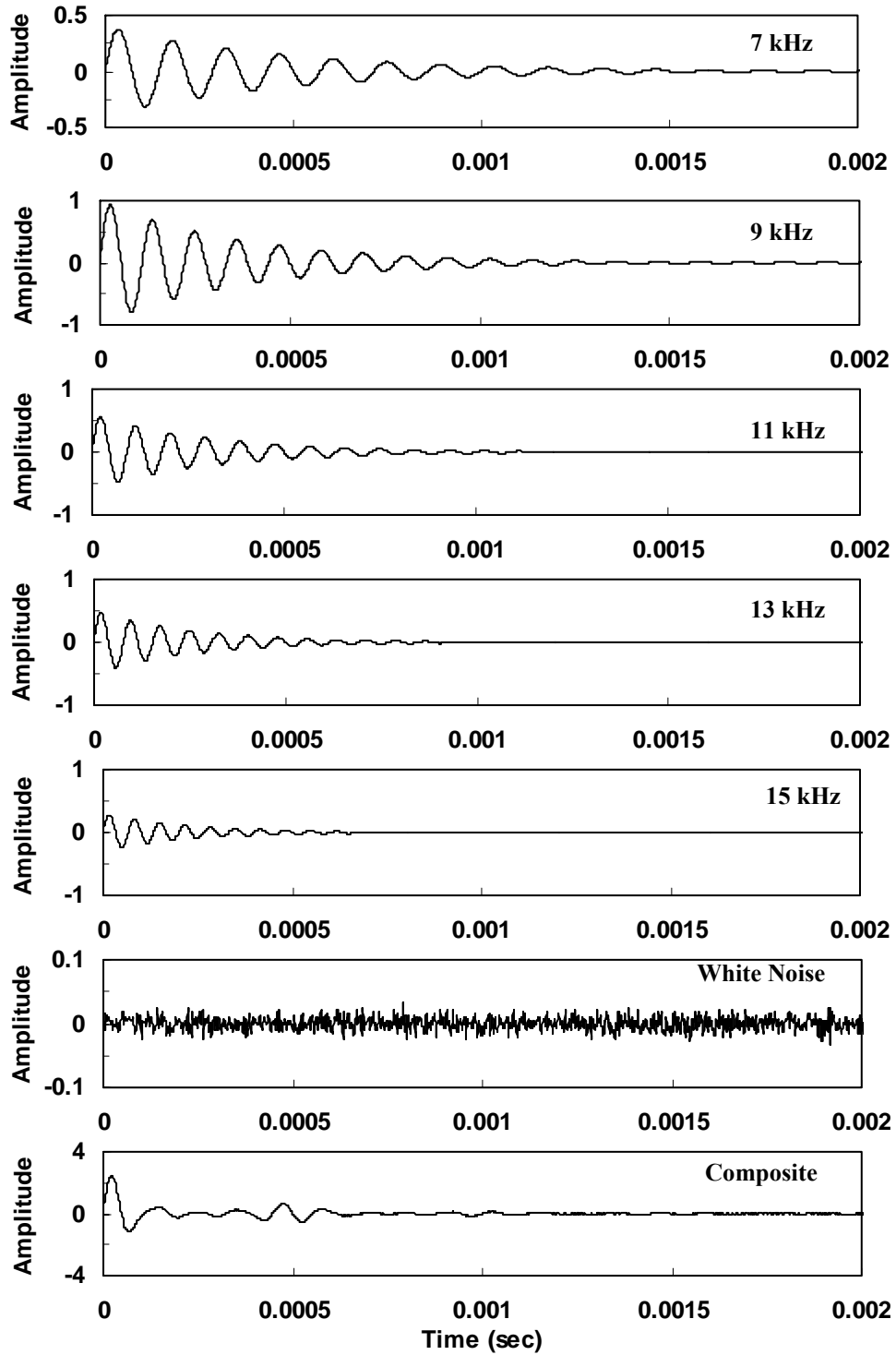


Figure 4.7 (b) Component and Composite Waves for Case IV

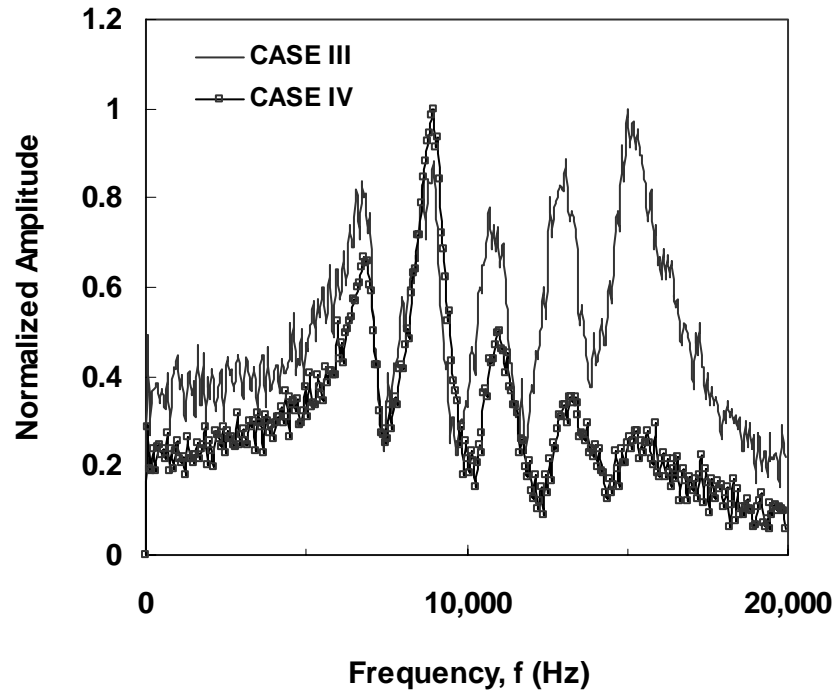


Figure 4.7 (c) Frequency Analysis for Cases III and IV

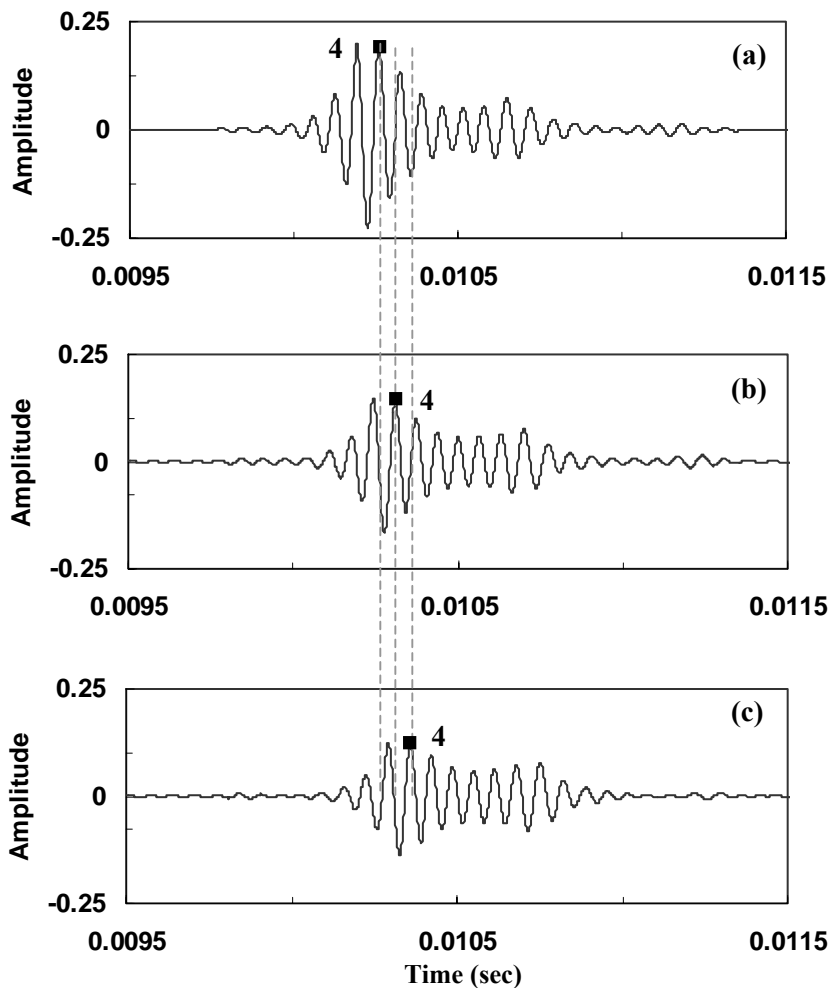
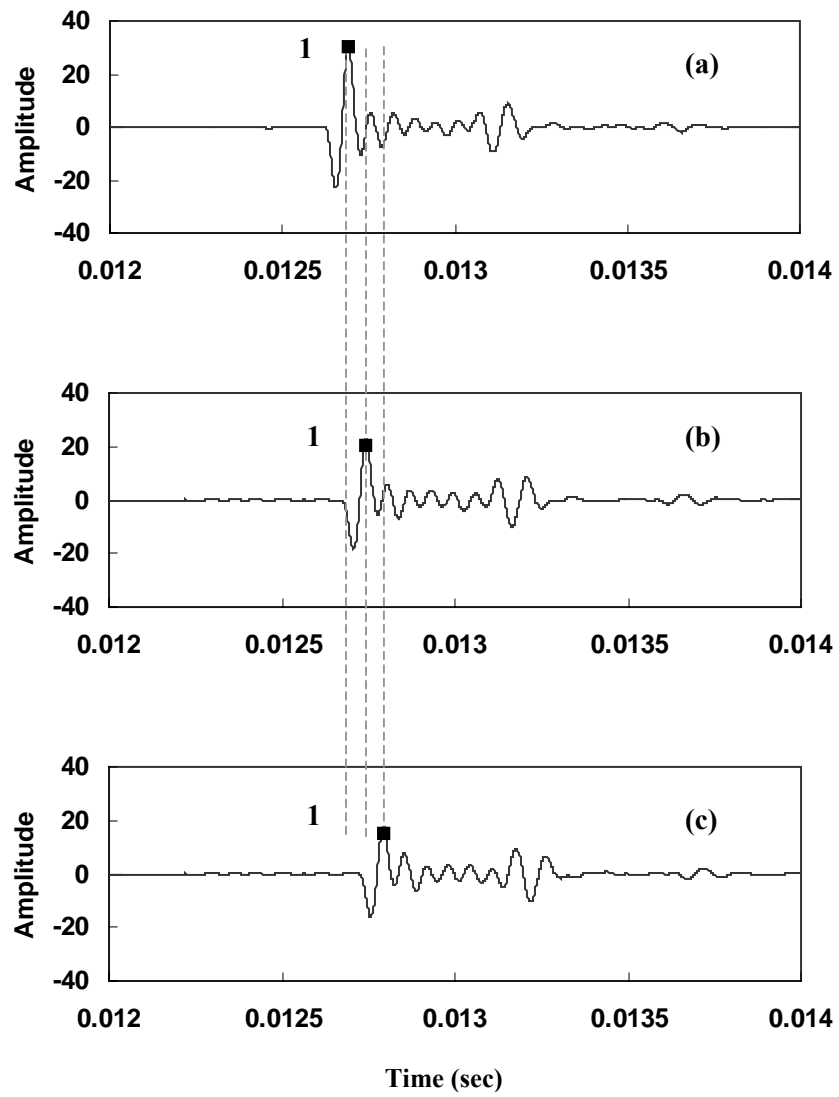


Figure 4.8 (a) Case III: WCM Transformed at:
 (a) 1st channel (b) 2nd channel (c) 3rd channel



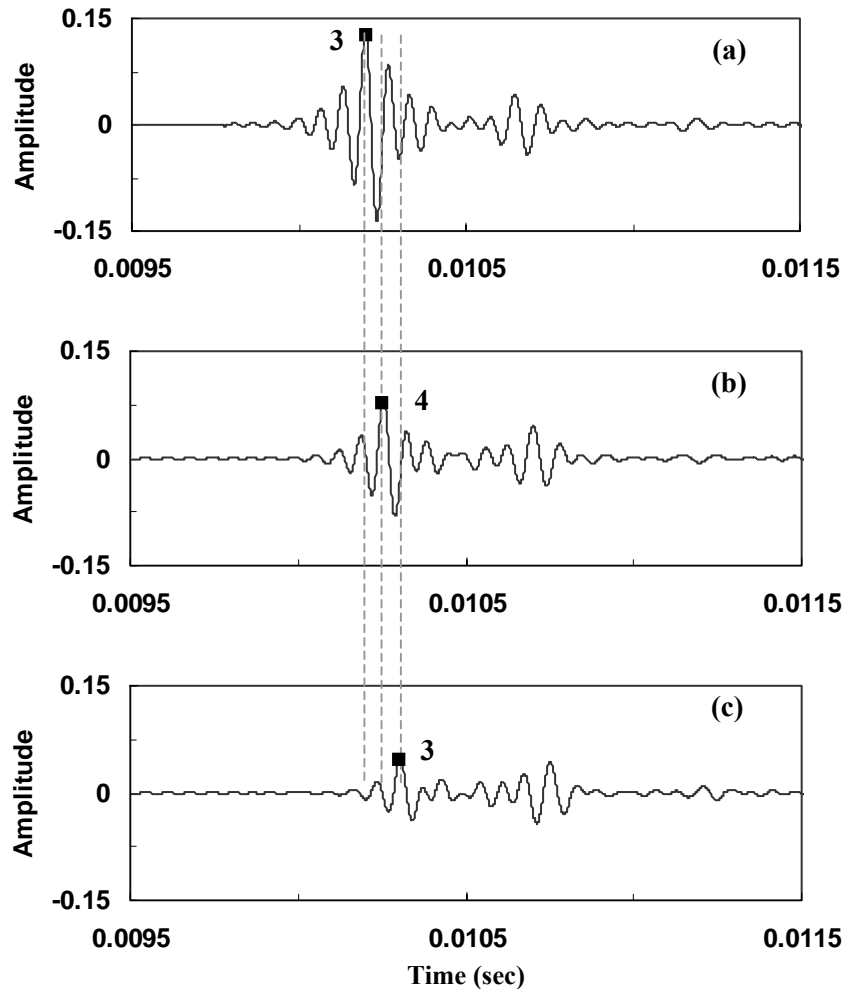


Figure 4.9 (a) Case IV: WCM Transformed Waves at:
 (a) 1st channel (b) 2nd channel (c) 3rd channel

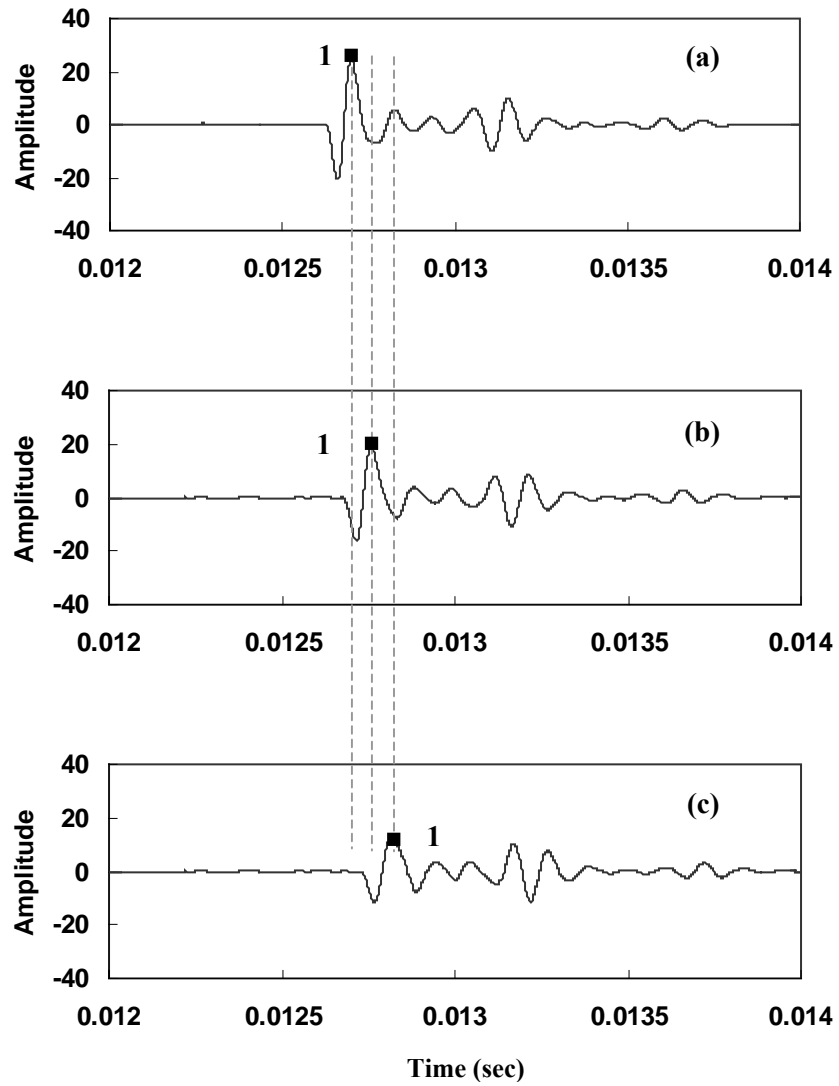


Figure 4.9 (b) Case IV: SKM Transformed Waves at:
 (a) 1st channel (b) 2nd channel (c) 3rd channel

Table 4.4 (a) Phase Velocity Calculations for Cases III and IV Based on WCM

CASE	PEAKS	Sensors				Predicted Velocity (0.05 / Δ_{t1-2}) (m/sec)	Input Velocity (m/sec)
		1	Δ_{t1-2} (10^{-5})	2	3		
		Arrival Time (sec)					
III	333	0.010194	5.2	0.010246	0.010296	962	1000
	444	0.010262	5.0	0.010312	0.01036	1000	
	555	0.010326	5.0	0.010376	0.010426	1000	
IV	223	0.010134	5.4	0.010188	0.010238	926	
	334	0.010200	5.6	0.010256	0.010306	893	
	445	0.010268	5.6	0.010324	0.010372	893	

Note: Δ_{i-j} = traveling time (sec) between channel i and channel j

Table 4.4 (b) Phase Velocity Calculations for Cases III and IV Based on SKM

CASE	PEAKS	Sensors				Predicted Velocity (0.05 / Δ_{t1-2}) (m/sec)	Input Velocity (m/sec)
		1	Δ_{t1-2} (10^{-5})	2	3		
		Arrival Time (sec)					
III	111	0.012694	5.2	0.012746	0.012796	962	1000
IV	111	0.012702	5.8	0.01276	0.012818	862	

Note: Δ_{i-j} = traveling time (sec) between channel i and channel j

4.3.4 STRENGTH AND WEAKNESS OF WAVELET CORRELATION METHOD

The overall capability in performance of the WCM was verified through several case studies in 4.3.2. In addition, understanding the strengths and weaknesses of the WCM is of importance for hands-on use in the field.

STRENGTHS

- The transformed wave using the WCM results in *narrow* bandwidth of frequencies. Thus, phase velocity from peak-to-peak calculation at sensors would little change by peak selection. In Table 4.2 and 4.4, an analysis of generated data sets suggested that there was very little difference (less than 5 %) in the calculated phase velocity as a function of the particular peak selected.
- When a dominant frequency (i.e., a frequency including largest energy) changes toward lower frequency during the damage process, the results produced by the WCM would not be much influenced because the nearby frequencies effect is small.
- As pavement damage develops during MMLS3 loading, the stress wave shape may be subjected to distortion. As for phase velocity calculation from a “bad-shaped” wave, the WCM can still provide more chances to find corresponding peaks using a wavelet having many fluctuations. Thus, the WCM is a stable procedure.

WEAKNESSES

- A phase velocity from the WCM is calculated based on a center peak which has the maximum amplitude due to the largest energy in wavelet recorded at each sensor. When the energy at the center peak in the wave is not significantly

different from adjacent peaks, the corresponding peak selection at the adjacent sensor may be unclear.

- As for low frequency analysis, i.e., mostly 100 Hz or lower, the wavelet may not provide the desired accuracy because its shape is not sharp enough, so the dominant frequency can be imprecise to target.

4.4 TESTING SETUP AND INSTRUMENTATION

Stress wave testing was applied as one technique for fatigue performance investigation using the MMLS3. Suitable impact source and powerful filtering technique are necessary to assess the response of the surface on thin pavements in testing. The general arrangement of the impact source, accelerometers, and signal processing equipment used is shown schematically in Figure 4.10. The accelerometers have magnetic adapters that allow them to couple to a 10 mm diameter steel disk which is glued to the AC pavement before loading. Sensors were connected to a Tektronix oscilloscope that acquired data once the first accelerometer was triggered by a signal produced from an impact on the pavement. The data were stored in the computer through the Stress Wave Analysis Program (SWAP) which is capable of performing the Fast Fourier Transform (FFT) and Short Kernel Method (SKM) analyses. An effective impact device was chosen for generating a surface wave in the desired frequency range. According to Heisey et al. (Gucunski et al, 1982), following criteria may be used to determine an approximate range for sensor spacing:

$$\frac{\lambda_{Vph}}{3} < X < 2\lambda_{Vph} \quad (4.9)$$

where, λ_{Vph} = the wavelength of phase velocity.

Based on an AC layer thickness of 45 mm and a dominant frequency of 19 kHz, since the wavelength, λ_{Vph} , is approximately 55 mm (1050 (m/sec) / 19,000 (Hz)), using Eq. 4.9, the sensor spacing should be between 18 mm to 115 mm. Accordingly a sensor spacing of 50 mm was selected.

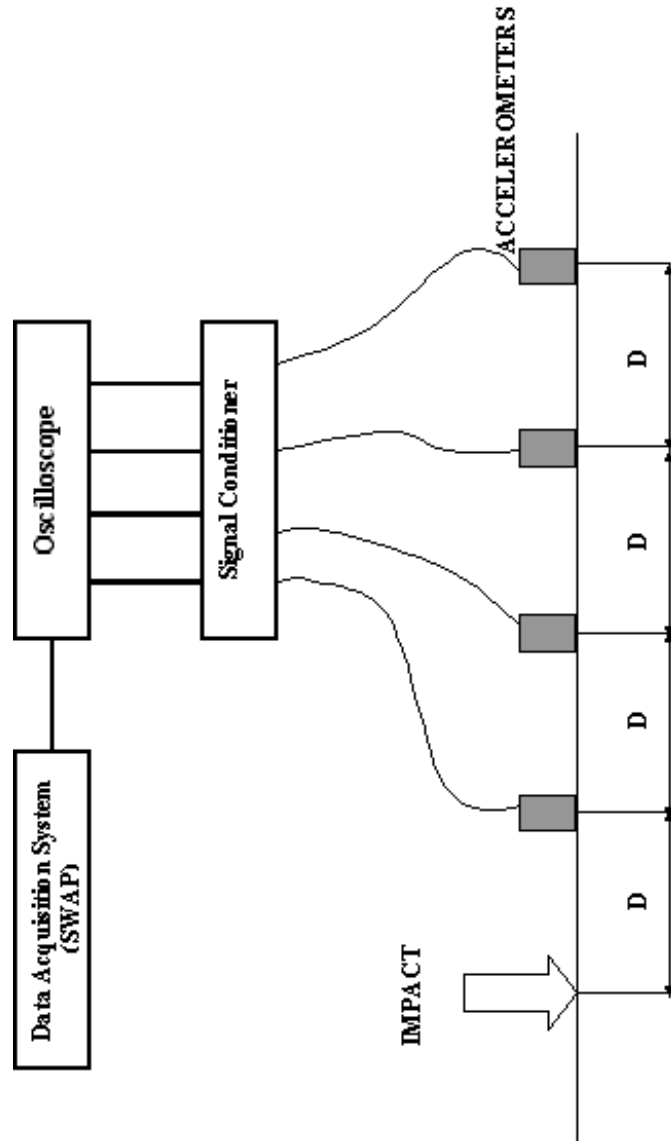


Figure 4.10 Schematic Diagram of Stress Wave Experimental Setup

4.5 COMPONENTS OF STRESS WAVE ANALYSIS

As stress wave tests were performed based on the testing procedures illustrated in Section 3.3 and the following components were analyzed.

4.5.1 DISPERSION ANALYSIS

Surface waves propagate to different depths in semi-infinite media as a function of wavelength. Longer wavelengths reach deeper into the system. Since a pavement constitutes a layered structure with varying moduli, a surface wave with multiple frequencies will propagate through the various moduli layers as a function of the component frequencies. These velocities as a function of frequency are called the *phase velocities*. The dispersion curve in Figure 4.11 shows the relationship between phase velocity and frequency. While the dispersion curve in Figure 4.12 represents the relationship between phase velocity and wavelength.

In this study, as the surface waves penetrate down to the base through an AC layer, the rate of propagation of these waves is influenced by the properties of all the layers. However, if the surface waves are composed of sufficiently high frequencies, they travel within the surface layer. Since the layer of interest in this study is the AC surface layer, it is beneficial to identify an impact method that generates high frequency surface waves that remain within the AC layer. As described in Appendix A, various impact devices were tried for this purpose. For example, a marble dropped through a 20 cm tall pipe created surface waves with a dominant frequency of 12 kHz, lower than the desired. Impact of a marble on cylindrical steel rod created waves with dominant frequencies in the range of 16k ~ 19k Hz. This range was considered to be acceptable, based on the representative frequency discussed in the following section. Based on a dominant

frequency content of 16k to 19k Hz, the calculated wavelengths at 20°C are approximately 60 to 40 mm.

4.5.2 REPRESENTATIVE FREQUENCY DETERMINATION

The change in phase velocity with increasing frequency shown in Figure 4.11 is probably related to the fact that, at frequencies lower than 13 kHz, the surface waves sample more from the neoprene base, that is the material below the AC layer. Since the modulus of the neoprene base is much lower than that of the AC layer, lower frequencies result in slower phase velocity.

According to Roesset (1990), the top flat portion, “plateau”, of the curve confirms that surface waves with frequencies over 13 kHz travel mainly in the AC surface layer and the constant phase velocity at higher frequency represents the linear elastic properties of the AC layer without disturbance from lower layers.

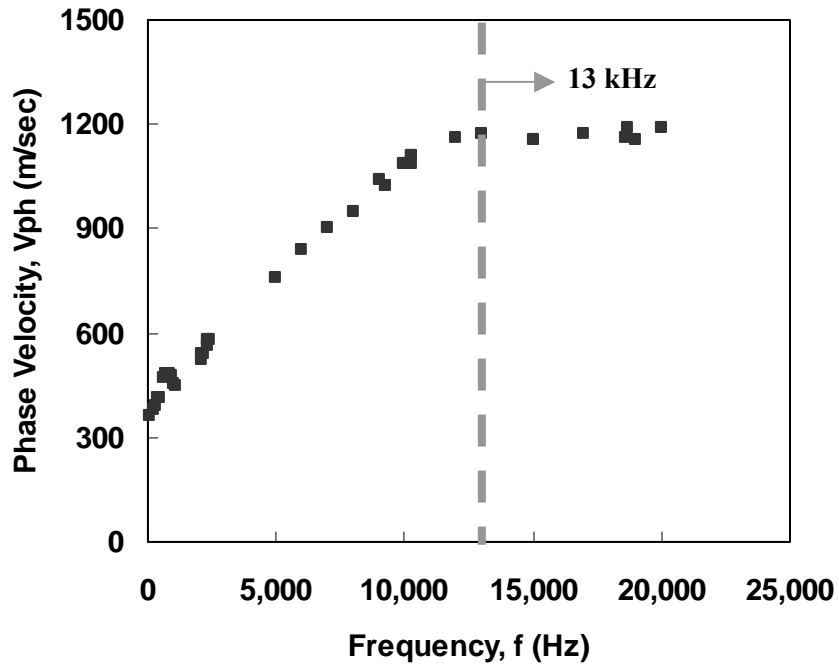


Figure 4.11 Dispersion Curve by WCM for RI-1 Pavement

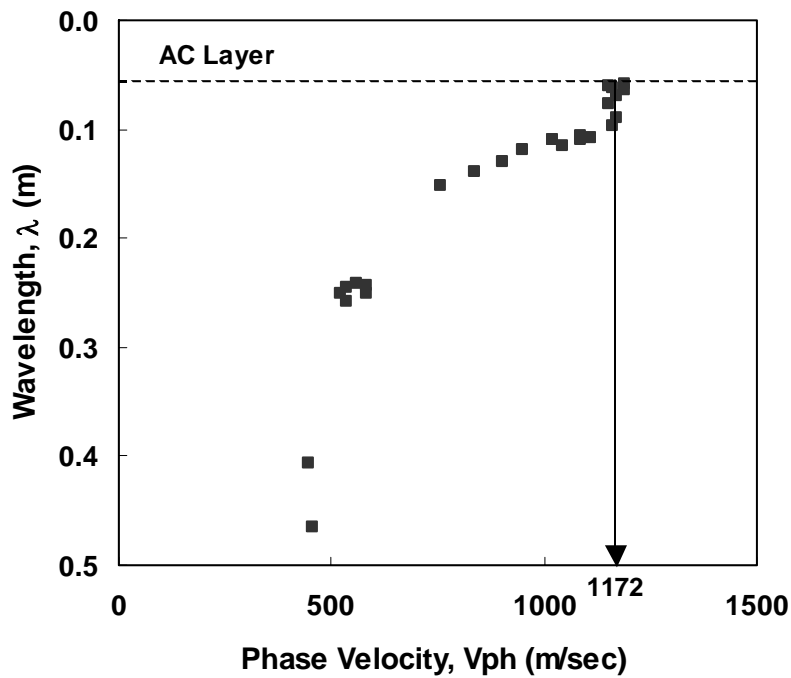


Figure 4.12 Dispersion Curve in Wavelength and Phase Velocity Relationship for RI-1 Pavement

Hence, that frequency and corresponding short wave lengths can be used for the calculation of the shear wave velocity and therefore the stiffness of the AC layer, as Figure 4.12 represents. Any frequencies higher than the 13 kHz thereby result in the similar phase velocity from which the AC modulus may be determined directly without inversion process. This procedure has been used in the analysis of the model pavement structures tested.

The sampling depth concept of surface waves can be of help to determine representative frequency. The sampling depth is about $\frac{1}{2}$ of the wavelength and that, by the time surface waves propagate to the depth equal to one wavelength, it is known that 90% of the energy is consumed (Richart and Woods, 1960, Nazarian et al, 1990). Strictly speaking, when one wavelength of surface wave is equal to or shorter than AC layer thickness, the representative frequency for the AC layer can be selected. However, since the energy consumption rate rapidly increases with sampling depth, when the sampling depth falls within AC layer, the frequency of surface wave may be accepted as a representative frequency. The observation makes the marble impact method on steel plate that results in about 60 ~ 80 mm wavelengths at a frequency range of 14 ~ 19 kHz for R11 pavement. For the stress wave of at least 16 kHz, its half of wavelength, sampling depth (37 mm), is shorter than the fatigue layer thickness of 40 mm used in the fatigue tests. Thus, according to both criteria, wavelet of 16 kHz or above is recommended to use for AC layer characterization.

4.5.3 MICRODAMAGE HEALING

In addition to fatigue damage, microdamage healing of asphalt concrete due to the introduction of rest periods was studied through laboratory experiments using stress wave techniques. The effect of a rest period is to extend the fatigue life of the asphalt concrete. In order to investigate the recovery from damage, stress wave data were collected at intervals during rest periods of up to approximately 1800 sec (30 min) at 11510, 67870, 183070, and 281960 wheel applications, respectively.

The major observation that can be made from Figure 4.13 is the upward shift of data points increase in phase velocity after rest periods while the temperature of the pavement remained between 20.5 ~ 21.5°C. There is a possible reason that can explain the changes in measured phase velocities. During rest periods, due to the inherent viscoelastic nature of the AC, deformations in the asphalt layer relax, and the microstructure of asphalt concrete changes by healing of micro-cracks, resulting in increased stiffness and resultant phase velocities.

To compare the amount of healing observed after different number of wheel applications, the healing index is defined as (Kim, 1998):

$$\text{Healing Index} = \frac{V_{after} - V_{before}}{V_{before}} \times 100 \quad (4.10)$$

where V_{before} : phase velocity right after completion of wheel loading, and

V_{after} : phase velocity after a rest period

From Figure 4.14 (a), it was observed that fatigue loading stages before visible crack occurrence at 183,000 wheel repetitions showed a relatively fast healing rate (greater than 0.01). However, Figure 4.14 (b) suggests that it does not result in a greater magnitude of

microdamage healing while macro-cracks develop. Generally, healing index gradually goes down in trend as wheels applications are added.

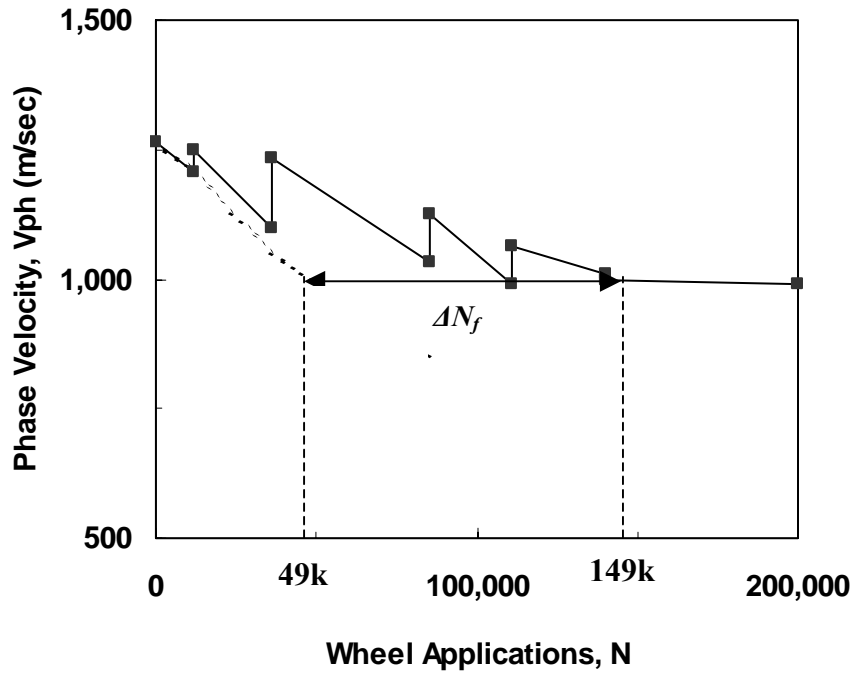


Figure 4.13 Changes in Phase Velocity during Fatigue Loading for I19C-A Pavement (8.7% AV Section)

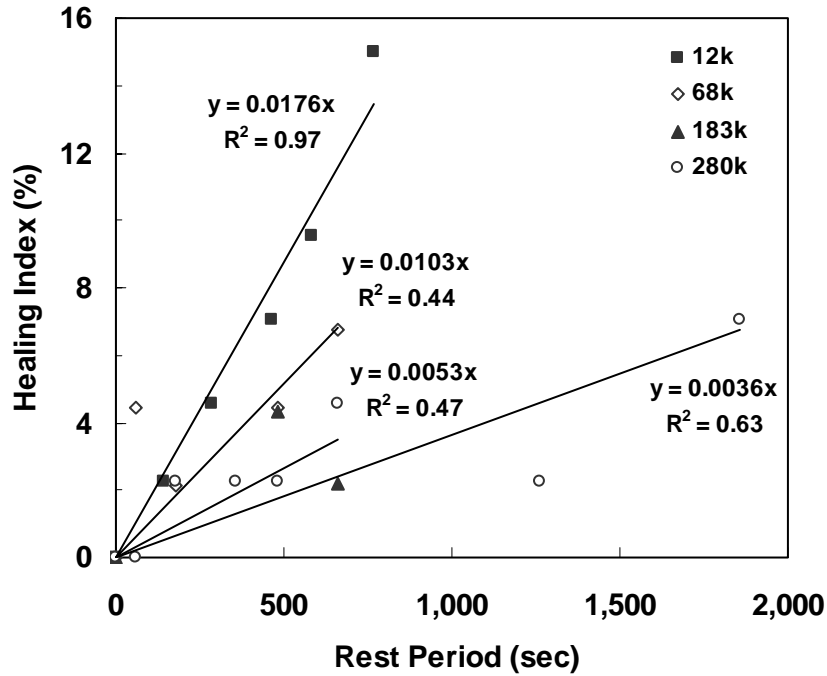


Figure 4.14 (a) Changes of Healing Index along Rest Period at different Load Levels for RI-1 Pavement

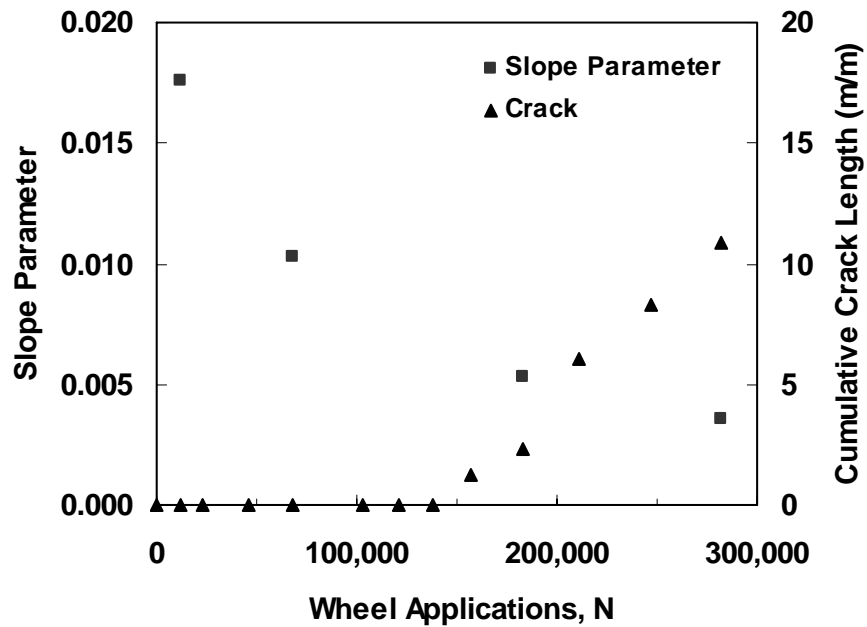


Figure 4.14 (b) Slope Parameter from Regression Analysis for Healing Indices and Cumulative Crack Length Profile as a Function of Wheel Applications for RI-1 Pavement

4.5.4 NONDESTRUCTIVE STIFFNESS EVALUATION ON THIN PAVEMENT

Figure 4.15 presents the surface wave test results from each slab for the entire fatigue period. It can be observed that the AC modulus decreases as the number of load cycles increases. Except for RI-2 pavement, the early reduction in the elastic modulus of other 40 mm thick pavements may be explained through structural degradation of pavements due to microcrack initiation and propagation. Since an RI-2 pavement is a 60 mm thick, the initial densification due to the MMLS3 loading until 260,000 wheel applications would increase the phase velocity and then structural degradation occurred. Figure 4.15 demonstrates that fatigue damage was in progress in the pavements because of a decrease in modulus, a symptom of damage evolution. In comparison to visible surface cracking, it was found that surface cracks arose when the phase velocity of the pavement decreased to approximately 50% of the initial values regardless of the different physical properties of the pavement such as air void content, aggregate gradation, etc.

In the study by Kim (1998), stress wave tests were conducted on a 102 mm thick pavement with an AC-5 surface layer. This pavement was constructed at the FHWA Turner-Fairbank Highway Research Center in McLean, VA and was loaded by ALF, a full-size APT device. The phase velocities found in the ALF study are compared in trend to the stress wave results obtained in this study using the MMLS3 on the RI-1 pavement. In Figure 4.16, phase velocities at the center of the wheel-trafficked area and the cumulative crack length are plotted against the number of wheel applications for both the MMLS3 and ALF. It can be observed that the phase velocity (and therefore AC stiffness) decreases as the number of loading cycles increase in both cases of the MMLS3 and ALF. The Figure 4.16 demonstrates that prior to the appearance of visible surface cracks,

which occurred after 125,000 load applications, the phase velocities had already significantly reduced. That reduction in velocity indicates model test structural degradation to be similar in character, although at a somewhat slower initial rate than observed for the ALF results. This observation suggests that the proposed NDE technique using WCM stress wave may be successfully implemented to investigate fatigue damage evaluation of especially thin AC layer such as used in AC overlays. This process may allow the optimum time for maintenance/rehabilitation of a thin AC layer pavement to be determined before cracks appear on the pavement surface.

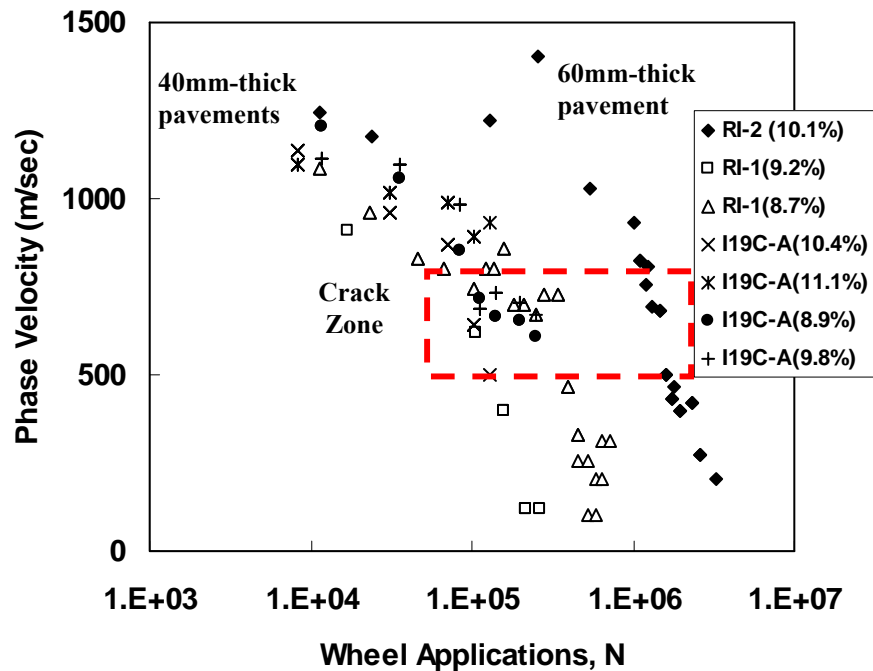


Figure 4.15 Phase Velocities versus Cracking

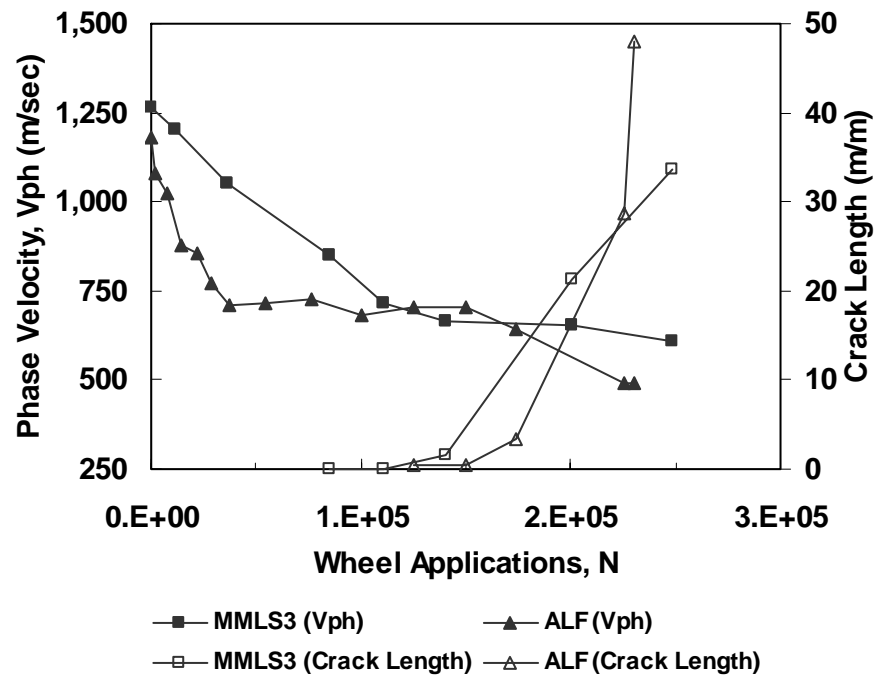


Figure 4.16 Phase Velocity (No Rest Periods) and Cumulative Surface Crack Length as a Function of Number of Wheel Applications: (a) MMLS3 and (b) ALF (Kim, 1998)

4.6 SUMMARY

Stress wave analysis was outlined in this Chapter. The WCM was newly introduced and its performance for signal processing analysis was assessed. The stress wave testing condition was established and material characterization using WCM was performed. Consequently, damage growth and healing effects of the model pavements were evaluated throughout the fatigue test.

CHAPTER 5

FATIGUE PERFORMANCE INVESTIGATION

5.1 INTRODUCTION

Fatigue cracking due to repeated loading has been regarded as an important distress type in asphalt concrete (AC) pavements. Designing a pavement structure that provides better resistance to fatigue cracking requires extensive laboratory testing and evaluation. Since the verification of pavement design and construction methods may take several decades using conventional methods, more economical and reliable alternatives have been explored.

The evolution of fatigue damage in laboratory asphalt pavements has been investigated using the MMLS3. Research was carried out to see the possibility of using a scaled-down accelerated pavement testing (APT) device to induce the realistic fatigue phenomenon and to propose an empirical fatigue life prediction methodology. Laboratory pavements were initially designed with the aid of a multi-layered linear elastic program. Indirect tension tests (IDT) were accompanied to determine engineering material characteristics after MMLS3 pavement testing.

After trial slabs were constructed and tested, the MMLS3 test setup and analysis techniques were established. An AC surface layer was constructed using a vibratory rolling compactor in the laboratory and was placed on a neoprene base that rested on a stiff layer consisting of a steel plate. This layered system has the advantages of being easy to construct and producing consistent thin pavements for fatigue testing with the MMLS3.

The MMLS3 has a wheel-wandering mechanism, which provides lateral wheel movement perpendicular to the traffic direction to minimize rutting. Wandering of the 100 mm wide wheel resulted in a wheel path of 180 mm in width. To achieve a normal lateral distribution of wheel loading, displacement increments were programmed to occur at constant intervals. As discussed in Chapter 4, deterioration of the asphalt layer due to this fatigue loading was periodically monitored through the nondestructive wave evaluation technique. This stress wave propagation method enabled the direct measurement of changes in the stiffness of the asphalt surface layer due to fatigue damage growth. Accurate evaluation of the changes in material properties within the asphalt layer would be of help to practically indicate the magnitude of fatigue damage in asphalt pavements. An increase in the tensile strain at the bottom of the slab was believed to be a significant measurement for evaluating the fatigue performance of a thin pavement. A fatigue life prediction protocol based on cumulative damage analysis is proposed and compared with results from the pavements tested.

The impact of pavement construction deficiencies on service life can be assessed using the pavement response prediction for known material properties and structural conditions. A framework using a laboratory testing program is introduced to predict the service life based on fatigue performance. This can be accomplished through determining material properties and parameters in the pavement structure. As a practical approach, the fatigue failure of a laboratory pavement subject to MMLS3 loading was predicted using an indirect tension testing program that was designed to determine appropriate material properties and parameters.

Finally, the scaled-down nature of the MMLS3 is shown to possess potential on instrumented pavements for calibration and/or verification of material constitutive models and pavement performance prediction models.

5.2 BACKGROUND

5.2.1 ASPHALT INSTITUTE FATIGUE LIFE PREDICTION MODEL

The most widely used laboratory-based fatigue equation was developed by the Asphalt Institute (Huang, 1965). This fatigue model is used in determining pavement service life. This phenomenological relationship, based on the constant stress criterion, is expressed as:

$$N_f = C \cdot f_1(\varepsilon_t)^{-f_2} |E^*|^{f_3} \quad (5.1)$$

where,

- N_f = fatigue service life of pavement
- C = the correction factor,
- ε_t = the tensile strain at the bottom of the AC layer, and
- $|E^*|$ = the dynamic modulus of the AC layer.

The Asphalt Institute suggests 0.0636, 3.291, and 0.854 for f_1 , f_2 , and f_3 , respectively, for a thin HMA layer less than 102 mm in thickness. The correction factor, C , is represented as:

$$C = 10^M \quad (5.2)$$

where,

$$M = 4.84 \left(\frac{V_b}{V_a + V_b} - 0.69 \right) \quad (5.3)$$

V_b = asphalt volume, and
 V_a = air void volume.

5.2.2 *INDIRECT TENSION TESTING (IDT)*

The indirect tension test has been extensively used in structural design research for flexible pavements since the 1960s. The advantage of this test is that cores from thin lifts can be tested directly in the laboratory. The IDT is devised to develop tensile stresses along the diametral axis of the test specimen, as shown in Figure 5.1. A compressive load is applied on a cylindrical specimen through two diametrically opposed, arc-shaped rigid platens (NCHRP report 465).

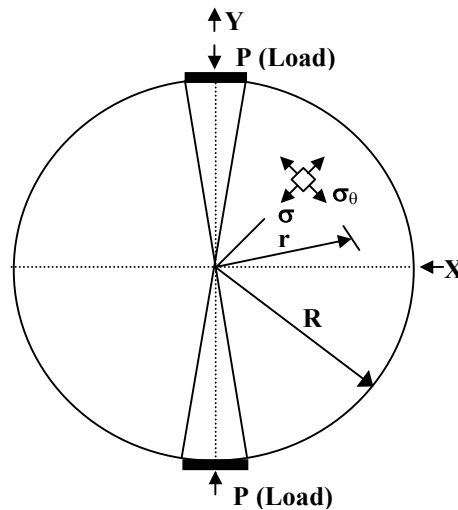


Figure 5.1 Schematics of the IDT (NCHRP 465)

As a fingerprint, the dynamic modulus test using IDT is conducted before IDT fatigue testing. The dynamic modulus test consists of a haversine loading applied to the specimen, as described in more detail in Appendix B. The load amplitude is adjusted based on the material stiffness, temperature, and frequency of loading to keep the strain response within the linear viscoelastic range. The load is applied until steady-state is

achieved, at which time several cycles of data are collected. From the frequency sweep test, the complex modulus, E^* , the dynamic modulus, $|E^*|$, and the phase angle, ϕ , can be determined. The dynamic modulus is the amplitude of the complex modulus. As the testing temperature decreases or the loading rate (frequency) increases the dynamic modulus will increase and the phase angle will decrease due to the time dependence or viscoelasticity of the material.

5.3 FATIGUE LABORATORY PAVEMENT CONSTRUCTION DEVELOPMENT

5.3.1 *EVOLUTION OF PAVEMENT SYSTEM FOR THE MMLS3*

To investigate realistic fatigue phenomena, four trial slabs were designed, constructed, and loaded. The first slab was intended to work as a fatigue control slab for the purpose of understanding the equipment and necessary test procedures. To model the successful testing with ALF by Kim (1998), the slab was constructed using a 3-layer system consisting of an AC layer with the NC Superpave mixture, a 160 mm thick aggregate base course, and a sand subgrade. Since the thickness of the AC layer, as a rule of thumb, was recommended to be at least 3 times larger than the nominal maximum size of aggregate (12.5 mm), the selected thickness was 40 mm. Even after 2.5 million axles of 2.1 kN load were applied over 2 weeks, no sign of a decrease in wave propagation velocity (i.e., stiffness) or cracking was apparent.

Along with modifications to the testing procedures is used on the first slab, the thickness of the second AC pavement layer was increased to 80 mm to give greater sampling depth for increased surface wave reliability. To expedite fatigue damage in this pavement, the base course was removed. Therefore, the second model pavement was

composed of two 40 mm asphalt lifts on sand. Even six million wheel applications over 3 months did not produce any fatigue cracks.

After the first two slabs had shown no measurable fatigue damage, a thinner surface layer was considered. Also, the construction difficulties that arose from the use of an aggregate base or sand subgrade were reconsidered. These deliberations resulted in the third pavement design. Six 25 mm thick D60 neoprene sheets with a modulus of 360 Mpa were used as a substitute for the aggregate base. The neoprene base was particularly helpful during pavement construction because only the top sheet had to be replaced with a new sheet between subsequent tests. For the third model pavement, a 60 mm AC layer was compacted on a wooden formwork and then carefully transferred without the introduction of any visible cracks onto the neoprene layers (150 mm thick) which rested on a 20 mm steel plate. The 3 m × 1 m plate was underlain by sand. A tack coat was applied between the neoprene base and the asphalt slab to ensure good bonding between these layers. After over 1.5 million wheel applications, longitudinal hairline cracks were observed, but the fatigued pavement did not show an alligator-crack pattern.

An apparent fatigue alligator crack pattern, however, was produced in the fourth slab which had a 40 mm thick AC layer. To satisfy the minimum required sampling depth for application of the surface wave technique described in Section 4.5.2, high frequency impact methods were investigated. Schematics of the four slabs described are presented in Figure 5.2.

The laboratory pavements were initially designed with the aid of a multi-layered linear elastic program. However, the final structural design for the accelerated fatigue testing using the MMLS3 was optimized through several trials.

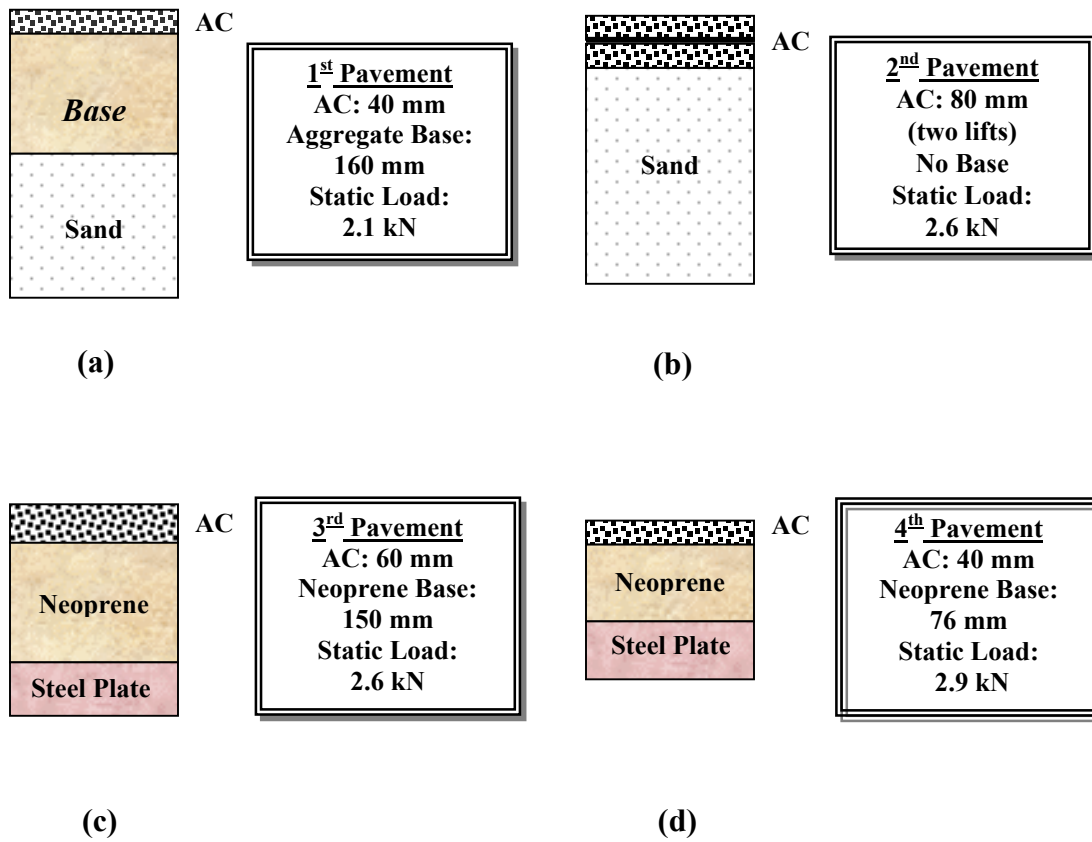


Figure 5.2 Overview of Constructed Pavements

5.3.2 *STRUCTURAL ANALYSIS FOR FATIGUE PAVEMENT USING MULTI-LAYER ELASTIC PROGRAM*

A multi-layer linear elastic program, EverStress, was used in evaluating pavement responses. This axi-symmetric linear program, provided complements of the Washington State Department of Transportation, is capable of determining the stresses, strains, and deflections in a semi-infinite layered elastic system under circular surface loads.

Seeing that the laboratory pavement developed for the MMLS3 fatigue testing consists of “artificial” layers with a neoprene base and a steel plate as a stiff layer, it possess a challenge to compare the resulting stress-strain response to that of a general pavement structure in the field. To simulate the real pavement as simply as possible, a three-layer pavement system was considered. As the MMLS3 wanders close to a normal lateral distribution of wheel loads, the wheels spend more time at the center of the wheel path than at the edge. Therefore, a comparison of compressive stresses along depth of the pavement and the tensile strain at the bottom of the AC layer at the center line of the wheel path is to be made for:

- The general pavement system with a crushed aggregate base and subgrade; and
- The laboratory pavement system with 3 layers of neoprene base on stiff layer.

It was assumed that the surface layer was well bonded to the base course. As for the laboratory pavement, while the tack coat was applied only between the neoprene and the AC surface layer, there was no bonding between neoprene layers. Material properties, such as dynamic modulus and Poisson’s ratio, for the general pavement were selected as average values from publishes and typical ranges (Huang, 1995) but actual layer

thicknesses are used from the RI-2 pavement (Huang, 1996). Layer thicknesses and chosen material properties are shown in Figure 5.3.

The surface layer thickness in both pavements was 40 mm, The 76.2 mm thickness of the base course in the general pavement is very close to that of the total thickness of these layers of neoprene of 25.4 mm (25.4 mm x 3 = 76.2 mm). As shown in Figure 5.4, the compressive stress (333 kPa) at the interface between the AC layer and the base in the laboratory pavement was 21.3% higher than the 262 kPa predicted for the general pavement. This difference is provided by the base layer of high Poisson's ratio (0.5 versus 0.4) in base layer. On the other hand, tensile strain of 318 $\mu\epsilon$ at the bottom of laboratory pavement was 34.4% lower than the 485 $\mu\epsilon$ at the same location of the general pavement. Therefore, the fatigue service life in the laboratory pavement may be shorter than in the general pavement.

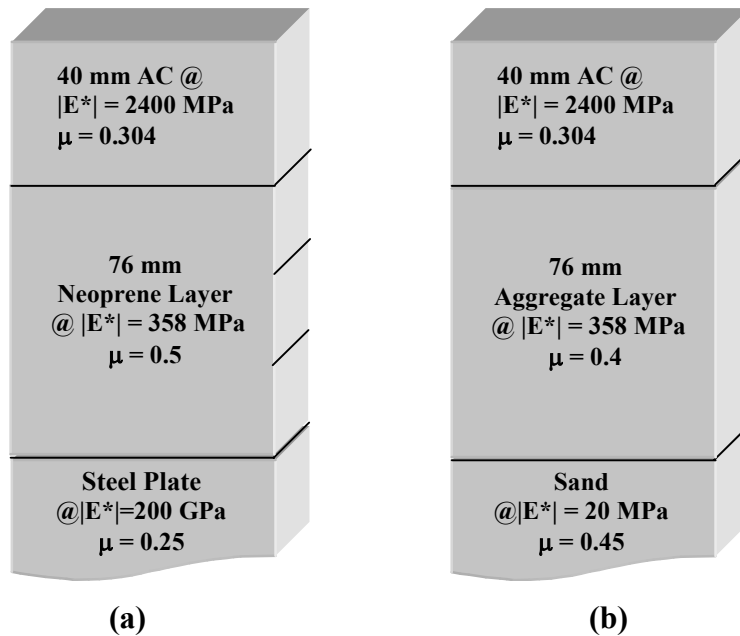


Figure 5.3 Pavement Profiles for Structural Analysis:
 (a) Laboratory Pavement (b) General Pavement

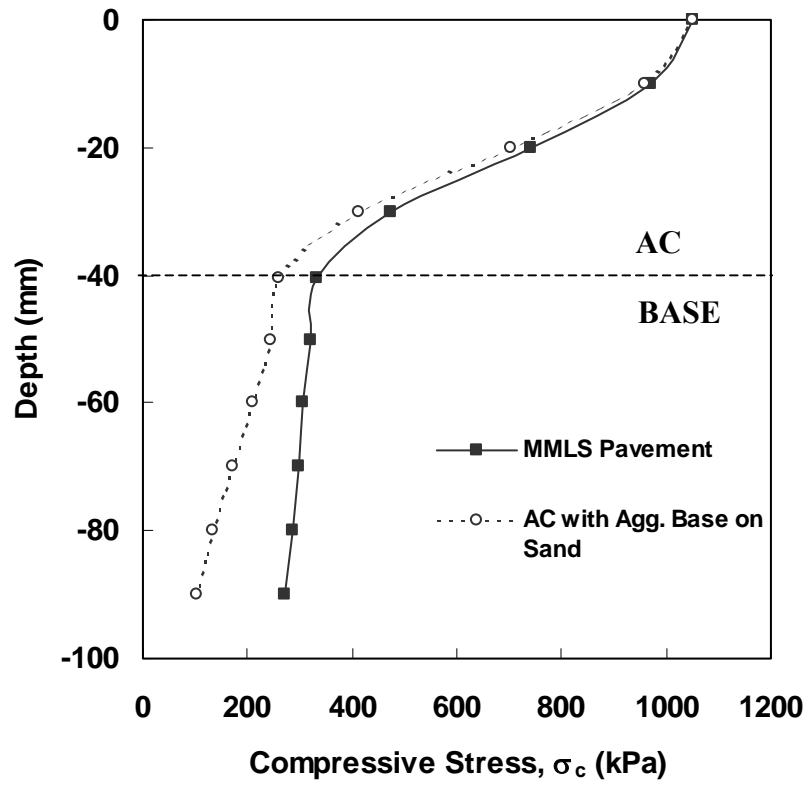


Figure 5.4 Compressive Stresses along Depth of Pavements at Center of Wheel Path

5.4 EVALUATION OF FATIGUE PERFORMANCE

5.4.1 ANALYSIS OF PAVEMENT RESPONSES

Tensile Strain

Measurements of horizontal strain response at the bottom of the bituminous layer are made by means of strip type strain gauges. Strain data were used to monitor a physical change in the pavement that can be evaluated as an increasing amount of damage. The tensile principal strain allows for a clear understanding of the overall fatigue damage development. As has been observed by Kim (1994) in indirect tension (IDT) fatigue testing of AC, Figure 5.5 shows the “trend” in the development of tensile strain at the bottom of the I19C-A pavements at different air void contents of 8.9, 9.8, 10.4, and 11.1%, as a function of the number of wheel applications. The strain increases rapidly at the initial stage and then the rate of increase of strain becomes relatively constant until accelerated to final failure. The fatigue life (N_f) was determined as an intersection between a line representing the constant growth of strain and the line fitting to the rising curve to complete failure on a log wheel load application versus linear strain plot, as shown in Figure 5.6. As a result, the relationship between number of wheel applications at failure and the air void content is represented by regression analysis in Figure 5.7. The results are summarized in Table 5.1.

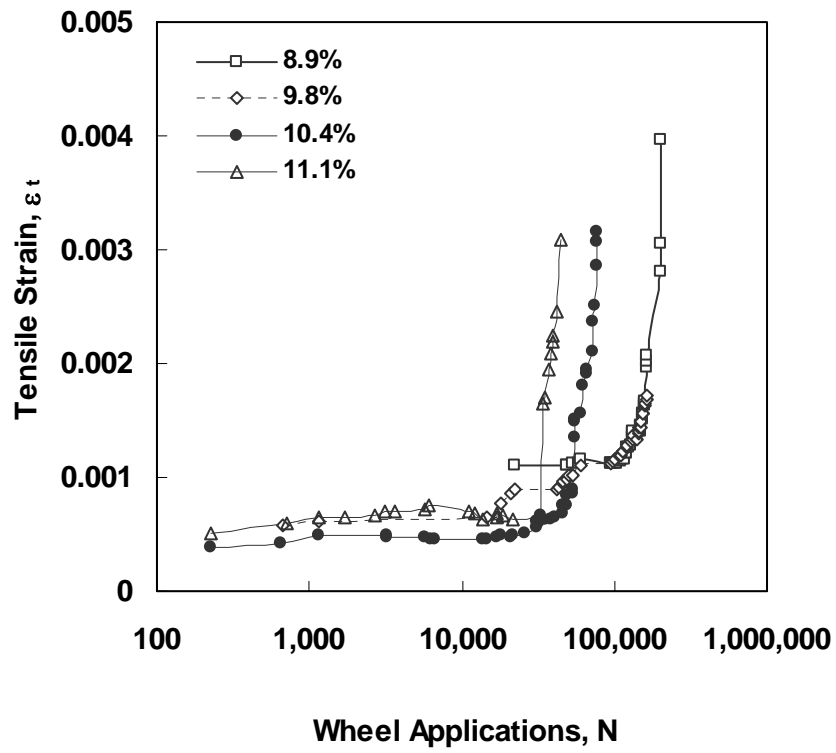


Figure 5.5 Measured Tensile Strain Profiles at Different Air Void Contents Using I19C-A Mix

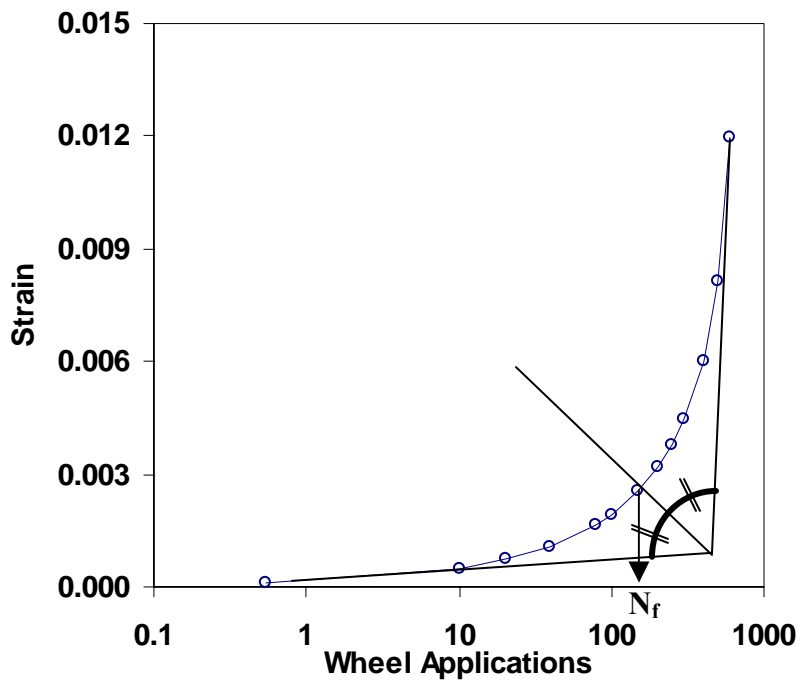


Figure 5.6 Example of Determination in Fatigue Life (NC DOT Report, 2002)

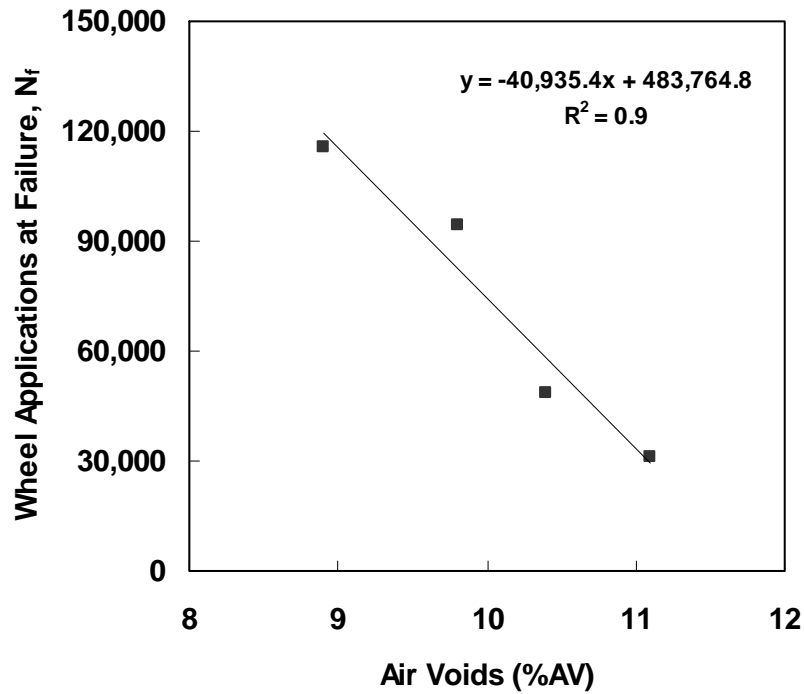


Figure 5.7 Relationships between Air Void Contents and Number of Wheel Applications at Failure

Table 5.1 Fatigue Life Analysis

Pavements	Air Void Contents (%)	N_{INI} (Wheels)	N_f (Wheels)
RI-2	10.1	1,600,570	N/A
RI-1	9.2	N/A	70,800
	8.7	156,930	N/A
I19C-A	8.9	140,260	148,966
	9.8	85,390	94,170
	10.4	31,290	48,346
	11.1	31,290	33,007

Note: N_{INI} is based on the first crack observation at measurement intervals
I19C-A stands for I19C mix prepared with aging for 4 hours

Cracking

Increase of strain indicates the damage accumulation due to repetitive loading. Fatigue failure may occur when the amount of damage reaches a certain critical value. An alligator crack pattern was observed in the fatigued pavements. In general, cracks initiate as hairline cracks along the trafficking direction and propagate slowly in the longitudinal and transverse directions until the development of a network of macrocracks that leads to failure. In Figure 5.8, fatigue performance resistant to cracking at different air void contents is shown as a function of cumulative crack length. According to Huang (1993), as the pavement reaches failure, over 50% of the loading area has already experienced fatigue cracking. The fatigue alligator cracking pattern from the RI-1 pavement is clearly shown in Figure 5.9. Interconnected cracks between the surface and the bottom of the AC layer and highlighted cracks are displayed in Figure 5.10 (a) and (b), respectively.

Stress Wave

As aforementioned in Chapter 4, stress wave technique using wavelet correlation method was adopted to monitor the change of stiffness of the AC layer as the number of load cycles increases. After the early reduction of phase velocity in advance of macro-crack advent, that may be caused by structural degradation of pavements due to micro-crack initiation, propagation, and densification as a symptom of damage evolution. The modulus after fast reduction until 24,000 wheel applications showed a gradual decrease in the trend that agreed with the findings by the full-scale tester as shown in Section 4.5.4.

Rutting

Transverse surface profile measurements using the profilometer were taken along the test grid before and after the completion of MMLS3 testing on each slab. It was observed that there was a reduction of the thickness of surface layers up to 3 ~ 5% after 150,000 wheel applications and about 6 ~ 8% after 200,000 wheel applications even using wandering system.

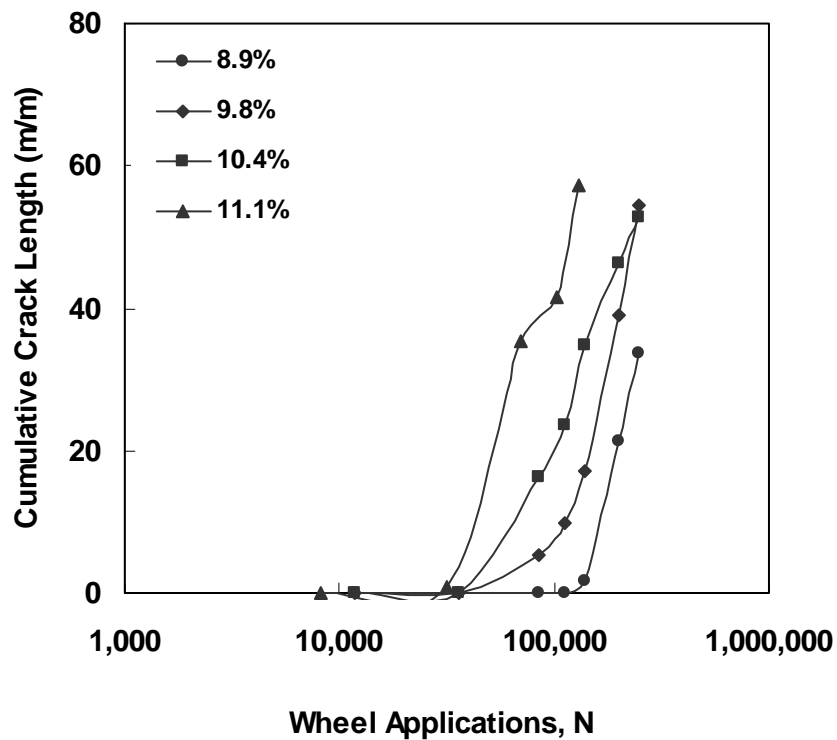


Figure 5.8 Crack Propagation at Different Air Void Contents Using I19C-A Mix

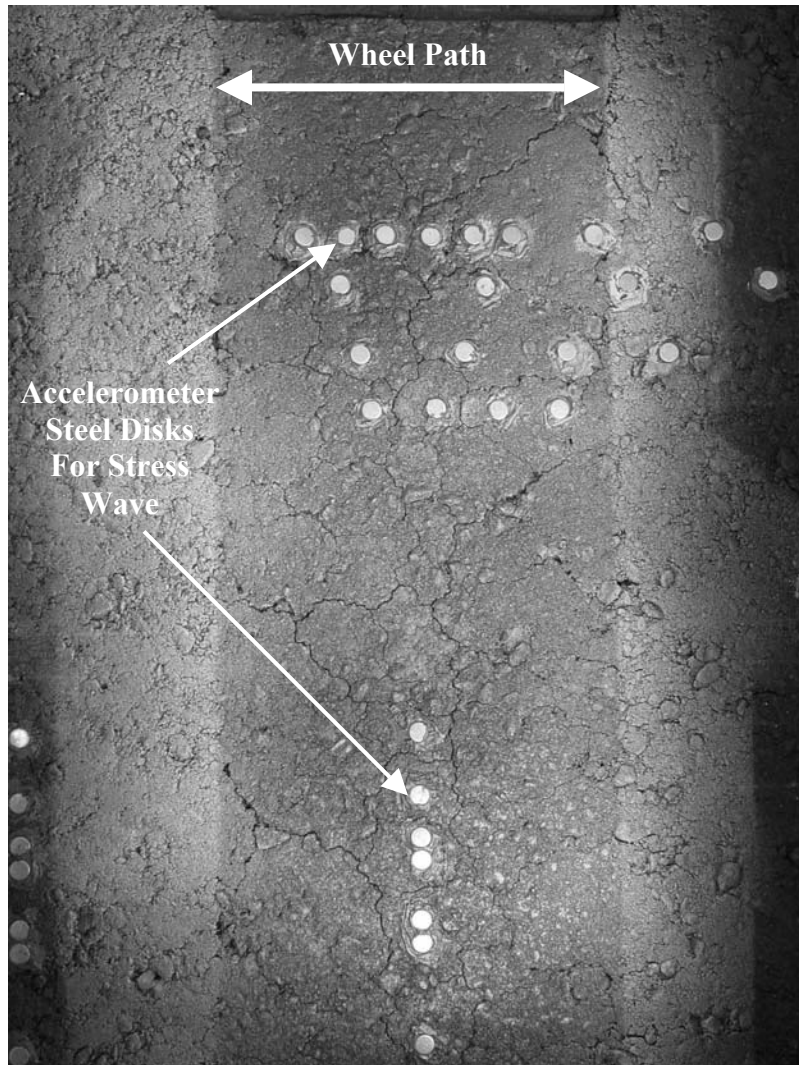


Figure 5.9 Fatigue Alligator Cracking Pattern after 250,000 Wheel Applications on the surface of RI-1 Pavement

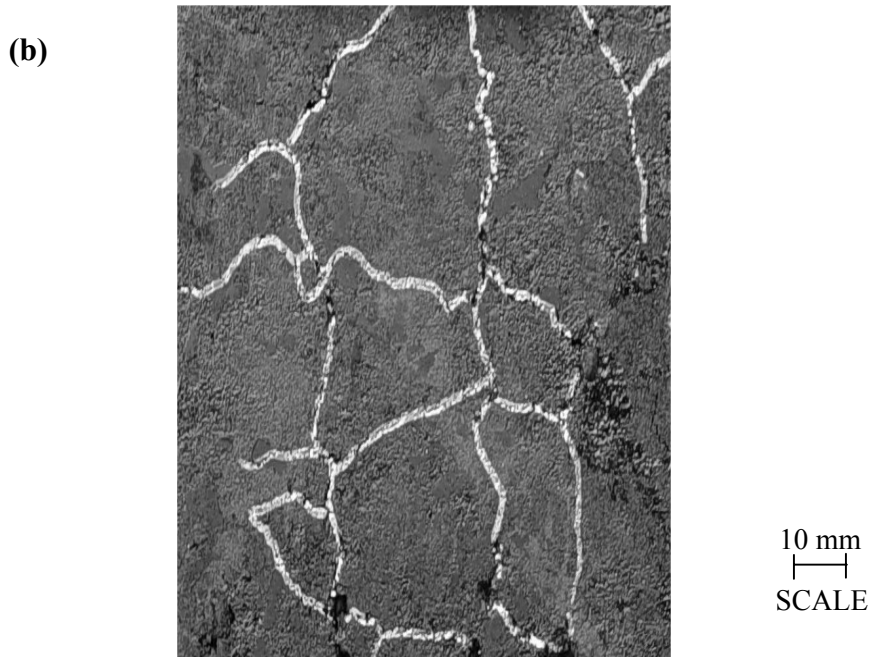
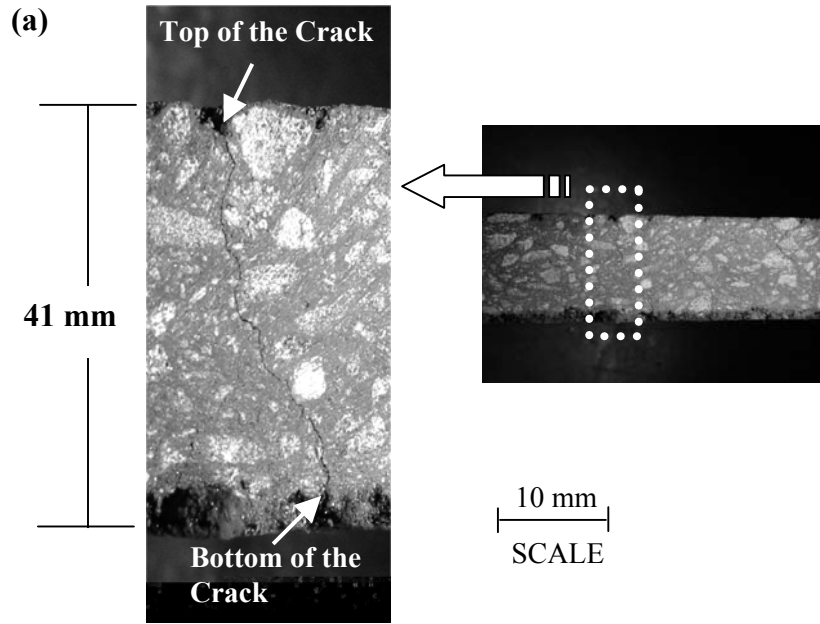


Figure 5.10 Fatigue Alligator Cracking Pattern in RI-1 Pavement:
(a) Top and Bottom Cracking Interconnection on Cross-section; and
(b) Highlighted Crack Paths at Bottom of Pavement

5.4.2 INDIRECT TENSION FATIGUE TESTS (IDFT)

Read et al. (1997) presented the development and subsequent use of the indirect tension fatigue test (IDFT) to evaluate the life to crack initiation of asphalt concrete. The horizontal deformation during the IDFT is recorded as a function of load cycle. The loading pattern used in the IDFT is a haversine load. Each specimen is subjected to a different level of stress so that a regression analysis on a range of values allows the development of the fatigue relationship (Figure 5.11) between the number of cycles at failure (N_f) and initial tensile strain (ϵ_t) on a log-log relationship:

$$N_f = k_1 * \epsilon_t^{-k_2} \quad (5.10)$$

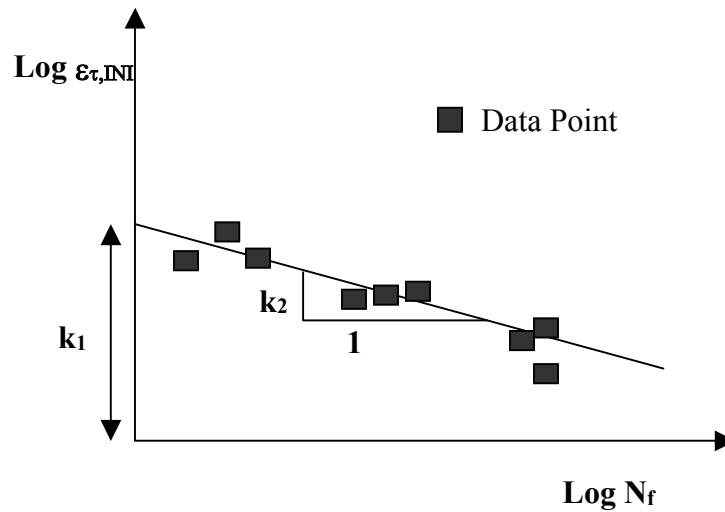


Figure 5.11 Initial Horizontal (Tensile) Strain versus Number of Load Repetitions

IDFT was conducted by Dr. Youngguk Seo in the N.C. State research group on 150 mm diameter cores taken from the RI-1 model pavement. Haversine load with the 0.6 sec loading period was used to simulate the MMLS3 loading rate. A 50.8 mm gauge length was adopted for measuring horizontal and vertical displacements. Due to 1 ~2% variation in air void contents measured at different locations, cores were sorted to have similar average air void contents in each group. The initial strain from the IDFT was defined as a horizontal strain at the 200th cycle. It is believed that 200 cycles are necessary to shake down the transient response of the specimen as well as that of the equipment. Figure 5.12 shows the fatigue life behavior at different load levels. Based on the failure criterion defined in section 5.4.1, the fatigue relationship between N_f and ε_t shown in Figure 5.13 was developed to obtain regression coefficients, k_1 (0.7857) and k_2 (1.0092). The values of fatigue service life determined at different load levels are presented in Table 5.2.

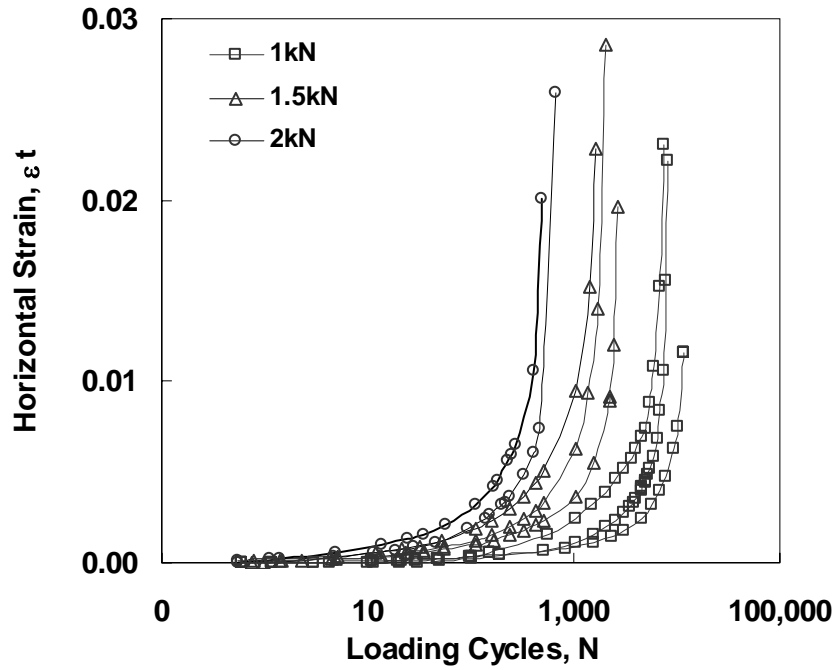


Figure 5.12 Fatigue Life Profiles Using RI-1 Mix

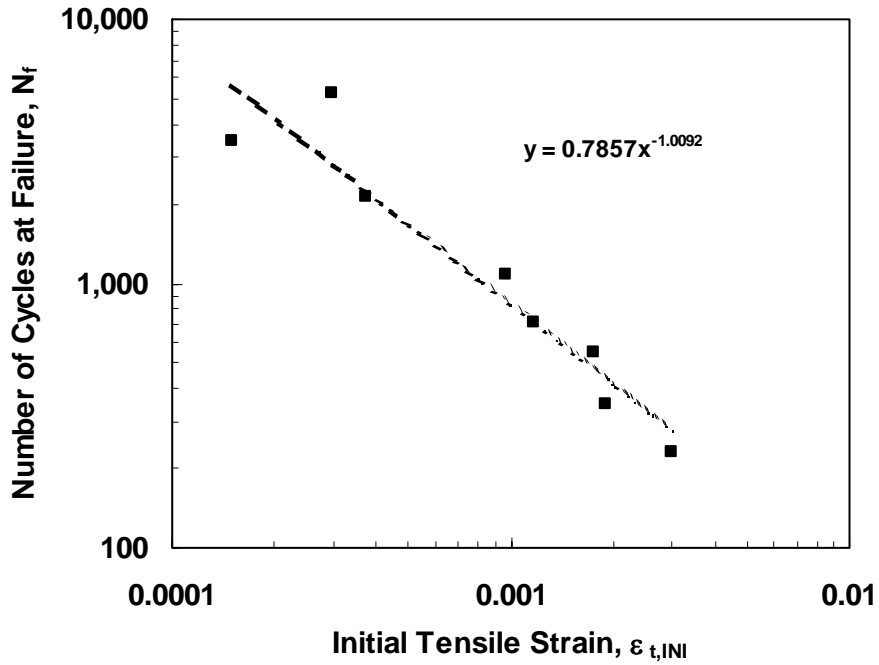


Figure 5.13 Regression Analysis for Coefficients, k_1 and k_2 , of Fatigue Life Prediction Model

Table 5.2 IDT Fatigue Testing Results

Test	Specimen ID	%AV	Load Levels (kN)	ε_t	N_f
RI-1	1	9.28	1	295	5,241
	3	10.74	1	150	3,437
	9	9.30	1	373	2,146
	4	9.51	1.5	968	1,075
	11	10.11	1.5	1,761	552
	14	8.15	1.5	1,168	710
	5	11.73	2	2,975	229
	10	10.46	2	1,917	351

5.4.3 CUMULATIVE DAMAGE ANALYSIS

Fatigue damage increases with applied loading cycles in a cumulative manner. Thus, cumulative fatigue damage analysis plays a key role in the fatigue life prediction of pavements subjected to MMLS3 loading. Miner's linear damage theory (Miner, 1945) was adopted to assess the fatigue behavior of the laboratory pavements tested. This damage model determines the incremental change in pavement wear caused by repetitions of dynamic load over time. The measure of damage (D) is the sum of the cycle ratios and assumes linear energy accumulation. That is,

$$D_i = \frac{N_i}{N_{fi}} \quad \text{and} \quad D = \sum_i D_i \quad (5.11)$$

where D_i = damage caused by the i^{th} load,

N_i = number of applied wheel applications of the i^{th} load, and

N_{fi} = allowable number of load repetitions to fatigue failure by the i^{th} load.

According to this model, failure occurs when $D = 1$.

Knowing that the MMLS3 loading incorporates a wandering mechanism, it would be of importance to correctly analyze fatigue damage. As shown in Figure 5.14, the lateral movement of a wheel provides a normal loading distribution on the pavement. Using the various load levels along the center line of the wheel path, an understanding of fatigue damage growth is possible. As a wheel moves laterally across the pavement, it makes 21 stops in 100 mm; these stops are referred to as “stations”. According to the time spent at each station in one wandering period (i.e., the time that it takes the wheel to move through each of the 21 stations), the N_i at the i^{th} station can be obtained. Then, the tensile strain value at each station was estimated using EverStress. A simplified example of this analysis is presented in Appendices B-1 and B-2.

Using the Asphalt Institute fatigue model in Eq. 5.1, the N_{fi} at the i^{th} station was determined. For the RI-1 pavement, with asphalt volume, V_b , of 5.8% and average air void volume, V_a , of 9.2%, the values of M and the correction factor, C, from Eq. 5.2 are calculated. After MMLS3 loading, specimens were obtained from the unloaded area by coring and prepared for IDT fatigue tests. Their thickness was determined to be approximately 38 mm with an average air void content of 9.2%. The tensile strain (ϵ_i) in Eq. 5.2 is the initial strain. Under the MMLS3 loading, it is assumed that it takes about 300 wheel applications, at which time the MMLS3 reaches from edge to center of the wheel path, to obtain a stabilized response from the pavement. The measured initial strain at the point in time was $297 \mu\epsilon$ under the center of the wheel path.

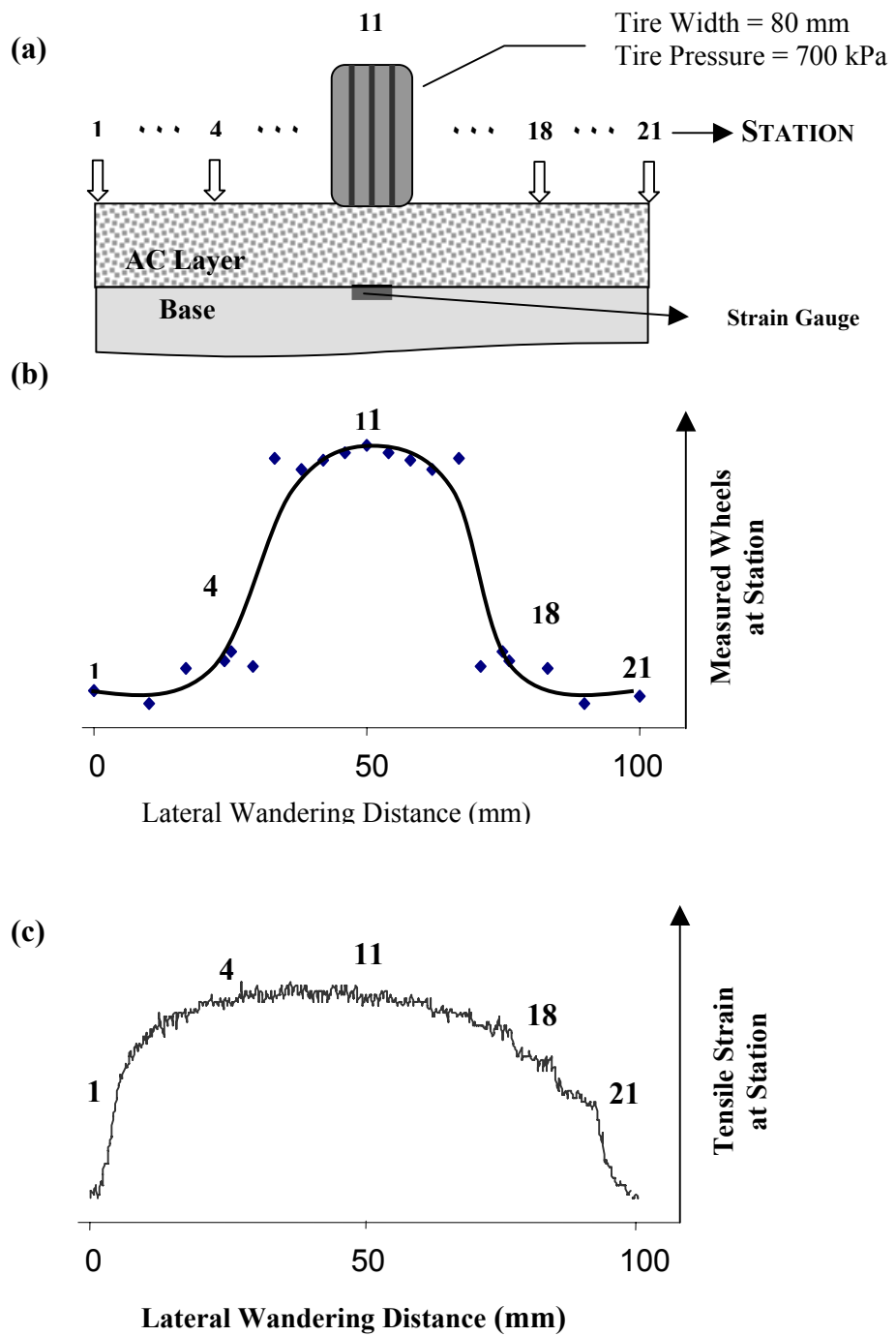


Figure 5.14 Schematics of Lateral Wheel Wandering: (a) Schematic of Loading Wheel; (b) Wheel Distributions in Wandering Period; and (c) Strain Gauge Responses at Different Wheel Locations

With the assumed Poisson's ratio of 0.31 at 20.5°C and the measured MMLS3 dynamic wheel load of 3.57 kN, the modulus of the pavement can be calculated using EverStress. This modulus corresponds to the measured initial strain in the iteration approach, it was found to be 2400 MPa. The tensile strain predicted by EverStress used an average of 10 points over a gauge length of 50 mm to allow fair comparison to the embedded strain gauge, which gave a single strain measurement over the 50 mm gauge length in the pavement. As the tensile strain values at 21 wandering stations were calculated, the prediction method stated above was applied. In accordance with the linear damage rule, the fatigue life was determined to be 23,200 cycles.

The IDT dynamic modulus test was performed as a fingerprint prior to IDT fatigue testing for IDT specimens. The dynamic modulus of specimen ID 1 (9.2% AV) at the MMLS3 testing condition was determined to be 2,585MPa. Using this modulus in EverStress, the initial tensile strain of 281 $\mu\epsilon$ was calculated and based on these strain values the RI-1 pavement's failure at 26,054 wheel applications was expected. The difference between measured and calculated pavement's failure gave the attention to get correct coefficients in modified fatigue model as follows:

$$N_f = k_1(\epsilon_t)^{-k_2} |E^*|^{k_3} \quad (5.12)$$

where,

k_1 , and k_2 = regression coefficients obtained from Eq. 5.10;

k_3 = correction factor fit to measured N_f at $D = 1$.

Now, the regression coefficients, k_1 (0.7857) and k_2 (1.0092) determined in Section 5.4.2, were substituted to AI fatigue model with dynamic modulus, 2,585 MPa, that was calculated by analysis of multi layer elastic program. Then the third coefficient,

k_3 , was found to be “0.2379” fitting to the RI-1 pavement’s failure at 70,800 wheel applications. Tables 5.3 and 5.4 show the comparative results by using different coefficients in fatigue model. This approach encourages using only IDT testing program to predict N_f of a laboratory pavement.

Table 5.3 Pavement Failure Prediction Using Measured Initial Tensile Strain (ϵ_t , 297 $\mu\epsilon$)

Calculated Dynamic Modulus ($ E^* $, MPa)	AI Fatigue Model			Regression Analysis of IDT Fatigue Test		Variable	Model Predicted N_f (N_{fM})	Experiment Predicted N_f (N_{fE})
	$c \cdot f_1$	f_2	f_3	k_1	k_2			
2400	0.0029	3.2910	-0.854				32,909	70,800
				0.7857	1.0092	-0.2436	70,800	

Note: For AI fatigue model, correction factor (c) of 0.0463 times to k_1 (0.0636)
 Model Predicted $N_{fM} = N_f$ determined by AI fatigue model
 Experiment Predicted $N_{fE} = N_f$ determined using IDT fatigue

Table 5.4 Pavement Failure Prediction Using Measured Dynamic Modulus ($|E^*|$, 2585 MPa)

Calculated Strain (ϵ_t , $\mu\epsilon$)	A.I. Fatigue Model			Regression Analysis of IDT Fatigue Test		Variable	Model Predicted N_f (N_{fM})	Experiment Predicted N_f (N_{fE})
	$c \cdot f_1$	f_2	f_3	k_1	k_2			
281	0.0029	3.2910	-0.854				32,909	70,800
				0.7857	1.0092	-0.2379	70,800	

5.4.4 FATIGUE LIFE PREDICTION ALGORITHM USING IDT TESTING PROGRAM

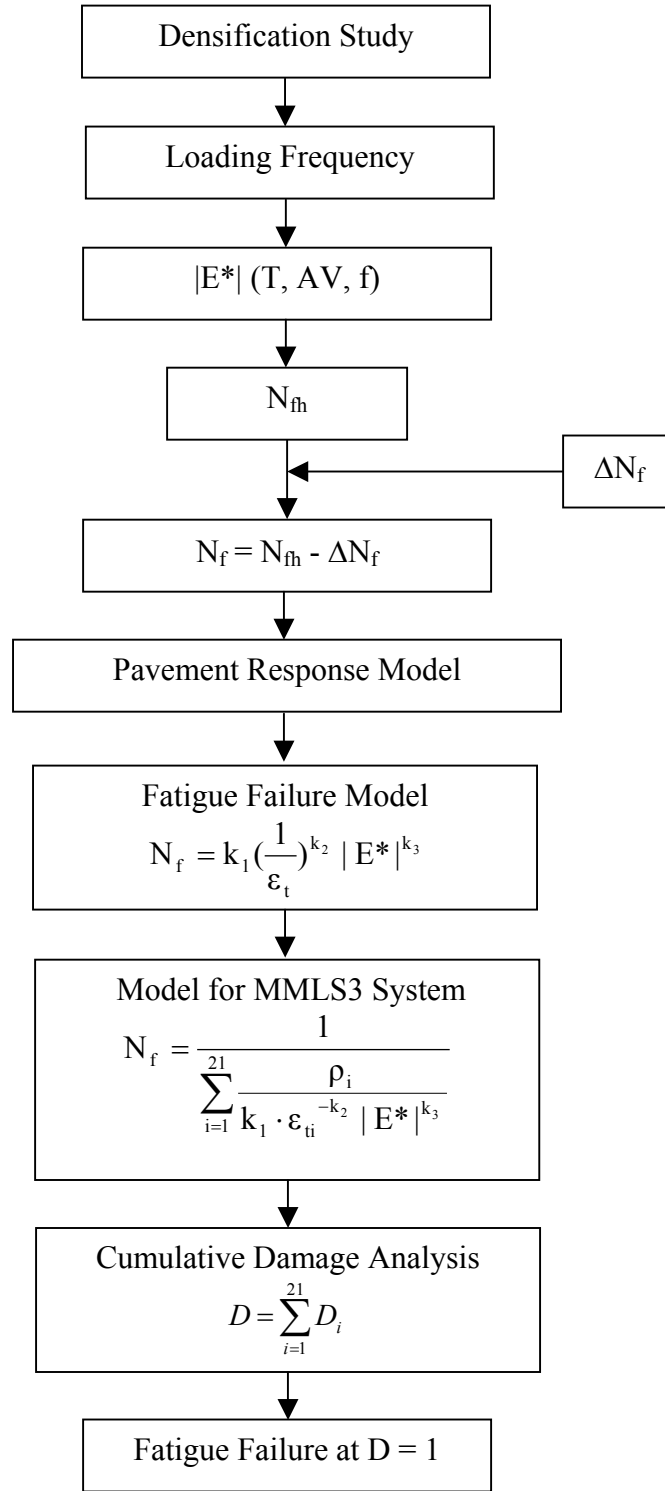


Figure 5.15 Framework for Prediction of Fatigue Failure

Definitions:

- T: Temperature
- AV: Air void content in percentage
- f: Loading frequency
- $|E^*|$: Dynamic modulus
- N_{fh} : Number of wheel applications at fatigue failure including rest period (healing effect)
- ΔN_f : Number of wheel applications for healing periods
- N_f : Number of wheel applications at fatigue failure excluding healing effect
- k_1 & k_2 : Fatigue regression coefficients based on air void content of the IDT specimen
- ϵ_t : Tensile strain on the center at the bottom of the MMLS pavement
- D: Damage ratio
- i : i^{th} loading stop among 21 stations in wandering period
- k_3 : The coefficient in fatigue prediction model based on fatigue failure of the MMLS3 pavement

In contrast to Section 5.4.3, methodology for the service life prediction of laboratory pavement fatigued by the MMLS3 is proposed using an IDT testing program that is based on specimens fabricated by gyratory compaction. It is expected that this alliance between the accelerated pavement test and small laboratory test can be a cornerstone to successfully estimate the service life of in situ pavements in the future.

To establish the fatigue failure prediction algorithm, the following procedure was considered as shown in Figure 5.15:

1. According to the air void content reduction study, a decrease of 2% in air void content is expected throughout the MMLS3 fatigue testing. For example, the fatigue service life for an 8.9% air void section of the MMLS3 pavement is predicted using k_1 & k_2 from IDT testing results for a specimen with 6.9% air voids. A careful look was given to examine the fundamental difference in both testing conditions. As discussed in Section 5.4.1, it was observed that even using a wandering system, the surface layer in laboratory pavement would be subjected to densification. Thus, air void densification study on field cores was conducted to refine the target air voids for specimens that are ready in laboratory (NC DOT report, 2002). The observation was made that air void differences between wheel path and lane center are dependent on the initial air void content. As the overall trend indicates in Figure 5.16, a significant air void reduction develops during the first two-year period. After that period, the densification process has slowed and air void content stabilizes. In this regard, target air voids of specimens for fatigue testing could be selected based on final air void contents achieved after two years

of densification. Considering some assumptions and adjustments, specimens with three air void contents of 6.0, 6.8, and 8.2% for I19C-A mix were fabricated.

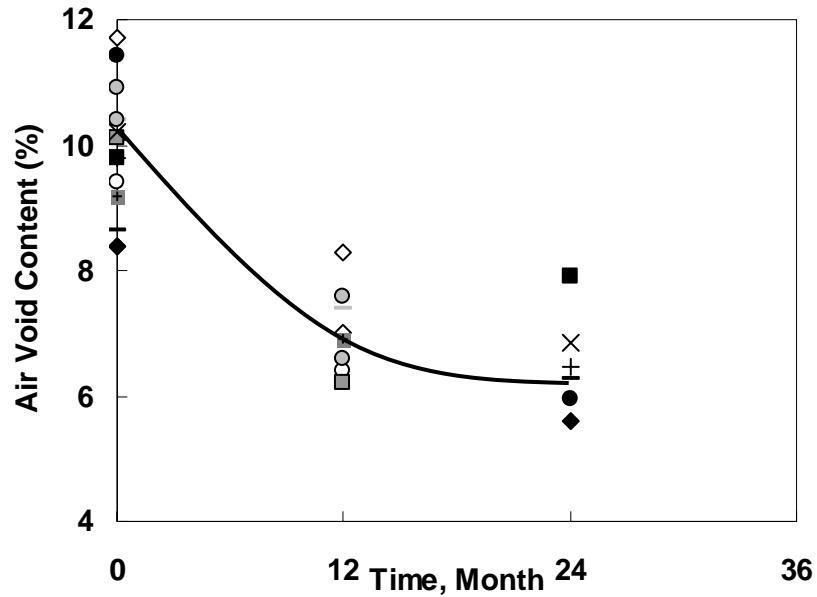


Figure 5.16 Reduction of Air Void Contents Using Field Cores
(NC DOT Report, 2002)

2. The response of deformation in asphalt concrete shows delayed behavior from the applied loading time due to the time dependent behavior of viscoelastic materials (Barkdale (1971), Kim (1994)). The loading time of 0.3 sec on the pavement surface and tensile strain pulse time of 0.6 sec at 45 mm deep in asphalt concrete layer were measured. According to Kim (1994), the longitudinal tensile strain pulse time and the depth beneath pavement surface have the linear relationship. On this account, the loading frequency at mid-depth for this algorithm is determined using the following linear equation in Figure 5.17:

$$\begin{aligned} \text{Loading frequency} &= -0.037 \times \text{mid-depth (22.5 mm)} + 3.33 \quad (5.13) \\ &= 2.5 \text{ (Hz)} \end{aligned}$$

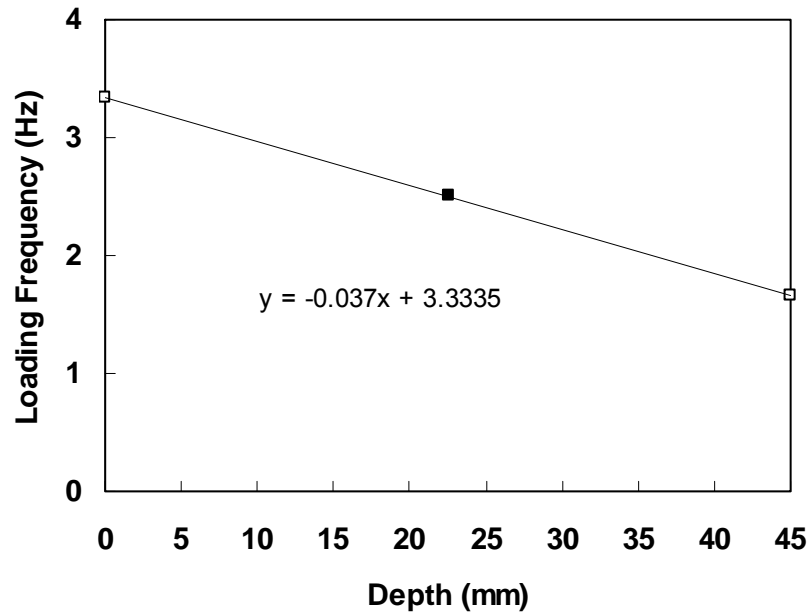


Figure 5.17 Loading Frequency Variation along Depths

- Through the uniaxial testing program, frequency sweep tests conducted within linear viscoelastic limits at different frequencies and temperatures should yield a single continuous mastercurve for dynamic modulus. Since shift factors as a function of temperature are found, the dynamic modulus as a function of temperature and air void content is determined as shown in Table 5.5.

Table 5.5 Uniaxial Dynamic Modulus at 20°C

Air Void Content (%)	Dynamic Modulus ($ E^* $, MPa)
8.9	4473.71
9.8	4024.75
10.4	3749.86
11.1	3451.94

4. Fatigue failure is measured through the MMLS3 test, which is defined in the overall tensile strain profile. However, it is noticeable that rest periods during the measurements of stress wave and surface survey in MMLS3 testing may influence to extend fatigue service life (ΔN_f) as discussed in Section 4.5.3. Therefore, N_f determined from strain profile analysis should be corrected by shifting to exclude rest period effect. At this point, overall strain profiles are investigated. Graphical interpretations are available in Figure 5.18 showing the correction method of the wheel applications that are effected by healing. In addition, Table 5.6 represents the computation of N_f as mentioned above. In general, the amount of healing decreases as the damage increased. This trend is expected because macrocracks cannot heal as efficiently as microcracks can.

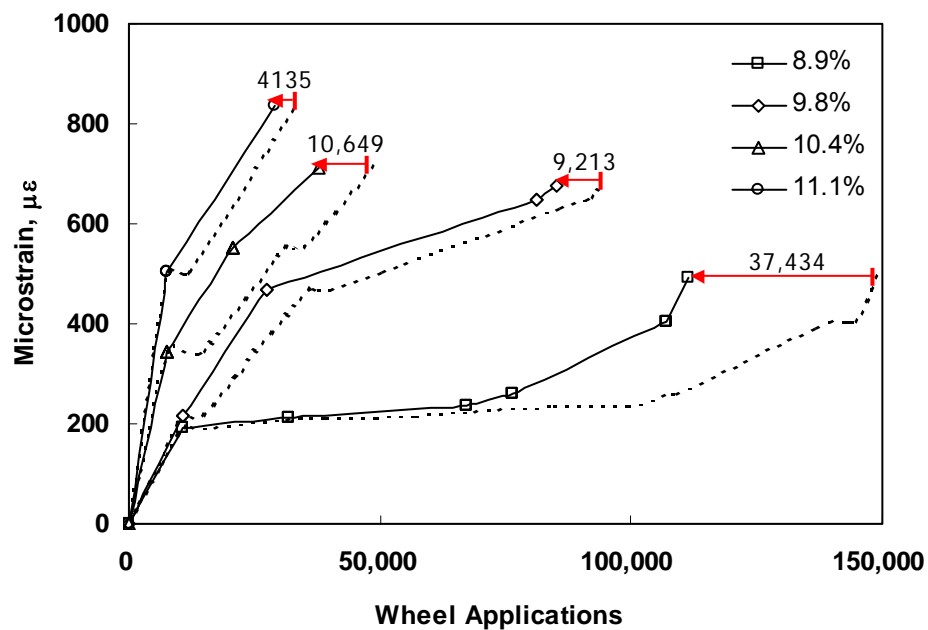


Figure 5.18 Correction of N_{fh} by Excluding Healing Effect

Table 5.6 Determination of N_f Based on Tensile Strain Profiles

Air Void (%)	Wheel Applications Before Healing	Wheel Applications After Healing	Difference	Sum of Difference (ΔN_f)	N_{fh}	N_f
8.9	10,750	14,550	3,800	37,434	148,966	111,532
	35,750	49,030	13,280			
	84,500	98,880	14,380			
	107,750	109,207	1,457			
	139,750	144,267	4,517			
9.8	10,750	14,577	3,827	9,213	94,170	84,957
	35,900	40,373	4,473			
	90,250	91,163	913			
10.4	7,650	14,813	7,163	10,649	48,346	37,697
	31,150	34,636	3,486			
11.1	7,650	11,785	4,135	4,135	33,007	28,872

5. The regression coefficients, k_1 and k_2 , as a function of air void content for IDT specimens, can be found for the fatigue model given in Eq. 5.10. As explained in Section 5.4.2, indirect tension fatigue tests performed to develop the fatigue relationship at three air void contents between the number of cycles at failure and initial tensile strain on a log-log model relationship (Figure 5.19 (a)). These regression coefficients are obtained from the plots versus air void contents in Figure 5.19 (b). Table 5.7 shows the determined values of regression coefficients as a function of air void content for the algorithm. While the tensile strain increases with air void contents, k_1 increases but k_2 decreases, though.

Table 5.7 Regression Coefficients, k_1 and k_2 , Determination for IDT specimen
Using I19-C-A Mixtures

$k_1 = a_1(\%AV)^{b_2}$		$k_2 = a_2(\%AV)^{b_2}$		Air Void Content (%)			
a_1	b_2	a_2	b_2	6.9	7.8	8.4	9.1
8.64E-17	18.31	34.714	-1.653	k_1 0.198	1.866	7.246	31.376
				k_2 1.426	1.164	1.030	0.902

6. Using the uniaxial dynamic modulus ($|E^*|$), multi-layer elastic analysis by EverStress 5.0 program is conducted to find the tensile strain (ϵ_i) in the center of wheelpath at the bottom of the pavement for the MMLS3 wandering system (Step 2) at 20°C. As mentioned in Section 5.4.3, the measure of damage, that is damage ratio (D), is the sum of the cycle ratios in the assumption of linear energy accumulation. Thus, cumulative damage analysis at 21 wandering stations, as described in Section 5.4.3, is performed. The Asphalt Institute fatigue model in Eq. 5.1 is used to determine the fatigue failure in the MMLS3 system including 21 wheel loading stations. Based on cumulative damage analysis (Appendix C.1), the fatigue failure model is developed as follows:

$$N_f = \frac{1}{\sum_{i=1}^{21} \frac{\rho_i}{C \cdot f_1 \cdot \epsilon_{ti}^{-f_2} |E^*|^{f_3}}} \quad (5.14)$$

where,

N_f = Wheel applications at failure based on Asphalt Institute model

ρ_i = Fraction at i^{th} station of wheel load at in one wandering period

C = Correction factor as a function of air void content

$f_1, f_2,$ and f_3 = Regression coefficients

ϵ_{ti} = Tensile strain at i^{th} station of wheel load

$|E^*|$ = Dynamic modulus

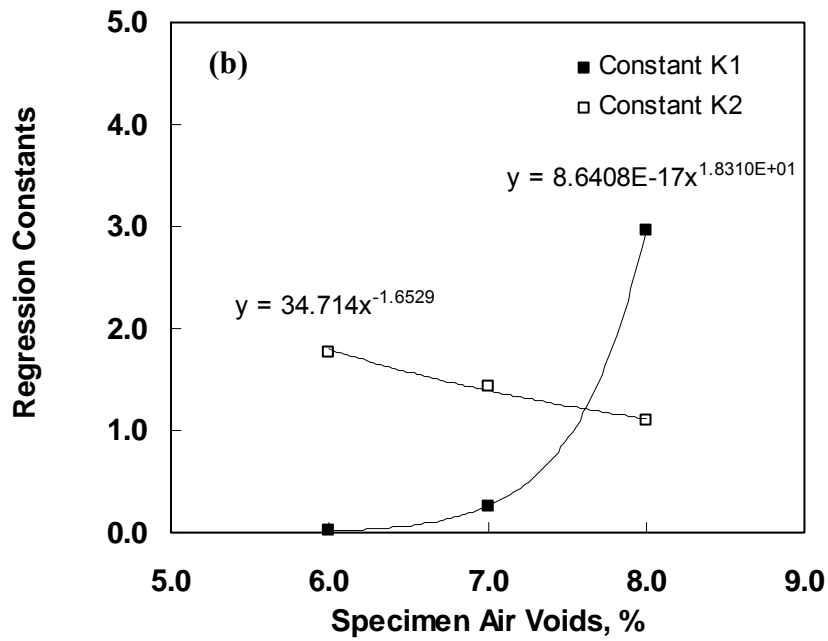
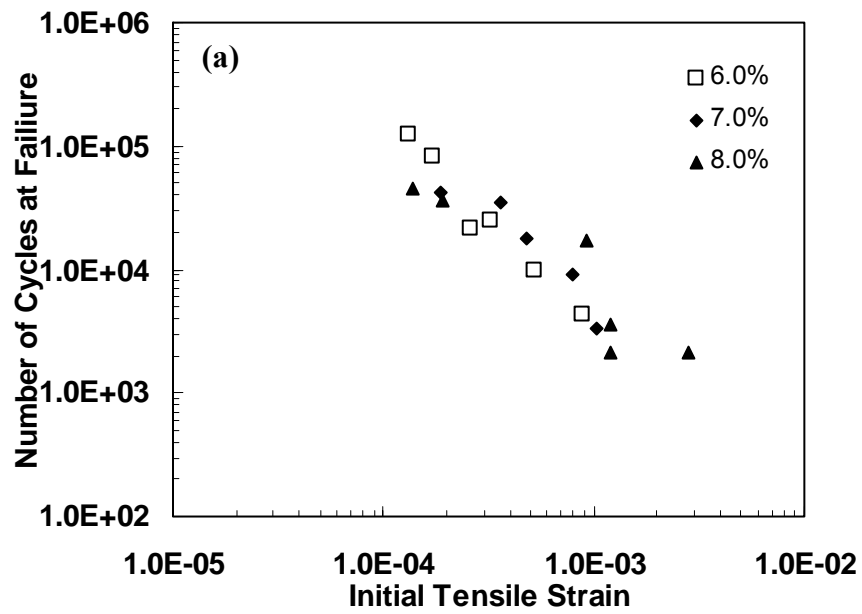


Figure 5.19 Regression Analysis for k_1 and k_2 in Fatigue Model:

- (a) Initial Tensile Strain versus Number of Cycles;
- (b) k_1 and k_2 as a Function of Air Void Contents

Table 5.8 includes the summary of cumulative damage analysis in this research.

Detailed mathematical explanations are available in Appendix C.2.

Table 5.8 Summary of Cumulative Damage Analysis Using Eq. 5.14

Air Void (%)	8.9	9.8	10.4	11.1
Correction Factor (C)	0.03716	0.0288	0.0247	0.0210
f_1	0.0636			
f_2	3.291			
f_3	-0.854			
N_f	111,532	85,957	37,697	28,872
Predicted N_f	68,472	38,821	30,741	21,773
Damage Ratio (D)	1.63	1.87	1.05	1.06

7. According to the proposed fatigue service life prediction algorithm for the MMLS3 pavement using only an IDT testing program, k_3 , which is the last leftover variable in Eq. 5.12, can be found by the condition as follows:

$$N_f \text{ (in algorithm)} = N_f \text{ (in Asphalt Institute model)} \quad (5.17)$$

$$\frac{1}{\sum_{i=1}^{21} \frac{\rho_i}{k_1 \cdot \varepsilon_{ti}^{-k_2} |E^*|^{k_3}}} = \frac{1}{\sum_{i=1}^{21} \frac{\rho_i}{C \cdot f_1 \cdot \varepsilon_{ti}^{-f_2} |E^*|^{f_3}}} \quad (5.18)$$

$$k_3 = \frac{1}{\log |E^*|} \left[\log(C) + \log\left(\frac{f_1}{k_1}\right) + \log\left(\frac{\sum_{i=1}^{21} \frac{f_i}{\varepsilon_{ti}^{-k_2}}}{\sum_{i=1}^{21} \frac{f_i}{\varepsilon_{ti}^{-f_2}}}\right) \right] + f_3 \quad (5.19)$$

Mathematical process from Eq. 5.17 to Eq. 5.19 is explained in Appendix C.3.

By the use of Eq. 5.19, Figure 5.20 was developed for determining k_3 (Table 5.9) as a function of air void content to perform the MMLS3 fatigue life prediction, which can be expressed as:

$$k_3 = 0.0217e^{0.1646x} - 0.1 \quad (5.20)$$

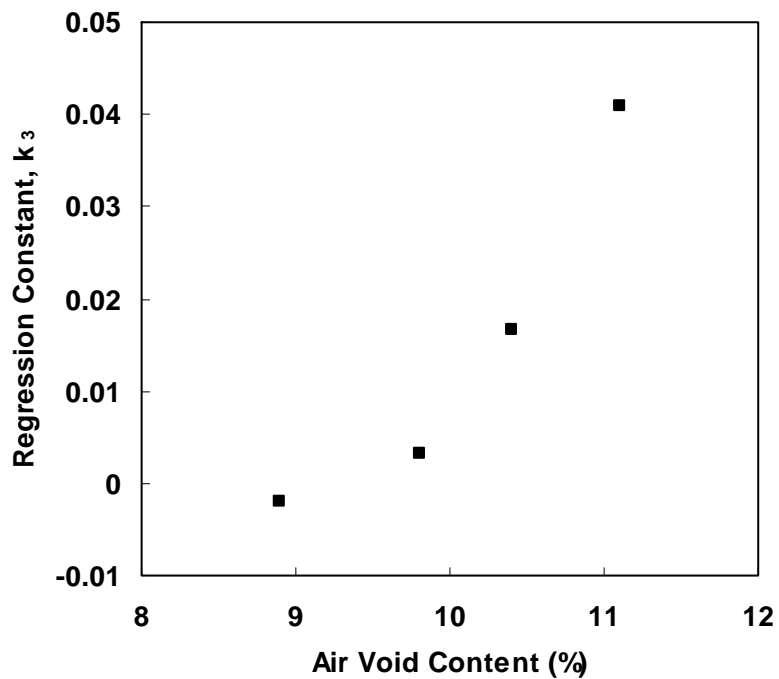


Figure 5.20 Determination of k_3 as a Function of Air Void Content

Table 5.9 Values of k_3 for the Fatigue Model

Air Void (%)	8.9	9.8	10.4	11.1
k_3	-0.00196	0.00312	0.01661	0.04099

It is concluded that the use of the developed algorithm can determine the fatigue failure of the MMLS3 pavement using an IDT testing program based on laboratory-fabricated specimens. As for the sections with 8.9 to 11.1% air void contents of I19C-A pavement, this algorithm conducted the prediction in failure criterion with the damage ratios of 1.05 ~ 1.87 using regression coefficients, which were developed using IDT specimens with 6.0% to 8.2% in air void contents.

5.5 SUMMARY

Fatigue phenomenon on model pavements was studied using the MMLS3. After efforts were given to correctly construct slabs for fatigue tests, the MMLS3 pavement structure was determined and appropriate instruments were selected. Fatigue failure, evidenced by alligator crack patterns was observed on the laboratory pavement. Failure prediction was performed by damage analysis using measured tensile strain profiles and stress wave analysis. The results from an IDT testing program were then employed to predict the fatigue performance for the MMLS3 testing.

CHAPTER 6

RUTTING PERFORMANCE INVESTIGATION

6.1 INTRODUCTION

Accelerated pavement testing using the MMLS3 allows a rapid assessment of the rutting potential of different asphalt mixtures under controlled conditions. Rutting is the load-induced permanent deformation of a flexible pavement and reduces the practical service life of the pavement. Depending on the magnitude of the load and relative strength of the pavement layers, permanent deformation can occur in the subgrade, base, or HMA layers. In recent years, the amount and severity of rutting in asphalt pavements have increased due to the increase in truck tire pressure, axle load, and traffic volume.

As previously described in the research objectives, one of the motivations for this research was to approximately investigate the effect of temperature and density on the long-term rutting performance in the asphalt surface layer. The slabs for asphalt-aggregate mix were constructed in divided sections as described in Section 6.3 and were tested at 40°C, a critical temperature in North Carolina, and 55°C, assumed as an extreme condition. While the MMLS3 wheels were passed without wandering over each slab listed in Table 3.2, the rut depth was regularly measured by a profilometer and an electronic indicator. This chapter presents results of tests at 40°C and 55°C. The deformation data were analyzed to determine whether the pavement performance could be quantified in terms of density or excess air void. The primary factors considered in this comparative rutting study are as follows:

- Constantly controlled temperature;
- Air void contents; and
- Aging procedure for mixture preparation.

In addition to monitoring performance of the pavement sections during the MMLS3 testing, the temperature distribution as a function of depth within the AC layer was measured. These temperature data were analyzed to develop an algorithm to realistically predict rut depth (i.e., permanent deformation) development under the MMLS3 using data from laboratory triaxial testing. Regression constants and material properties, such as resilient strain and dynamic modulus, were obtained from triaxial testing. Finally, the rutting performance for different densities of AC layer was predicted/verified using the proposed algorithm.

6.2 PERMANENT DEFORMATION EMPIRICAL MODEL

The empirical linear log relationship between permanent strain (ϵ_p) and number of load applications (N) is the most well known model. It can be mathematically expressed as:

$$\epsilon_p = aN^b \quad (6.1)$$

where,

- ϵ_p = cumulative permanent strain
- a = intercept from regression
- b = slope from regression
- N = number of loading repetitions

To obtain the permanent strain (ϵ_{pn}) resulting from a single load application, differentiation of Eq. (6.1) will yield the following equation (QI et al, 1993):

$$\frac{\varepsilon_{pn}}{\varepsilon_{RP}} = \frac{ab}{\varepsilon_{RM}} N^{b-1} \quad (6.2)$$

where,

a and b = regression constants

ε_{pn} = permanent strain change at N^{th} loading

ε_p = cumulative permanent strain

ε_{RM} = measured resilient strain

ε_{RP} = predicted resilient strain

N = number of loading repetitions

It is obvious that the two coefficients, a and b , used in the prediction model represent a material's permanent deformation characteristics under a given magnitude of repeated loads. These two constants can be obtained by linear regression techniques in logarithmic space. The intercept coefficient, a , denotes the permanent strain at $N = 1$ repetition, whereas, the slope coefficient, b , denotes the rate of change in permanent strain with respect to load repetitions, in logarithmic form.

6.3 RUTTING SLAB CONSTRUCTION DEVELOPMENT

Based upon the experience of slab construction for fatigue testing, laboratory pavements for the rutting long-term performance test were built on the 25-mm steel plate supported on compacted sand. Each slab with different material characteristics, such as density and aggregate distribution, was compacted with constant compaction effort in two 60 mm asphalt lifts. A tack coat using MC-30 was used to ensure a bond between the first and second lifts. As before, the slabs were formed in divided sections and then tested at

the desired temperature. The layout and configuration used for the MMLS3 testing of slabs were explicitly explained in Chapter 3.

6.4 EVALUATION OF RUTTING PERFORMANCE

6.4.1 PAVEMENT TEMPERATURE CONTROL

An “effective temperature” for permanent deformation can be defined as a single test temperature at which the amount of permanent deformation accumulated caused by a given number of wheel load applications would be equivalent to that caused by the same number of loads applied at different temperatures representing the seasonal variation of temperature throughout the year. From temperature data obtained from the National Climate Data Center for the eight divisions of the State of North Carolina, the effective temperatures range between 31°C and 46°C (NC DOT report, 2002). Thus, the temperature selected for permanent deformation testing was 40°C. Testing was also performed at 55°C to represent extreme conditions.

Changes of temperature within the pavement were monitored using K-type thermocouples throughout the MMLS3 testing. Temperatures at three depths (top 0 to 10 mm, middle 60 mm, and bottom 110 to 120 mm) within the test pavement (RI-1) were measured, together with the cumulative load applications. Figure 6.1 shows that the temperature of the asphalt concrete remained fairly constant throughout the test. For the 40°C test (Figure 6.1 (a)), average overall temperature in the mid-depth of the pavement was 40.2°C, whereas the mid-depth temperature of the pavement targeted to 55°C was 52.4°C (Figure 6.1 (b)). From each of these figures, it can be seen that the top and bottom temperatures were approximately plus and minus 5 degrees different than the pavement

mid-depth temperature. This variation of temperature as a function of depth will be input into the rut depth prediction algorithm.

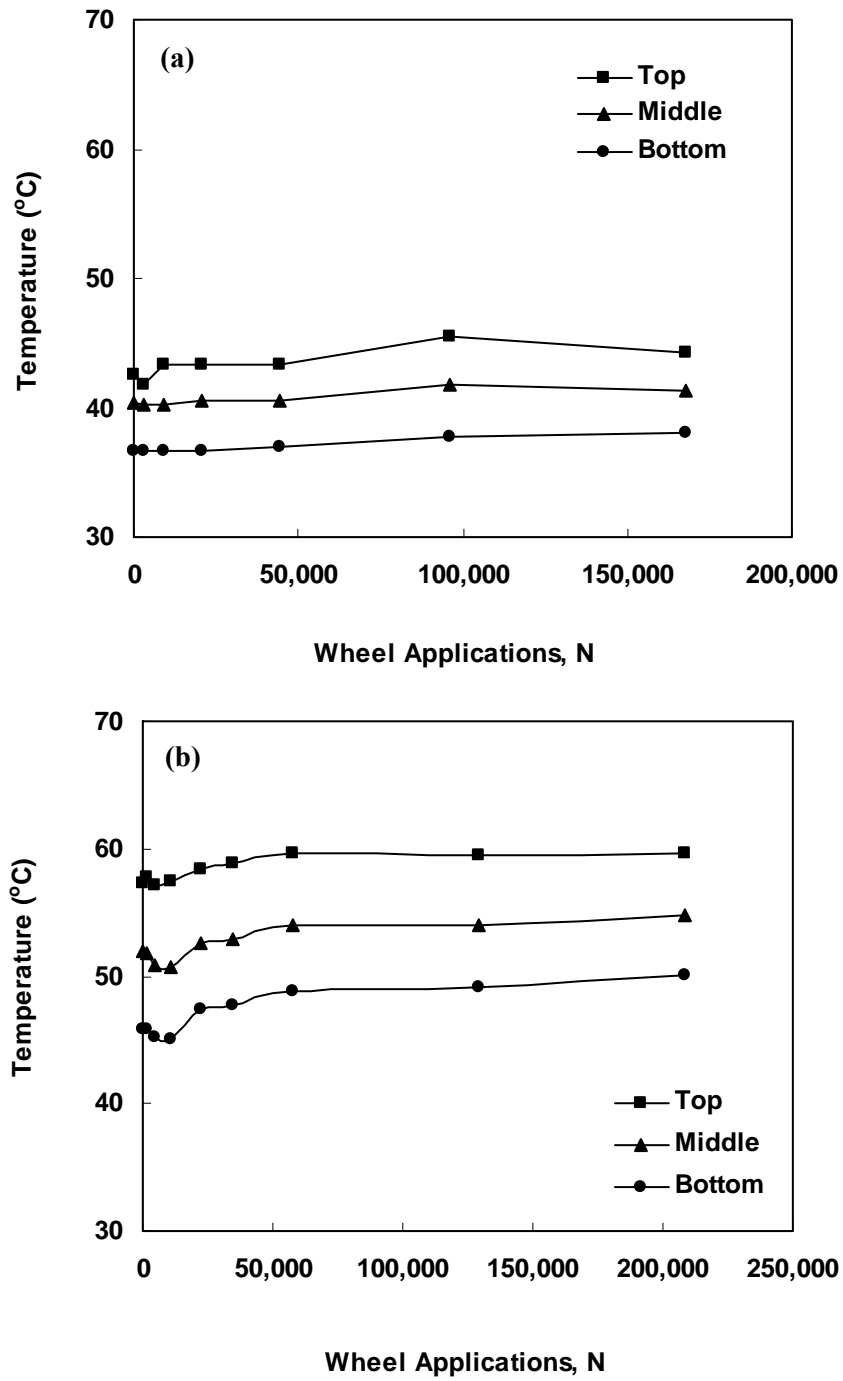


Figure 6.1 Temperature Profile in RI-1 Pavement: (a) at 40°C and (b) at 55°C

6.4.2 ANALYSIS OF RUTTING PROFILES

Using the reference test grid previously described in Section 3.3.2, transverse surface profile measurements were taken along the test grid using the profilometer. When a load is applied, the maximum deformation occurs directly under the center of the load contact area. In determining rut depth, the reference method of analysis was primarily used (Epps, 2001). By this method, the initial profile before trafficking and the subsequent profiles after a specific amount of trafficking were recorded and compared to obtain the maximum difference between two profiles in the trafficked region. Figure 6.2 presents progressive surface deformation at different number of load applications for the RI-1 slabs. Based on the reference method for the MMLS3, maximum rut depth was determined at each loading stage. For each of the two test temperatures, Figure 6.3 shows rut depth development as a function of number of load applications.

It is crucial that instrumentation be used that was capable of measuring displacements in each of the two lifts. A multi-depth deflectometer (MDD) was used to measure the permanent deformation at the top of the bottom lift. Thus, the displacement from the accumulated permanent deformation measured on each of the slab surfaces enables the contribution of each lift to the total rut depth to be determined. Figures 6.4 and 6.5 show the growth of the permanent deformation measured on the slab surfaces and the permanent deformation attributable to each of the two lifts for the RI-2 slabs at 40 and 55°C, respectively.

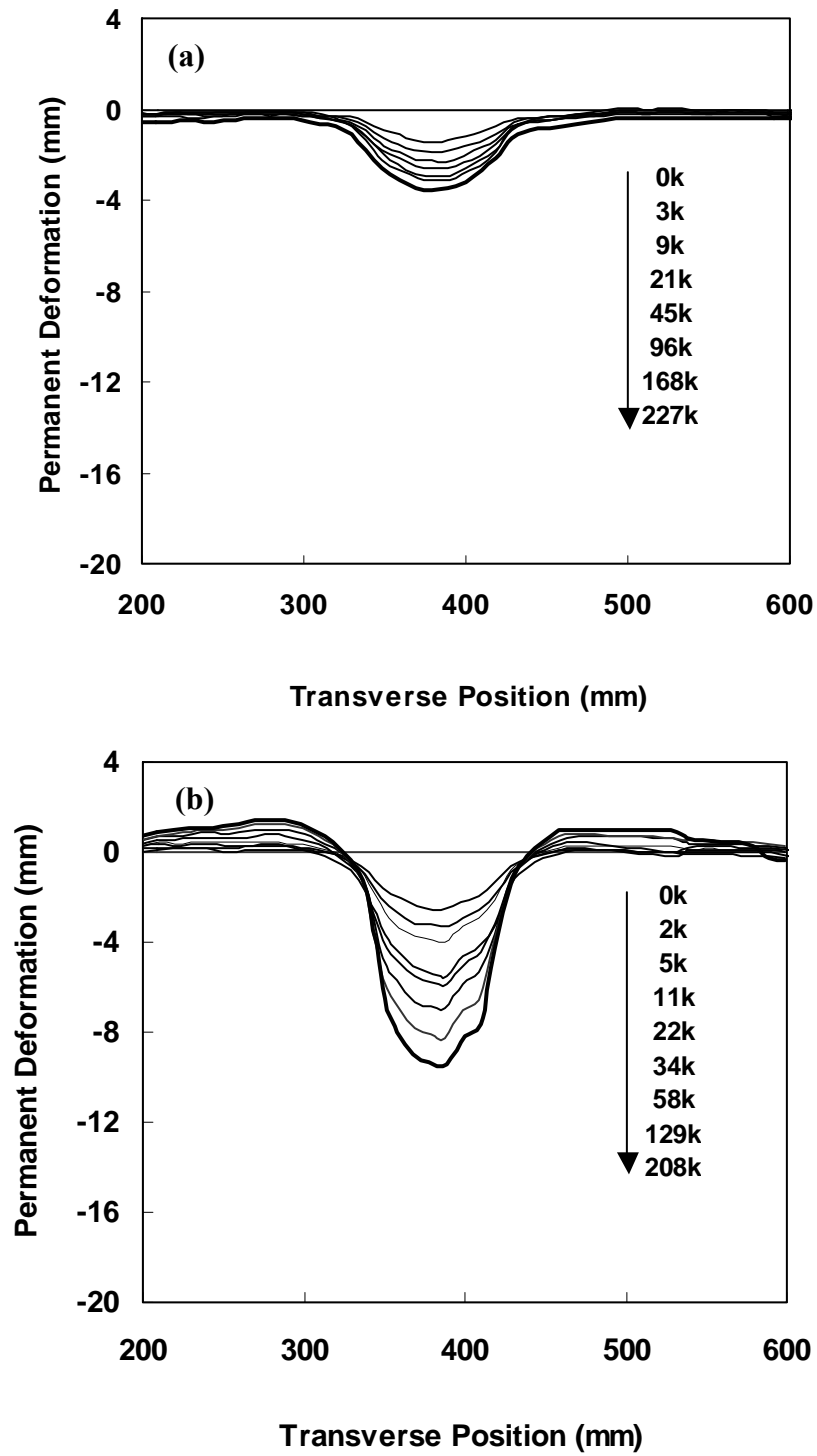


Figure 6.2 Lateral Rutting Profile for RI-1 Slab: (a) at 40°C and (b) at 55°C

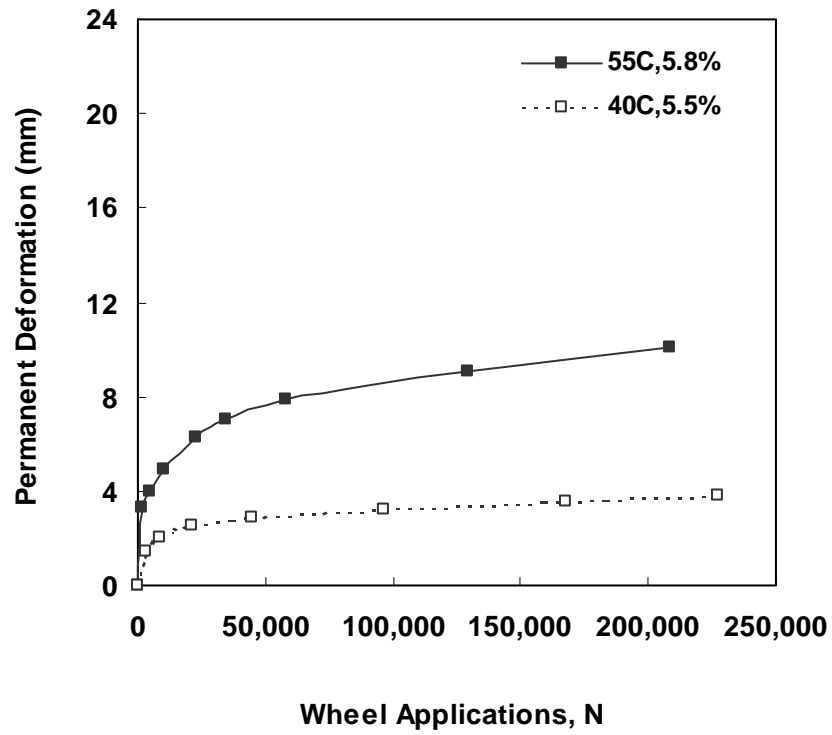


Figure 6.3 Rut Depth Growth Using Reference Method for RI-1 Slab

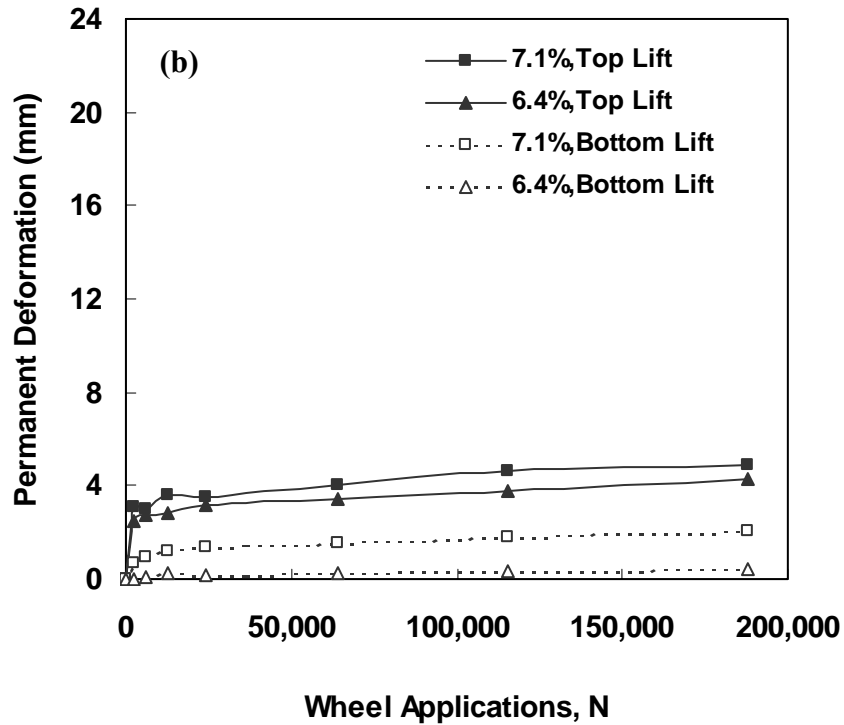
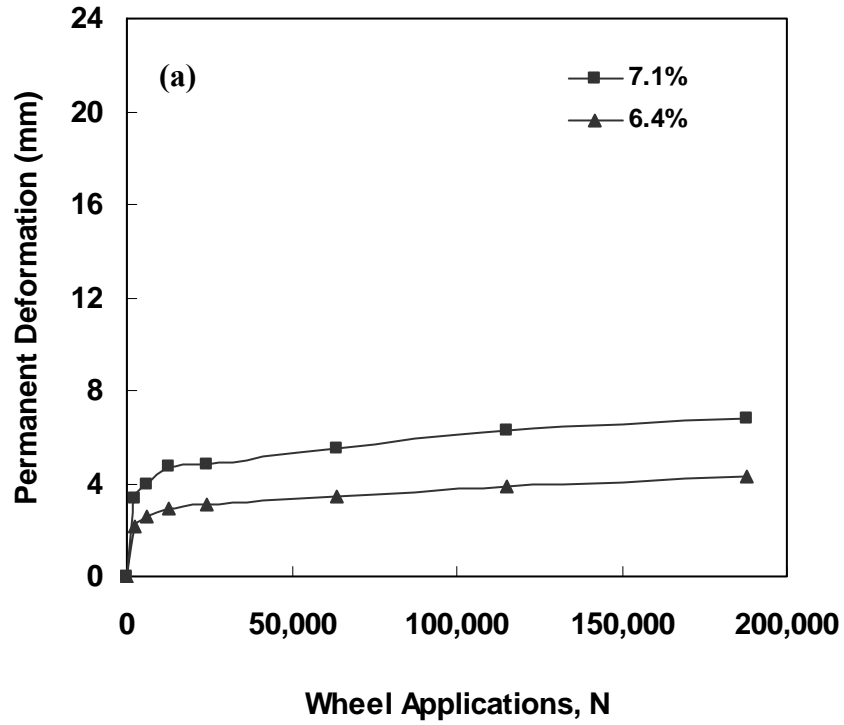


Figure 6.4 Rut Depth Growth for RI-2 Slab at 40°C:

- (a) Permanent Deformation Measured from the Pavement Surface, and
- (b) Permanent Deformation Measured from Top/Bottom Lifts

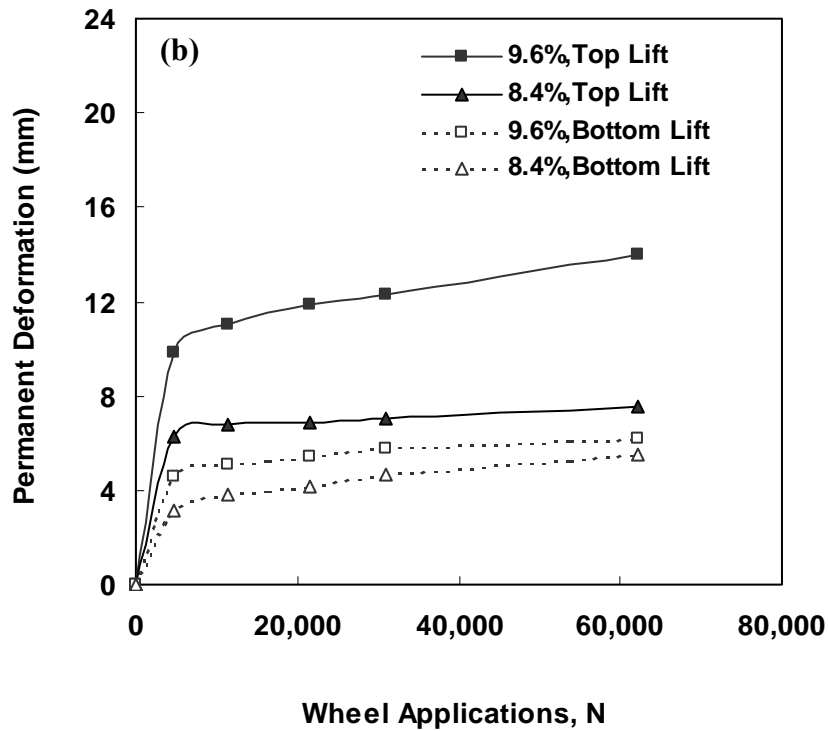
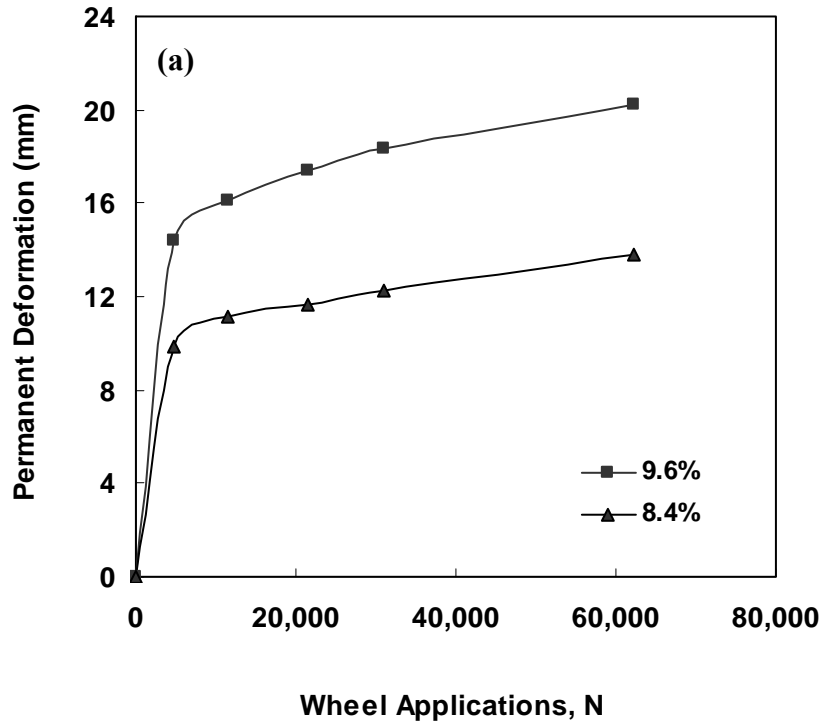


Figure 6.5 Rut Depth Growth for RI-2 Slab at 55°C:

- (a) Permanent Deformation Measured from the Pavement Surface, and
- (b) Permanent Deformation Measured from Top/Bottom Lifts

Table 6.1 presents an analysis of the deformation data with the total, top, and lower lift displacement and percentage of total deformation that occurred within the top lift. It can be observed that the permanent deformation from the top lift accounted for approximately 82% and 67% of the total rut depth measured at 40°C and 55°C, respectively.

Table 6.1 Analysis of Permanent Deformation for RI-1 and RI-2 Pavements

Temp. (°C)	Test	Air Void Content (%)	Wheel Loads (x1000)	Total PD ^a (mm)	Top Lift PD ^a (mm)	Low Lift PD ^a (mm)	% of Total PD ^a in Top Lift
40	RI-1	5.5	50	2.86	2.05	0.80	71.7
			100	3.29	2.28	1.01	69.3
			150	3.42	2.80	1.09	81.9
	RI-2	6.4	50	3.35	3.31	0.26	98.8
			100	3.73	3.69	0.36	98.9
			150	4.05	4.01	0.41	99.0
55	RI-1	7.1	50	5.24	3.86	1.38	73.7
			100	6.04	4.56	1.48	75.4
			150	6.53	4.77	1.76	73.0
	RI-2	8.4	20	5.90	4.63	1.89	78.5
			40	7.04	5.31	2.44	75.4
			60	7.82	5.71	2.66	73.0
RI-2	9.6	20	11.61	6.89	4.10	59.3	
		40	12.69	7.20	4.91	56.7	
		60	13.65	7.49	5.43	54.9	
RI-2	9.6	20	17.20	11.78	5.37	68.5	
		40	18.86	12.81	5.91	67.9	
		60	20.07	13.89	6.16	69.2	

Note: a. PD stands for permanent deformation

b. Some values between measurement intervals were determined by piecewise linear iteration method. Thus, total PD may not be equal to summation of PD's from each lift.

Parametric Study for Temperature and Air Void Effects

Changes in air temperature have the effect of changing the viscosity of the asphalt layer. Since the AC permanent deformation prediction model (Eq. 6.1) was based on repeated load compression tests, factors experimentally determined from the model may be expected to be a function of temperature and air void content. For higher temperature and/or higher air void content, decreased AC stiffness may produce a trend for variations in model coefficients. According to a comprehensive permanent deformation study by Leahy and Witzak (1991), the slope coefficient, b , was shown to be moderately influenced by temperature and air void content. The intercept coefficient, a , however, was significantly influenced by temperature and moderately influenced by compaction/air void content. To see the measured effects of testing conditions on permanent deformation using Eq. 6.1, average permanent strain was calculated as the ratio of rut depth to overall slab thickness.

Figure 6.6 shows the average permanent strain as a function of load applications for the RI-1 slabs at 40°C and 55°C. The regression curves fitting to the log permanent strain (ϵ_p) – log load repetitions (N) phenomenological relationship can be found as follows:

- At 40°C, $\epsilon_p = 0.0022 (N)^{0.2111}$
- At 55°C, $\epsilon_p = 0.0041 (N)^{0.2429}$

As depicted in Figure 6.7, the air void content effect on permanent deformation was investigated using an I19C slab that was composed of sections with air void contents of 8.7%, 8.9%, 9.7%, and 10.2%. Regression analysis of these data produced the following

functional relationship between air void content and average permanent strain as a function of number of load applications:

- 8.7%: $\epsilon_p = 0.0034 (N)^{0.2097}$
- 8.9%: $\epsilon_p = 0.0035 (N)^{0.2071}$
- 9.7%: $\epsilon_p = 0.0039 (N)^{0.2209}$
- 10.2%: $\epsilon_p = 0.0028 (N)^{0.2567}$

These results confirm that “a” and “b” were affected by test conditions and mixture properties. For the data base considered, the “a” term increased by 86% from 0.0022 to 0.0041 as the temperature was raised from 40°C to 55°C but the “b” term increased by only 15%. Figure 6.8 shows that the “a” term does not show considerable variation with air void content, however, the “b” increases approximately 22% as the air void content increases from 8.7% to 10.2%.

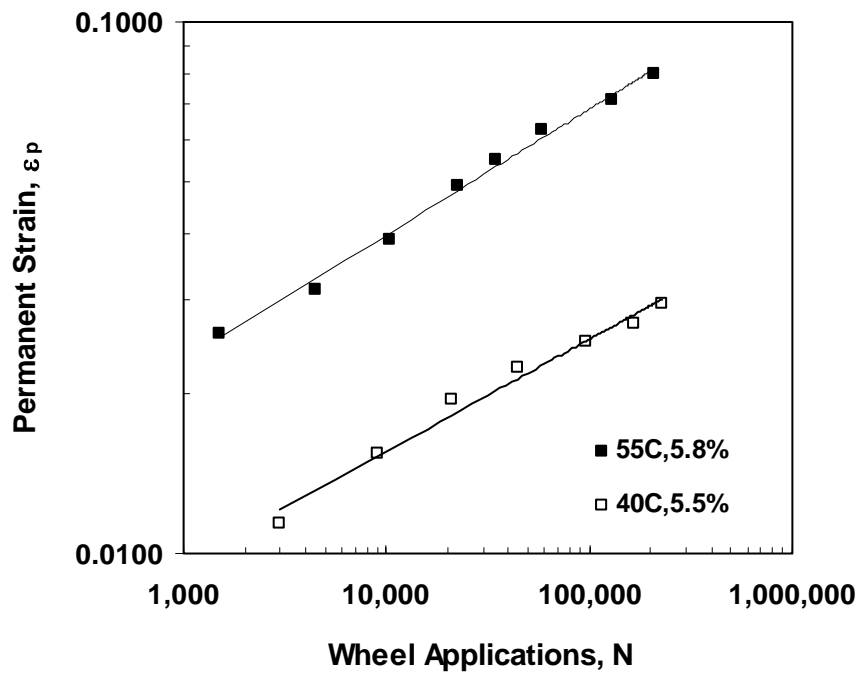


Figure 6.6 Permanent Strain Growth as a Function of Temperature from RI1 Slab

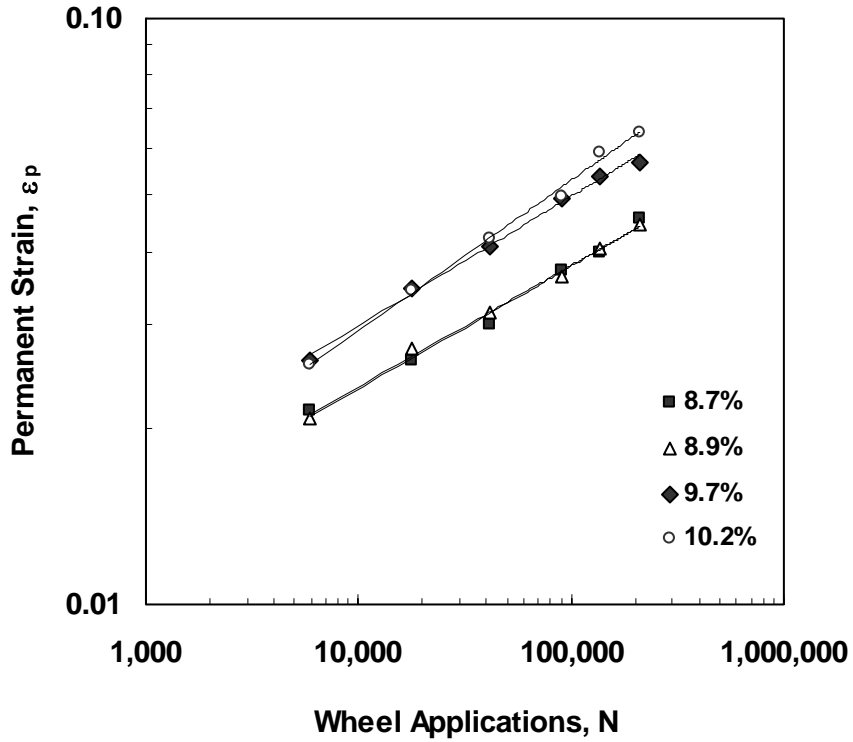


Figure 6.7 Permanent Strain Growth as a Function of Air Void Content from I19C Slab

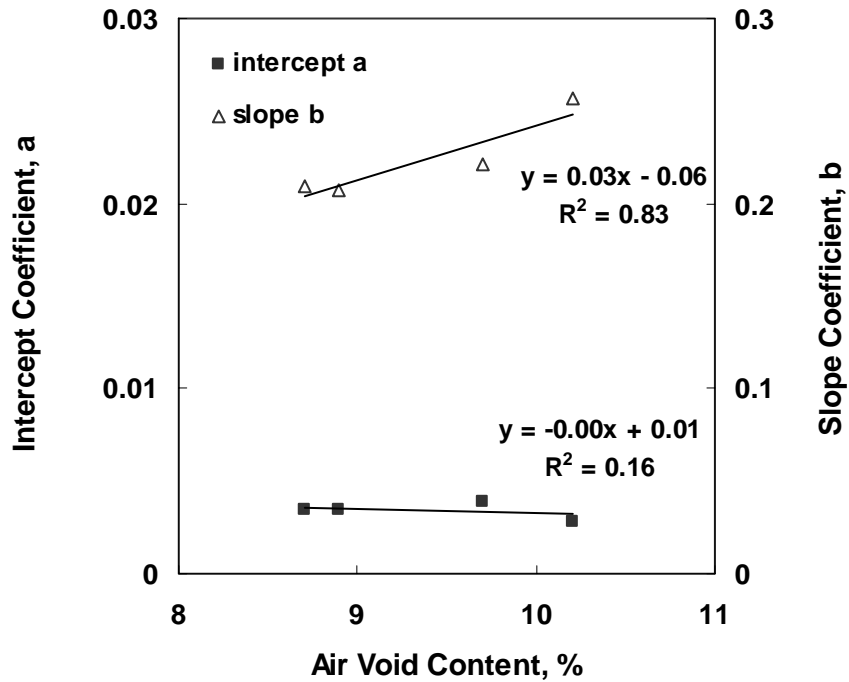


Figure 6.8 Permanent Strain Model Coefficients as a Function of Air Void Contents for I19C-A Slab

Parametric Study for Aging Effect

The stiffness of an asphalt concrete layer may be variable because of material hardening by aging. In order to assess the influence of aging, two slabs of the I19C mix were constructed. One slab was aged for 7 hours (I19C-OV) while the second was aged for 4 hours (I19C-A). Both slabs were then subjected to loading by the MMLS3 and rut depths were measured. Figure 6.9 shows the difference in permanent deformation performance as represented by the average permanent strain. The hardened pavement (7-hour aging) rut depth (i.e., permanent strain) was approximately 50% of that for the slab aged only 4 hours, even though it had a 10% higher air void content. The relationships between average permanent strain (ratio of rut depth to layer thickness) and numbers of applied loads were determined to be:

- For 7-hour aging: $\epsilon_p = 0.0017 (N)^{0.2368}$
- For 4-hour aging: $\epsilon_p = 0.0028 (N)^{0.2567}$

It can be concluded that with increased aging from 4 hours to 7 hours, the “a” term decreased by 39% but the “b” term decreased by 8%.

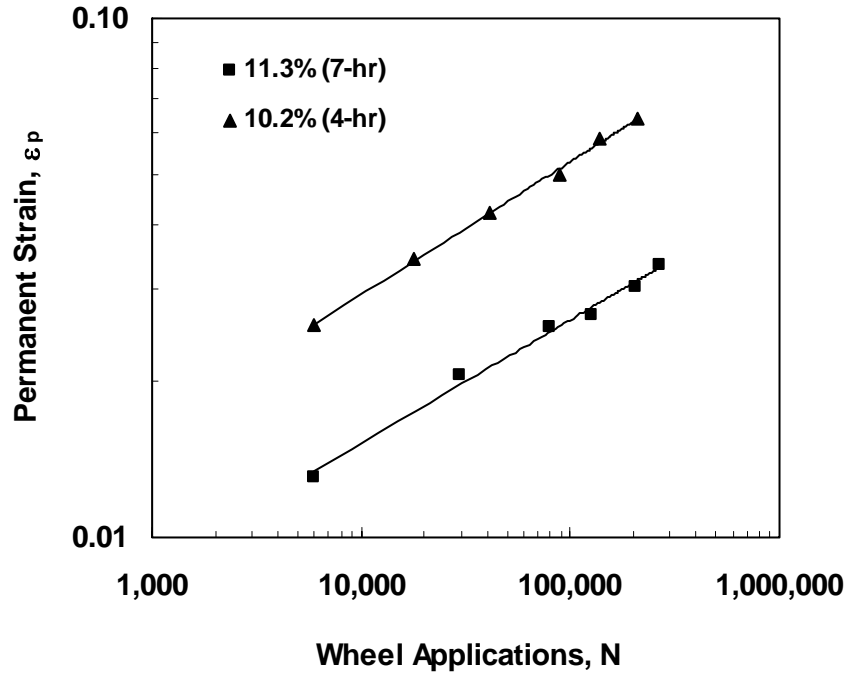


Figure 6.9 Aging Effect on I19C Pavements

6.4.3 PAVEMENT SERVICE LIFE ANALYSIS

According to Epps (2001), a 10 mm failure criterion under full-scale loading corresponds to about 5 mm under the MMLS3 after 100,000 load repetitions. Using the 5 mm - rut depth failure criteria provided, rutting performance acceptability can be assessed. A summary of the rutting results is shown in Table 6.2. It is apparent from the results obtained in this study that temperature has a significant effect on rutting of asphalt mixes. At 55°C, all AC slabs failed long before 100,000 wheel load applications. At 40°C, only the RI-2 (7.1%), I19C-A (9.7%), and I19C-A (10.2%) slabs failed according to the failure criterion at 100,000 repetitions. Rutting failure was observed on pavements with higher than 9.7% air void content for 19 mm NMSA and 7.1% air void content for 9.5 mm NMSA.

Table 6.2 Structural Deformation Results

Test	Temp. (°C)	Air Void (%)	Cycles to Failure (5 mm)	Rut Depth At 100,000 Cycles (mm)	Total Applied Wheels	Final Rut Depth (mm)
RI-2	55	8.4	2,380	N/A ^a	62,270	14.0
		9.6	1,700	N/A ^a		20.0
RI-2	40	6.4	N/A ^a	N/A ^a	188,800	4.3
		7.1	25,000	6.1 (F) ^c		6.8
RI-1	55	5.8	11,160	8.4 (F) ^c	208,510	10.0
RI-1	40	5.5	N/A ^a	3.3	227,570	3.7
I19C-OA	40	11.3	N/A ^a	3.3	269,480	4.3
I19C-A	40	8.7	161,000	4.4	209,140	5.4
		8.9	158,000	4.5		5.3
		9.7	43,470	6.1 (F) ^c		6.9
		10.2	26,840	6.4 (F) ^c		8.0

Note: a. N/A means Not Available

b. Some values between measurement intervals were determined by piecewise linear method.

c. (F) means rutting failure.

6.5 PERMANENT DEFORMATION PREDICTION ALGORITHM

This section describes the development of a permanent deformation prediction methodology that reflects the actual performance of I19C-A mix under the MMLS3 loading. The MMLS3 permanent deformation was predicted/verified through the proposed algorithm associated with prediction model (Eq. 6.2) elements that could be found from triaxial testing.

As previously discussed in Section 6.4.1, the I19C-A pavement in the environmental chamber was controlled at 40°C. However, the actual temperature of the AC layer varied with depths. The pavement temperature ranged from 35°C at the bottom to 45°C on the surface. Thus, it is reasonable to suspect that this variation in temperature may have an effect on permanent deformation. To evaluate the change of material properties with variation of temperature, triaxial testing was commenced for permanent deformation performance at three temperature conditions: 30°C, 40°C, and 50°C. The triaxial testing was conducted by Mr. El-Haggan in the N.C. State pavement materials research group under the conditions as follows:

- 10 Hz loading frequency (0.1 sec loading and 0.9 sec rest period);
- 827 kPa (120 psi) loading pressure; and
- 138 kPa (20 psi) confining pressure.

As mentioned previously, the range of triaxial testing temperatures is due to calculated critical temperatures based on North Carolina regional weather database (NC DOT report, 2002). Specimens for triaxial testing were fabricated at three air void contents, 8.7, 9.5, and 10.5%, using a laboratory gyratory compactor. A servo-hydraulic Universal Testing Machine (UTM) was used to carry out the triaxial permanent deformation testing.

Assuming that the surface layer, totally 122 mm in height, of I19C-A pavement composed of two lifts may be modeled to consist of four layers; from a top layer to a lower layer, 15.025 (H₁), 15.025 (H₂), 30.05 (H₃), and 60.1 (H₄) mm, respectively. Since permanent deformation mostly occurs close to surface of a pavement, it may be reasonable that the top lift was considered as three layers in the axisymmetric model shown in Figure 6.10.

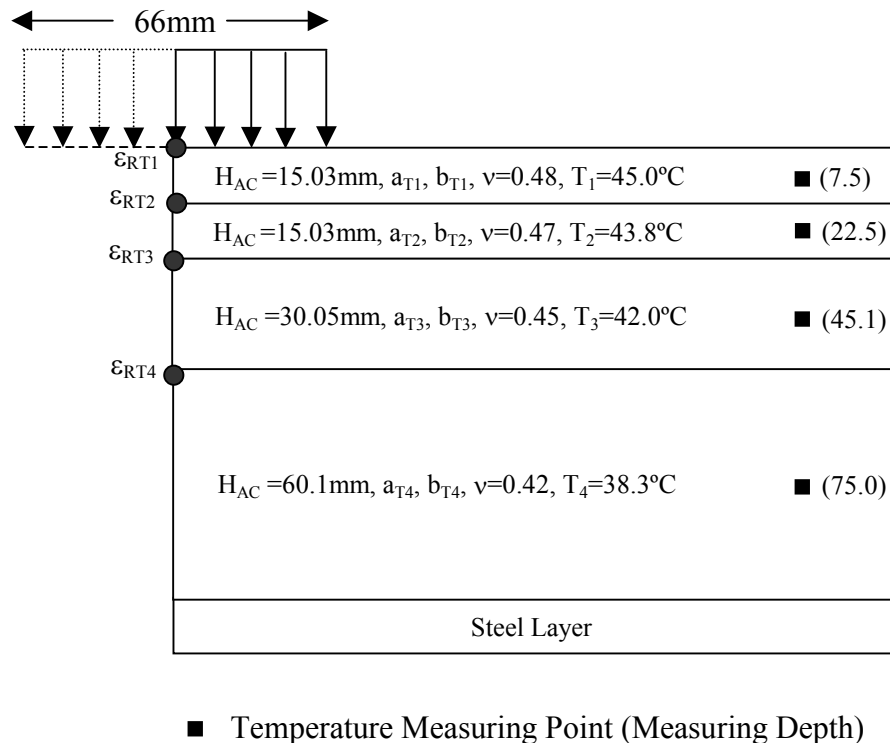


Figure 6.10 Layer Characteristics of I19C-A Pavement for Permanent Deformation Prediction Based on Temperature Variation in the Half Space

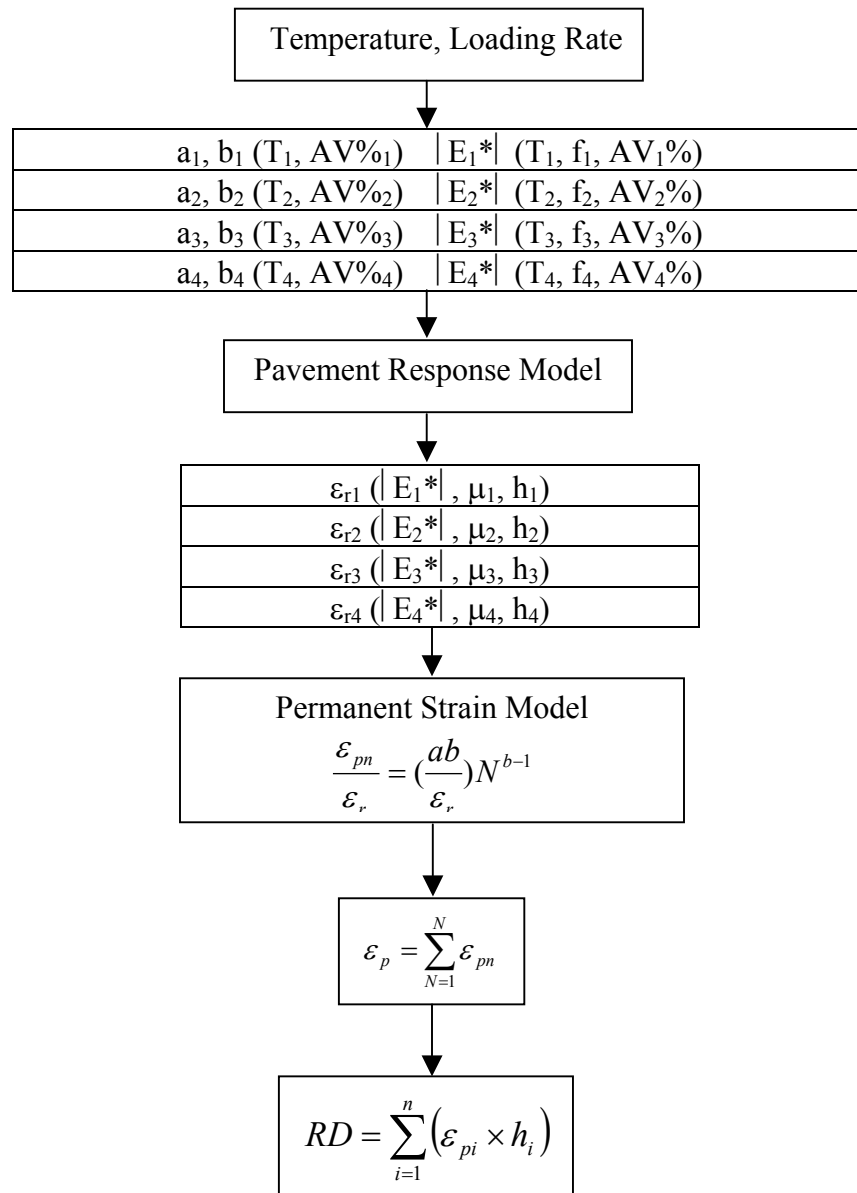


Figure 6.11 Framework for Prediction of Rut Depth

Definitions:

- T: Temperature
- f: Loading rate
- AV%: Air void contents in percentage
- h: Thickness
- μ : Poisson's ratio
- $|E^*|$: Dynamic modulus
- a, b: Permanent deformation regression coefficients
- ϵ_r : Resilient strain
- ϵ_{pn} : Incremental permanent strain due to a single load application
- ϵ_p : Total permanent strain
- N: Number of load applications for a certain group of several hours
- n: Number of sublayers in the asphalt pavement
- RD: Rut Depth

Then, the prediction algorithm for the MMLS3 induced permanent deformation using data from triaxial testing is summarized by the following steps as shown in Figure 6.11:

1. The response of deformation in asphalt concrete shows delayed behavior from the applied loading time due to the time dependent manner of viscoelastic materials (Barkdale (1971), Kim (1994)). The time of loading, 0.3 sec, on the pavement surface, as shown in Figure 2.2, and tensile strain pulse time, 0.6 sec, at the depth of 45 mm in asphalt concrete layer were evaluated. According to Kim (1994), the longitudinal tensile strain pulse time and the depth beneath pavement surface have the linear relationship. On this account, Figure 6.12 was developed and, as shown in Table 6.3, the loading frequencies at depths in the algorithm was determined using the following linear equation:

$$\text{Loading frequency} = -0.037 \times \text{depth (mm)} + 3.33 \quad (6.3)$$

Table 6.3 Loading Frequencies at Measuring Depths

Depths (mm)	7.5	22.5	45.0	75.0
Loading Frequencies (Hz)	3.06	2.50	1.66	0.56

2. It is also assumed that four layers in pavement for algorithm would be constantly maintained at 45.0 (T₁), 43.8 (T₂), 42.0 (T₃), and 38.3 (T₄) °C, which were temperatures at mid-depth of each layer. The mid-depth temperatures are obtained using linear regression analysis of measured temperature data throughout the MMLS3 testing for I19C-A pavement. Figure 6.13 presents the discrepancy between measured and assumed temperatures as a function of depth in algorithm:

$$\text{Temperature} = 0.0819 \times \text{depth (mm)} + 45.665 \quad (6.4)$$

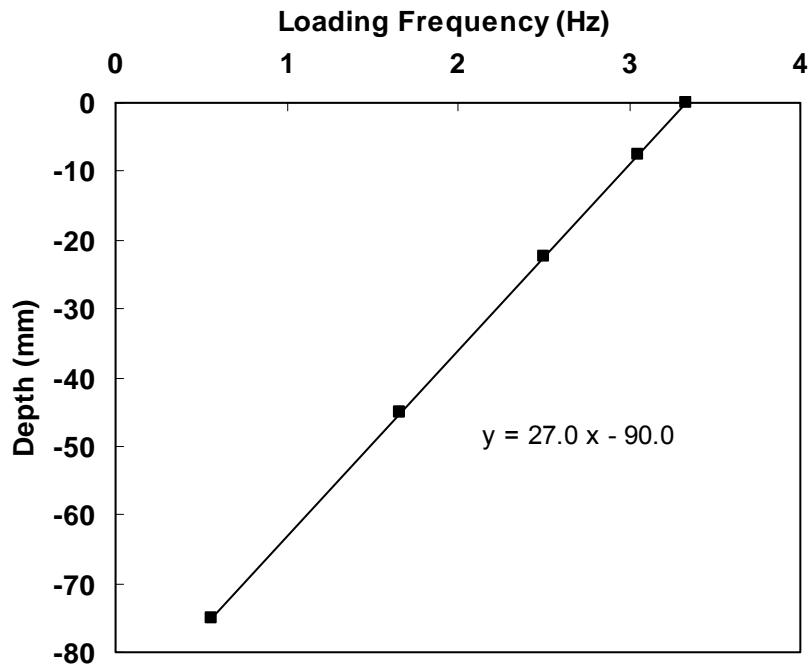


Figure 6.12 Loading Frequency Variation along Depths

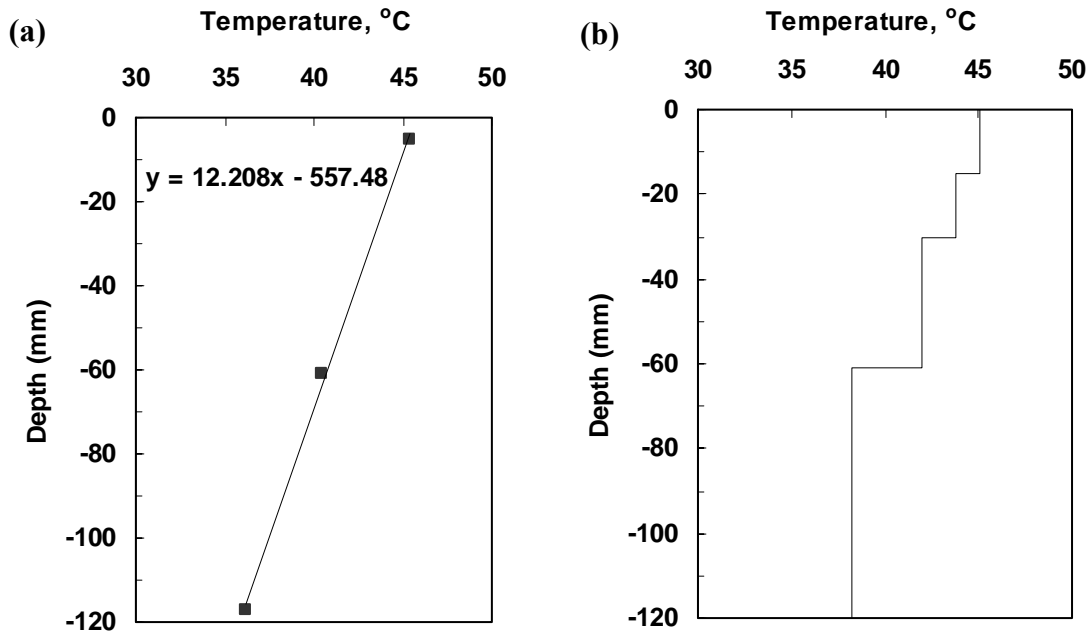


Figure 6.13 Temperature Variation in Depth of Pavement for I19C-A:

(a) Linear Variation in Actual Measurements, (b) Assumed Variation in Algorithm

3. Frequency sweep tests on specimens are performed in the uniaxial testing condition. Master curves were developed from dynamic modulus testing on specimens with different air voids using the time-temperature superposition principle. The following is the sigmoidal function which was used in fitting each master curve:

$$\log |E^*| = a + \frac{b}{1 + \frac{1}{\exp^{d+e(\log f_R)}}} \quad (6.5)$$

where,

$|E^*|$ = Dynamic modulus (MPa),

a, b, d, e = Regression coefficients,

f = Frequency,

a_T = Shift factor,

f_R = Reduced frequency (= f · a_T , Hz).

Since shift factors as a function of temperature are found, the dynamic modulus as a function of temperature and air void content can be determined in Table 6.4.

Table 6.4 Dynamic Modulus Computation Using Uniaxial Testing Program

AV (%)	Temp (°C)	log a_T @3.3Hz	a_T (× E-05)	f_R (× E-04)	a	b	d	e	$ E^* $ @ f_R
8.7	45.04	-4.123	7.525	2.303	1.166	3.276	1.671	0.450	681
	43.81	-4.015	9.657	2.414					693
	41.97	-3.848	14.20	2.357					687
	38.28	-3.495	31.95	1.789					621
9.7	45.04	-4.123	7.525	2.303	1.076	3.334	1.662	0.450	581
	43.81	-4.015	9.657	2.414					592
	41.97	-3.848	14.20	2.357					586
	38.28	-3.495	31.95	1.789					529
10.2	45.04	-4.123	7.525	2.303	1.032	3.363	1.658	0.450	537
	43.81	-4.015	9.657	2.414					547
	41.97	-3.848	14.198	2.357					542
	38.28	-3.495	31.954	1.789					488

4. According to Chehab (2002), from a time-temperature superposition principle, strain values for a particular test history can be predicted by performing a test with the same loading history and the same reduced time history at different temperature. In other words, strain history at different temperatures is overlapped with the same reduced time and loading history. Based on this observation, the strain history by the MMLS3, which has various loading times as a function of depths, is predicted with loading time (10 Hz) of 0.1 sec in the triaxial testing using a shift factor at different temperature. As a shift factor is applied to convert a loading frequency at a measured temperature to a triaxial loading frequency of 10 Hz, the reduced temperatures at 10 Hz are obtained as following in Table 6.5:

Table 6.5 Computation Method for Reduced Temperatures at 10 Hz Loading Equivalent to Temperatures at Different Loading Frequencies

T_0 (°C)	10			
Layer	1	2	3	4
Measured Temp, T_M , (°C)	45.04	43.81	41.97	38.28
$\log(a_{TM})$	-4.1235	-4.0151	-3.8478	-3.4955
Shift Factor, a_{TM}	7.525E-05	9.657E-05	1.420E-04	3.195E-04
Mk3 Loading Freq (Hz)	3.06	2.5	1.66	0.56
Reduced Freq. (Hz)	2.303E-04	2.414E-04	2.357E-04	1.789E-04
Triaxial Loading Freq (Hz)	10			
Shift Factor, a_{TR}	2.303E-05	2.414E-05	2.357E-05	1.789E-05
$\log(a_{TR})$	-4.638E+00	-4.617E+00	-4.628E+00	-4.747E+00
Reduced Temp, T_R , (°C)	50.94	50.70	50.82	52.24

5. Resilient strain is the recoverable strain resulting from the compression cycle being applied to the specimen instrumented with LVDTs during the triaxial compression test at 30, 40, and 50°C temperatures. A representative resilient strain value, ϵ_{RM} , can be obtained through the regression analysis as a function of air void content and temperature of T_M . Multi-layered elastic analysis, then, is performed using Everstress 5.0 program in order to determine the resilient strain for all the layers of pavement structure in algorithm. As shown in Figure 6.10, a four-layered structure for I19C-A pavement was considered. Resilient strain values along depths in each layer were computed using given inputs, including dynamic modulus in Table 6.4 and Poisson's ratio, which were based on the MMLS3 testing conditions in temperatures of T_M . Then, average resilient strain value, ϵ_{RP} , of each layer was predicted. Table 6.6 shows the comparative resilient strain values between ϵ_{RM} and ϵ_{RP} .

Table 6.6 Representative Resilient Strain Values of ϵ_{RM} and ϵ_{RP}

Air Void (%)	Temp (°C)	50.94	50.70	50.82	52.24
8.7	ϵ_{RM} ($\mu\epsilon$)	764	729	676	571
	ϵ_{RP} ($\mu\epsilon$)	541	926	733	350
9.7	ϵ_{RM} ($\mu\epsilon$)	805	769	715	606
	ϵ_{RP} ($\mu\epsilon$)	635	1085	859	411
10.2	ϵ_{RM} ($\mu\epsilon$)	826	789	734	624
	ϵ_{RP} ($\mu\epsilon$)	687	1175	930	445

6. From permanent strain profiles as a function of number of loading cycles, a regression analysis was performed between permanent strain (ϵ_p) and load repetitions (N) on the log-log linear relationship. Then, an intercept coefficient, a , and a slope coefficient, b , for the prediction model in Eq. 6.2 were determined. Therefore, “ a ” and “ b ” values as a function of temperature and air void content were obtained (Appendix D). The multivariable regression analysis to the coefficient, “ a ” or “ b ”, for temperature and air void content relationship enables model coefficients to be obtained as shown in Table 6.7.

Table 6.7 Regression Constants for Temperatures and Air Void Content

Air Void (%)	Temp (°C)	50.94	50.70	50.82	52.24
8.7	a	0.00306	0.00303	0.00305	0.00326
	b	0.21691	0.21720	0.21706	0.21499
9.7	a	0.00330	0.00326	0.00328	0.00350
	b	0.23151	0.23173	0.23162	0.22996
10.2	a	0.00342	0.00338	0.00340	0.00362
	b	0.23881	0.23900	0.23891	0.23745

7. All elements found at each layer were substituted into the prediction model in Eq. 6.2. Using the Matlab program, the permanent strain (ϵ_{pn}) in each layer resulting from a single load application at each layer is predicted by integration using an adaptive integral quadrature. In Eq. 6.2, ϵ_{pn} is the permanent strain due to a single load application. Thus, each permanent strain was calculated and added to get cumulative permanent strain for $n = 1$ to N until failure. Since each permanent strain value was multiplied by the layer thickness, respectively, the

rut depth for a layer can be computed. At the end, the total rut depth, RD, is then obtained by adding the displacement contributions from each model layer as follows:

$$RD \text{ (total)} = \sum_{l=1}^4 [\varepsilon_p(l) \times h_l] \quad (6.6)$$

where,

l = Number of layers in algorithm

Figure 6.14 presents the development of measured and predicted rut depths as wheel applications increase. Table 6.8 summarizes the results of rut depth prediction. As seen in Figure 6.14, it can be found that the proposed algorithm performed in approximately 17, 13, and 3% difference between measurement and prediction for permanent deformations of 8.7, 9.7, and 10.2% air void contents, respectively. The resulting rut depth was 5.47 mm for 8.7% air voids and was 7.96 mm for 10.2% air voids. Therefore, the rut depth in case of 10.2% air voids was 1.5 times more than the rut depth in case of 8% air voids. It means that the 10.2% air voids pavement will reach failure earlier, and it, therefore, will have less service life than the in-specification pavement with 8% air voids. Using this algorithm in this research, the amount of rutting is expected almost 1.7 times in the case of the 1.5% deficient pavement between 8.7 and 10.2% air voids.

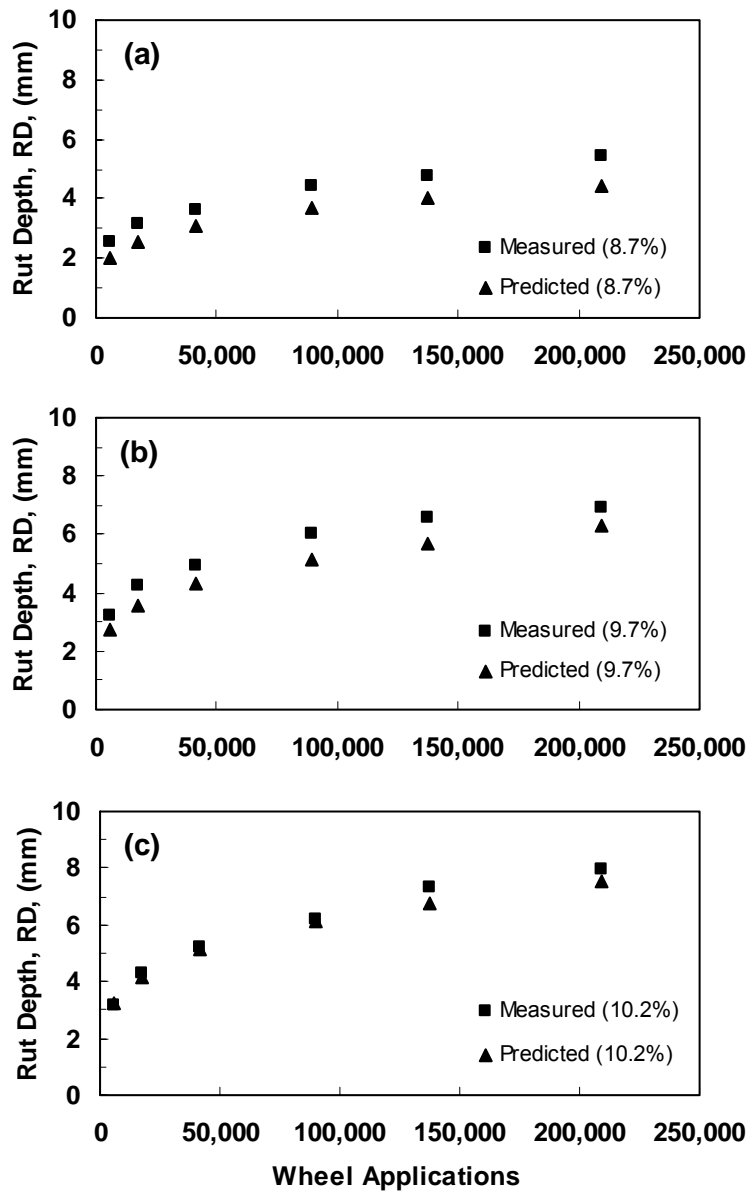


Figure 6.14 Comparison of Measured / Predicted Rut Depths in 4-layered Structure for Air Void Contents of: (a) 8.7%; (b) 9.7%; (c) 10.2%

Table 6.8 Results of Rut Depths (RD) Using Prediction Algorithm

Wheel Applications	Air Void Content (%)								
	8.7			9.7			10.2		
	RD _M	RD _P	D (%)	RD _M	RD _P	D (%)	RD _M	RD _P	D (%)
5950	2.57	2.04	20.75	3.19	2.76	13.36	3.18	3.21	0.97
17790	3.12	2.58	17.27	4.23	3.56	15.95	4.27	4.17	2.41
41600	3.61	3.11	13.99	4.96	4.33	12.69	5.22	5.11	2.24
89730	4.46	3.67	17.76	6.01	5.17	14.00	6.18	6.13	0.83
137320	4.78	4.02	15.91	6.56	5.70	13.16	7.30	6.79	7.03
209140	5.45	4.40	19.24	6.94	6.29	9.42	7.96	7.51	5.67

Note: RD_M is the rut depth in measurement
RD_P is the rut depth in prediction
D is the difference in percentage between RD_M and RD_P.

There are several possible reasons to cause errors using this algorithm. Firstly, as shown in Figure 6.11, each layer temperature in the model pavement was determined using linear regression based on measured three points. Because temperature is the most critical factor in the algorithm, any experimental errors in these values have a significant effect. Accordingly, it might be desirable in further testing to add a fourth or fifth temperature sensor across the pavement depth. Structural analysis of the surface AC layer in the algorithm may be more accurate if performed with an increase of number of layers.

Secondly, “a” and “b” parameters and dynamic moduli, as an input for EverStress program, at desired air void contents on temperatures of layers can be obtained through regression analysis of data for triaxial specimens by means of their linear relationships. Accuracy of performance prediction, therefore, significantly correlates the intensity of linear relationship in parameters or material properties for triaxial specimens.

Thirdly, as explained at Step 4 in prediction algorithm, strain history by short loading time and short rest period at higher temperature is to be same by long loading time and long rest period at lower temperature under the time-temperature superposition principle. However, in the MMLS3 loading history, as the loading time increases along depths, the rest period rather decreases because the loading period of MMLS3 is fixed at 0.6 sec. Hence, the reduced temperatures, which were found at Step 4 in algorithm, strictly does not satisfy the condition of the rest period in MMLS loading to be same strain history. It can contribute to make the difference between prediction and measurement of permanent deformation as shown in Figure 6.13.

6.6 SUMMARY

The rutting performance on model asphalt concrete pavement was investigated using the MMLS3 in this Chapter. After pavement construction and testing method for rutting were effectively established, surface profiles were measured and evaluated. Using parametric study enables to evaluate effect of material properties and testing conditions on performance. Cyclic triaxial compression testing program was incorporated to predict the permanent deformation of the MMLS3 tests. The prediction algorithm was formulated and successfully verified.

CHAPTER 7

FIBER REINFORCED ASPHALT CONCRETE (FRAC)

7.1 INTRODUCTION

It is well known that embedded fibers improve the properties of a wide variety of media in terms of ductility and energy absorption. Numerous fiber composite materials are available for a variety of applications using these advantages. Fiber inclusion can be one of the effective ways of improving the properties of concrete pavements. However, since little work has been done on flexible pavement, it is the objective of two studies to evaluate the feasibility of using fiber reinforced asphalt concrete to improve mechanical properties for better fatigue performance.

It is difficult to characterize the crack resistance of an asphalt concrete pavement system because of the complexity of the cracking phenomenon. In the fracture process, when a crack starts to develop in a material including fibers, fibers bridging the crack can provide resistance to crack propagation and crack opening prior to pullout or rupture. Previous research (Bentur, 1990, Kwak and Kim, 1995) indicated that even with low modulus synthetic fibers, considerable improvements in the strain capacity, impact resistance and crack control of fiber composites would be expected.

This chapter reports on an experimental program to evaluate the mechanical properties of asphalt concrete containing nylon fibers and any increase in cracking resistance of the composite material. Nylon, a popular facing yarn of carpet fibers, was selected because the experience from this investigation may suggest the use of actual recycled carpet fibers in asphalt concrete composites in the future. Single fiber pullout

tests for a single nylon fiber and indirect tensile strength tests on fiber reinforced asphalt concrete were performed. Test results will be presented and discussed in the following sections.

7.2 Background

As advances in technology have caused development of construction materials, recent research has been directed toward increasing the serviceability and safety of structures using fibers as concrete reinforcement. Since the early use of asbestos fibers, a wide variety of other fibers such as steel, glass carbon, Kevlar, polypropylene and nylon have been used with hydraulic cements. These types of fibers vary considerably in properties, effectiveness and cost (Bentur, 1990; Beaudoin, 1990; Harris, 1999). Most of developments with fiber reinforced concrete (FRC) involve the use of ordinary Portland cements at this time.

Reinforced concrete beams with a polymer fraction have been investigated (Kwak, 1995). The beams were designed to take static and fatigue loads. Fatigue life of fiber reinforced concrete is drawing significant attention for two reasons. First, FRC is finding increasing use for applications such as pavements where their short-term properties are advantageous. Second, civil infrastructures constructed decades ago are deteriorating with increasing speed. At the time of construction, long-term durability was expected. The increasing use of FRC requires both low life-cycle cost and high long-term durability primarily measured as a long fatigue life in applications where high cycle fatigue loading is expected. Polyvinylidene chloride (PVDC) is used to produce polymer-reinforced concrete. Kwak (1995) showed that the PVDC reinforcement with a higher

solid content of the polymer contributed to an increase in the compressive and tensile strengths as well as an improvement in the durability of the concrete.

Li and Matsumoto (1998) presented an analytic model for fatigue crack life prediction in fiber reinforced concrete. Crack bridging stress in FRC is exerted by fibers and aggregate, so the cyclic constitutive law of FRC can be obtained by the superposition of crack bridging stress-crack opening displacement relations due to both fiber and aggregate under cyclic loading. The model explains fatigue crack growth in cementitious matrix material under the influence of external cyclic loading and fiber and aggregate bridging.

Wang (1987) reported experimental results on the properties of various synthetic fiber reinforced cementitious composites and the properties of the reinforcing fibers. Volume fractions of 2 to 6.5 % of synthetic fibers - such as acrylic, polyester, and aramid fibers - mixed during preparation of a cement matrix contributed to improved specimen resistance to failure in a compact tension test, the splitting tensile test, and the four-point beam bending test. Interestingly enough, Wang (1994,2000) also evaluated the use of recycled fibers from carpet industrial waste for reinforcement of concrete at 1 and 2 % volume fractions. The US carpet industry produces about 1 billion m² of carpet and consumes about 1 million tons of synthetic fibers. A carpet typically consists of two layers of backing (usually polypropylene) filled styrene-butadiene latex rubber (SBR), and face fibers (the majority being nylon 6 and nylon 6.6) tufted into the primary backing. The nylon face fiber is often in the form of a heavily crimped loose filament bundle known as a textured yarn. The typical recycled carpet fiber length ranges from 12–25 mm. The flexural strengths from the four-point beam bending test for the FRC

specimens show a pseudo-ductile behavior by which fibers bridging the beam crack can be shown. Rather, the plain concrete samples broke into two pieces once the peak load was reached, with very little energy absorption.

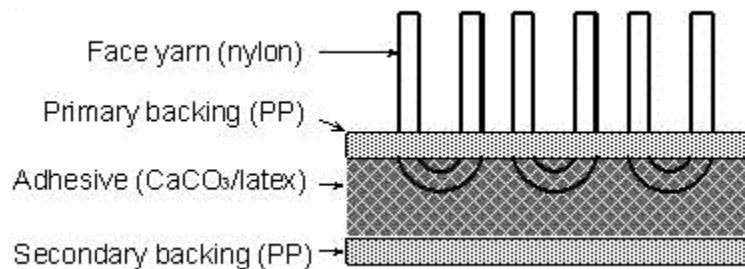


Figure 7.1 Illustration of Tufted Carpet Structure (Wang, 1994)

Serfass and Samanos (1996) generally introduced fiber-modified asphalt concrete characteristics, applications and behavior. According to their conclusions, fiber incorporation has proved to be a practical and dependable technique for improving asphalt concrete. Accurate proportioning of fibers and bitumen is essential and requires special attention. Adding fibers enables developing mixes rich in bitumen, and then displaying high resistance to moisture, ageing, and fatigue cracking. Tests proved the existence of an optimal fiber content, which depends on the nature of the fibers. This optimal content corresponds to the best compromise obtainable between two competing effects generated by the fibers:

- The increase in resistance against shear and extrusion brought by the locking and the reinforcement, and
- The reduced resistance, beyond a specific threshold, due to a decrease in compactability and therefore a loss of density.

Peled (1999) investigated the influence of a woven fabric structure on the flexural behavior of cementitious composites. The fabrics used were plain weave with various fills densities while the warp density was kept constant. The yarns were monofilament polyethylene. While preparing the composite, intensive vibration was applied to achieve better penetration of the cement matrix between the fabric openings. It was found that the fabric structure did not provide a composite with better properties. Weakening of the matrix due to less efficient compaction was detected. Chang (1999) applied several geogrids to study the formation and development of fatigue cracks in asphalt concrete beams. For a beam reinforced with glass geogrids, the fatigue life was 5 to 9 times that of an unreinforced beam. It was observed that the fatigue life of the pavement overlay was improved.

Maurer and Malasheskie (1989) studied whether uses of geotechnical fabrics and fibers could significantly retard reflective cracking in an asphalt concrete overlay. Among paving fabrics, fiberized-asphalt membrane and fiber-reinforced asphalt concrete provided better performance over non-reinforced samples in comparisons of construction, maintenance costs, ease of placement, and the ability to prevent or retard reflective cracking. The fiber reinforced asphalt mix formulation was 0.3 % volume fiber content. The fibers were added to the mix at the beginning of the dry mixing cycle along with the dried aggregate. Saraf proposed the improved effect of reinforcement on the fatigue lives of the beams. Their analyses indicated that beams reinforced with woven grid and nonwoven fabric composites performed significantly better than beams containing nonwoven paving fabric alone.

Huet et al. (1990) conducted comparative experiments on several porous asphalts with high void content (about 20 %) using the Nantes circular fatigue test track, which is designed to accelerate the effect of heavy traffic. Pure asphalt cement, elastomer (SBS) modified binder, and pure bitumen and fiber were selected. It was concluded that performance was improved by the addition of higher reinforced porous asphalt.

According to Jenq et al. (1993), fiber reinforcement was found to slightly increase the crack resistance of the asphalt concrete overlays because the addition of fibers to asphalt mixes in general increases the fracture energy by 50 to 100 %, which implies that the fiberized mix is tougher and more ductile. Fiber addition, however, seems to have little effect on the material's modulus of elasticity or its tensile strength.

Jiang and McDaniel (1993) evaluated two methods for reducing reflective cracking of an asphalt overlay over a concrete pavement. The first method, cracking and seating, breaks the existing concrete pavement slabs into smaller pieces and then seats these pieces by rolling to achieve uniform contact between the individual slab pieces and the base layer before placement of the asphalt overlay. The second method involved the addition of polypropylene fibers to the asphalt overlay to increase the tensile strength of the asphalt mixture. Kim et al. (1999) also sought to evaluate the performance of polymer-modified asphalt mixtures and reinforcement techniques against reflective cracking for typical asphalt pavement overlays. Low-density polyethylene (LDPE) plus 6 mm long polyester fiber had a significant tensile reinforcing effect on the asphalt mixture using the indirect tensile strength test. In addition, fiber seems to be necessary to extend significantly the fatigue life of mixtures. Reinforced mixtures have the effect of extending fatigue life by approximately 20-25 times that of plain asphalt mixtures.

7.3 MECHANICAL PROPERTIES OF FIBER-EMBEDDED CEMENT CONCRETE

7.3.1 FIBER-CEMENT INTERACTION MECHANISM: STRESS TRANSFER

The reinforcing function of fibers in the cementitious matrix comes from two aspects: (1) the process by which load is transferred from the matrix to the fibers; and (2) the bridging effect of the fibers across the matrix cracks, which occurs at a further stage of loading.

According to Bentur (1990), in brittle matrix composites, elastic stress transfer is the major mechanism before any cracks occur and the longitudinal displacements of the fiber and matrix at the interface are geometrically compatible. The stress developed at the interface is a shear stress that distributes the external load between fibers and matrix, so that strains of these two components at the interface remain the same.

As loading proceeds, debonding across the interface can take place, and the process controlling stress transfer becomes one of frictional slip. In this case relative displacements between the fiber and the matrix take place. The shear stress, assumed to be uniformly distributed, develops the frictional stress along the fiber-matrix interface. This process is of most importance in the post-cracking case, in which the fibers bridge across cracks. Properties such as the ultimate strength and strain of the composite control this mode of stress transfer. The transition from elastic stress transfer to frictional stress transfer occurs when the interfacial shear stresses due to loading exceed the fiber-matrix shear strength (adhesional strength, τ_{au}). As this stress is exceeded, fiber-matrix debonding is initiated, and frictional shear stress will act across the interface in the debonded zone. The maximum frictional shear stress is called by τ_{fu} (Bentur, 1990).

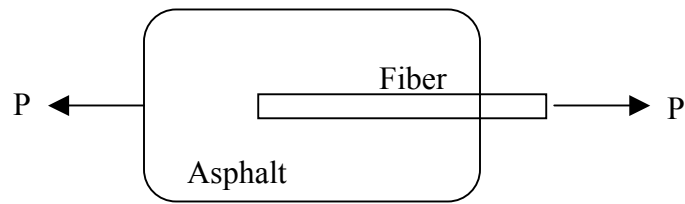


Figure 7.2 Pull-out Geometry to Simulate Fiber-Matrix Interaction

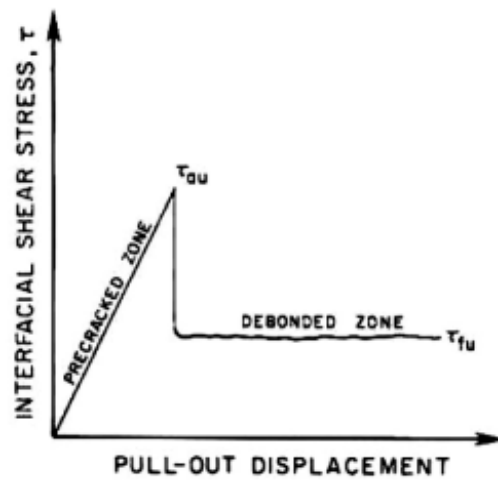


Figure 7.3 Pull-out Displacement Curve with a Transition from Elastic Stress Transfer to a Constant Frictional Stress Transfer (Bentur, 1990)

7.3.2 FIBER LENGTH EFFECT

The actual composite may consist of short fibers dispersed in the matrix. The contribution of short fibers to the mechanical properties of the composite is smaller than that of long fibers oriented parallel to the load. A critical length parameter, L_c , can be defined as the minimum fiber length required for the build-up of a stress in the fiber which is equal to its failure load. For $L < L_c$, there is not sufficient embedded length to generate a stress equal to the fiber strength, and the fiber is not utilized efficiently. If the length of the fiber considerably exceeds L_c the stress along most of the fiber may reach its tensile strength. It, thus, utilizes the potential of the fiber reinforcement. For a frictional shear transfer, the calculated value of L_c is: (Bentur, 1990)

$$L_c = \frac{\sigma_{fu} \cdot r}{\tau_{fu}} \quad (7.1)$$

where, σ_{fu} = fiber strength,

r = fiber thickness, and

τ_{fu} = frictional shear strength

7.3.3 CRITICAL FIBER VOLUME FRACTION

In cementitious fiber composites, the failure strain of the fiber is generally greater than that of the matrix which fails first. When the matrix cracks, the fibers either carry the additional load or the composite fails. The minimum (critical) fiber volume fraction, V_{cr} , required for the composite to sustain the load after matrix fracture occurs is given as (Beaudoin, 1990):

$$V_{cr} = \frac{\sigma_{mu}}{\sigma_{mu} + (\sigma_{fu} - \sigma_f')} \quad (7.2)$$

where, σ_f' = stress on the fibers when the matrix fails,

σ_{mu} = ultimate strengths of the matrix, and

σ_{fu} = ultimate strengths of the fiber

7.4 FIBER-ASPHALT PULLOUT TEST

Measurements of pullout under constant rate of elongation tensile testing condition were performed at 20°C. Single nylon fibers, manufactured by Mini Fiber Inc., were tested for debonding and tensile behavior as a function of embedded length of fiber. The fibers were embedded different lengths into the series of disposable 3 oz. cup filled with asphalt binder. The details of specimen preparation and testing are presented in the following sections.

7.4.1 SPECIMEN PREPARATION

Pullout test samples were fabricated by two different methods based on embedded length (L_{emb}) of fibers. For specimens of $L_{emb} > 10$ mm, a container for the test was prepared by piercing its bottom with a needle. A single fiber of 300 mm was straight installed through the bottom of the container. The one end of the fiber through the bottom of container was attached outside of the testing container and the other end was fixed on the pullout device. Asphalt binder at 100°C was ready and poured into the container just to hold the fiber. After cooling, the fiber was marked by black ink on measure of a pullout device which is shown in Figure 7.4 and a razor cut the end of the fiber at the bottom to be free for pull-up. Then, the container was filled with hot asphalt binder that

was ready at 120°C and the fiber was carefully pulled up to desired height along the measure on the device. When the fiberized asphalt container was cool, the actual embedded length of fiber was determined by measuring the extruded fiber length from the surface of the asphalt to the end of the fiber.

For specimens of $L_{emb} < 10$ mm, a container was firstly filled with asphalt without piercing on the bottom. Since a single nylon fiber is so light and tends to float in hot asphalt, it was not easy to control embedding the fiber shorter than 10 mm using the method above. Thus, the fiber was embedded from surface of asphalt. For this embedding method, 100 mm long fibers were ready. In asphalt of the container at room temperature, a 3 mm approximately wide hole was made to a desired depth on the surface using a small nail. After the fiber was put down all the way in the hole, the container with fiber was heated for 15 minutes in an oven at 135°C to get a smooth surface and proper bonding.

7.4.2 TEST CONFIGURATIONS

The pullout tests for nylon fibers in an asphalt matrix were performed as illustrated in Figure 7.2, at the Physical Testing Laboratory in the College of Textile at N.C. State University. For an asphalt container, it was necessary to design and fabricate an attachment to assist with the pullout test. The pullout tests were performed on a SYNTECH testing machine. A 5-lb load cell was used to measure the load and the data was recorded by a data acquisition system. The loading rate was 300 mm/min, which rate is specified in ASTM D2256 for yarn tensile strength testing. The testing setup used is shown in Figure 7.5.

The gauge length of 30 mm is determined as the minimum length between the surface of the container and the grip of SYNTECH. It is preferred to use a shorter gauge length to reduce undesirable effects from an exposed fiber.

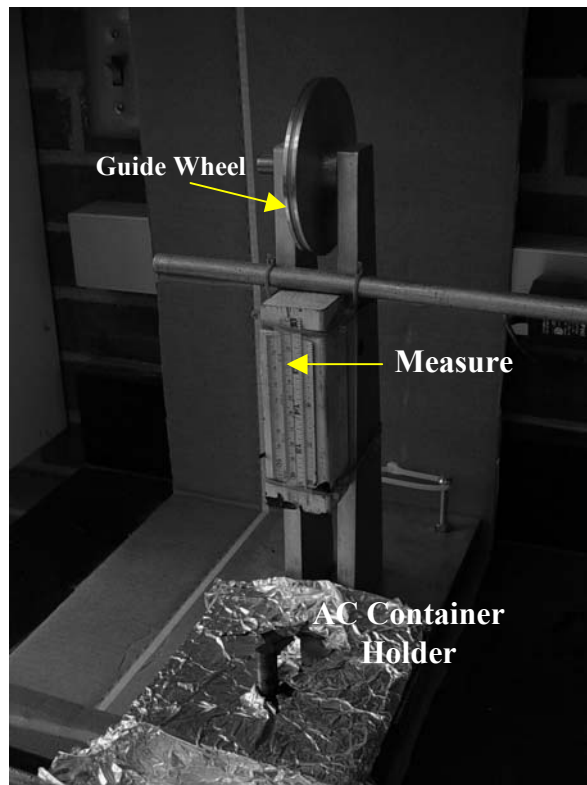


Figure 7.4 Pullout Testing Device

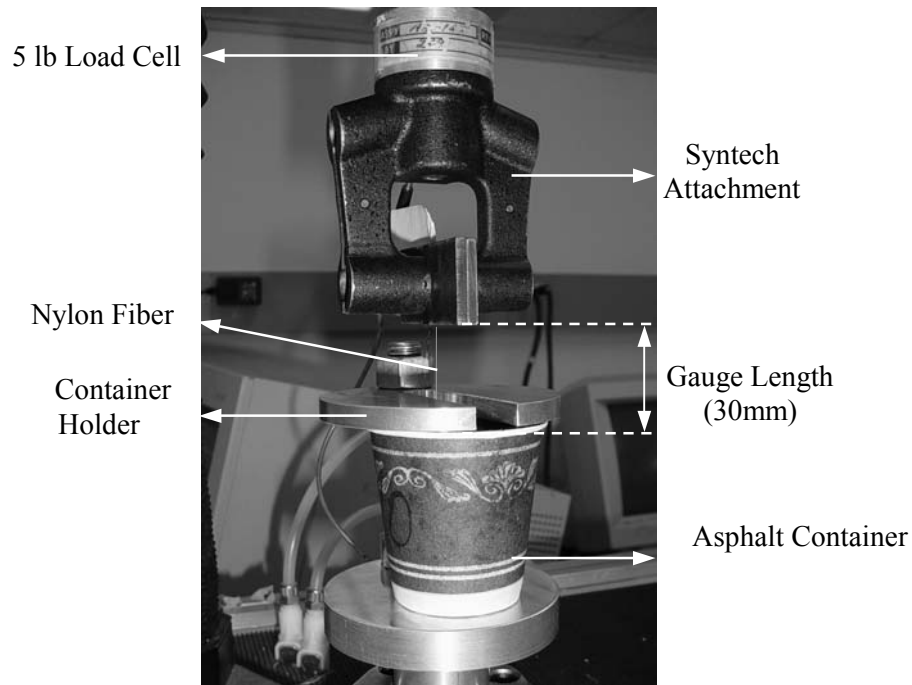


Figure 7.5 Nylon Pullout Test Setup

7.4.3 *PULLOUT TEST RESULTS*

Direct fiber pullout tests from an asphalt matrix were conducted with nylon fiber. The material properties for typical facing fibers from carpet were considered to select fiber type, thickness, and length. For this reason, 15-denier nylon fibers were used and since the actual length of waste carpet fiber is to be approximately 19 mm according to Wang (1994), fibers shorter than 20 mm were selected for all tests.

According to Bentur (1990), as presented in Figure 7.6, the curve of pullout load versus fiber displacement, which is resulted from the actual pullout test for a 6 mm embedded nylon fiber in this study, can be interpreted as follows:

1. Intact interface occurs by elastic bonding in O – P period.
2. At P, the elastic bond starts breaking by the pullout force. It results in the change of slope in the diagram.
3. After gradual debonding process was observed in the P – R period, the load reached the maximum load at R. It means the termination of the debonding process. The sudden drop in load follows. Then, the fiber slips out without any observation of frictional resistance that may build additional fiber extension to a certain extent after sudden drop of load.

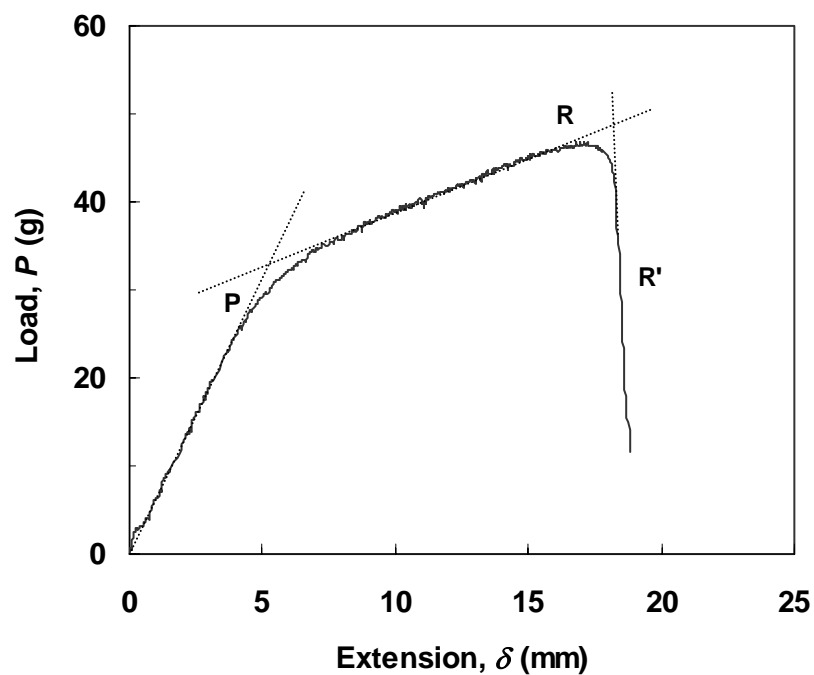


Figure 7.6 Illustration of Relationships between Pullout Load and Fiber Extension
Using 6 mm Embedded Fiber Tested

It can be seen that the actual embedded length of nylon fibers were accounted for in this study. The average maximum load at failure (P_{break}) in fiber tensile testing was found to be 60.48 gram. From the regression analysis between fiber embedded length and fiber pullout load in Figure 7.7 based on measured data in Table 7.1, it was found that fiber rupture during pullout occurred on fibers embedded approximately 9.2 mm or longer.

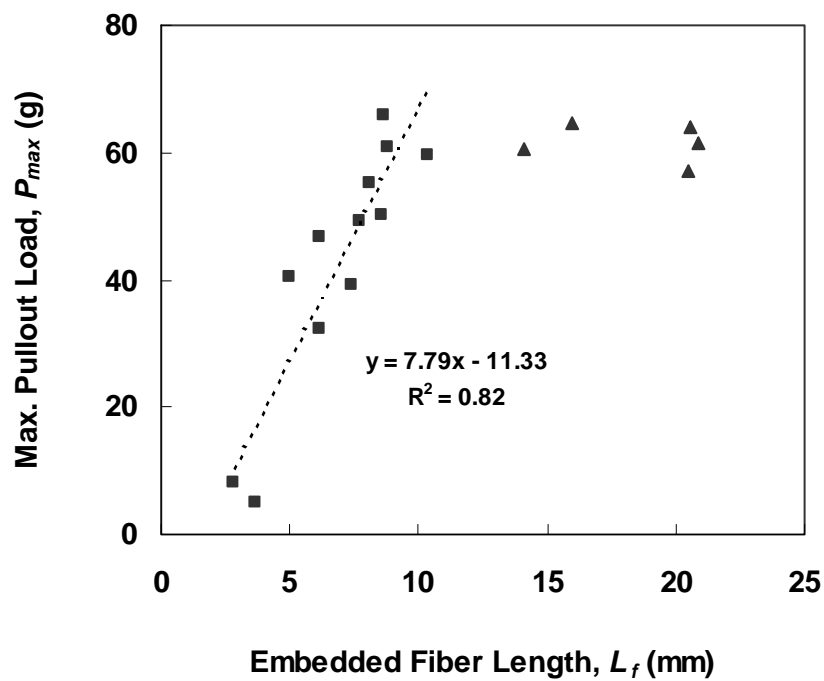


Figure 7.7 Embedded Fiber Length versus Pullout Load

Note: data (▲) not used in regression analysis (fibers did not pullout)

Table 7.1 Pullout Testing Results

Embedded Fiber Length (mm)	Pullout Load (g)
2.79	8.31
3.66	5.14
4.96	40.60
6.14	32.28
6.19	46.71
7.38	39.13
7.74	49.40
8.10	55.27
8.66	66.03
8.59	50.13
8.79	60.92
10.39	59.69
14.12	60.43 *
15.93	64.59 *
20.50	57.25 *
20.58	63.85 *
20.90	61.41 *

*Note: “ * ” did not pullout / ruptured*

7.5 FIBER REINFORCED ASPHALT CONCRETE STRENGTH TESTS

7.5.1 SPECIMEN PREPARATION

According to supplemental specification 826 for asphalt concrete with fibers from the Ohio State Department of Transportation (2000), the mixtures of aggregate, fiber and asphalt binder were presented in the laboratory.

Aggregate gradation for S9.5C-A mix design provided by N.C. DOT for fiber inclusion was used to fabricate 3 fresh IDT specimens of 150 mm x 59.5 mm for IDST using a Superpave gyratory compactor. Both ends of the specimen were evenly cut to be 38 mm high with approximately 8.5% air void content. This aggregate gradation is available in Chapter 3. Nylon fiber volume fractions (V_f) of 0.25, 0.5, and 1%, were calculated based on following assumptions and conditions:

- Assuming that polymeric nylon fiber be a circular cross-section;
- Specific gravity = 1.14;
- Linear density (denier) = 15 (15 g / 9000 m);
- Single fiber diameter = 0.043 mm [$\sqrt{(15 \cdot 4)/(1.14 \cdot \pi \cdot 9 \cdot 10^5)}$]

According to the single fiber volume calculation, the amount of fibers required for S9.5C-A mix was determined as 3.02 g for 0.25% V_f , 6.04 g for 0.5% V_f , and 12.09 g for 1% V_f . After each batch of aggregate was heated at 166°C, measured amount of fibers were placed in the mixing on fine aggregate as a layer and then larger aggregate covered the fiber. The sandwich layers helped the AC binder to be distributed over all fibers as well as fine materials. After mixing, fiber composite mixes were aged for 4 hours at 135°C and then compacted at 155°C.

7.5.2 INDIRECT TENSION STRENGTH TEST (IDST)

The indirect tension strength test is performed on the specimen at a constant crosshead rate until it fails. The testing setup is showing in Figure 7.8. The testing procedure was explained in Section 3.4.2.

The horizontal tensile stress can be calculated using the elastic solution for the IDT geometry:

$$\text{Horizontal Tensile Stress} = \frac{2P}{\pi d} \quad (7.3)$$

where,

P = the applied load (gram);

d = the diameter of the specimen (15.24 mm); and

t = the thickness of the test specimen (mm)

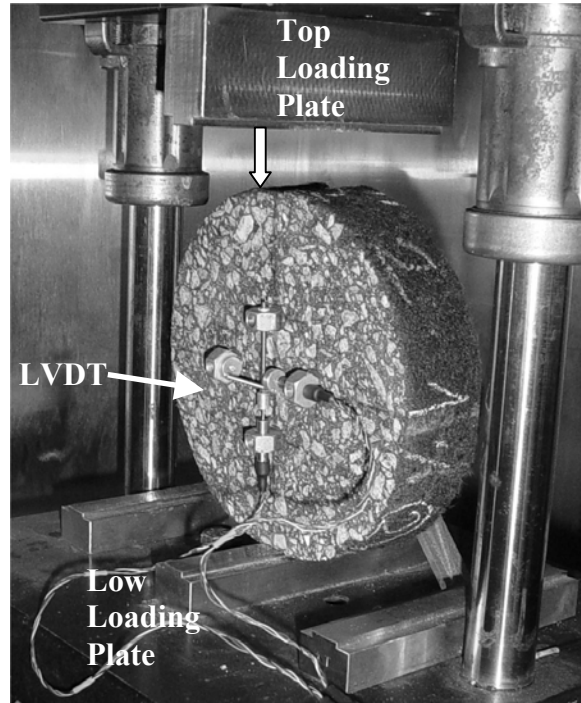


Figure 7.8 IDST Setup

7.5.3 TEST RESULTS

The tensile stress-strain was almost linear up to the maximum point, at which point it was immediately decreasing as shown in Figure 7.9. Before final rupture a damage zone, or fracture zone, formed in the testing specimen. The further increase of deformation caused increasing damage in the fracture zone and a decreasing strength. Thus a descending stress in the specimen resulted whereas the deformation was increasing due to the existence of the fracture zone.

Figure 7.10 is the schematic diagram to illustrate “*Work potential theory*” which is based on an irreversible thermodynamic process, at which the total energy, W_T , done by the load is conserved as the sum of the strain energy, W , and the dissipated energy, W_s , which contributes to changes in the structure, as follows:

$$W_T = W + W_s \quad (7.3)$$

where,

$$W_T = \int_0^{\varepsilon_{\sigma=MAX}} \sigma d\varepsilon ; \quad (7.4)$$

$$W = \frac{1}{2} \sigma_{\max} \varepsilon_{\sigma=\max} ; \text{ and} \quad (7.5)$$

$$W_s = W_T - W \quad (7.6)$$

Assuming that the stress increases until it is σ_{\max} , resulting in the displacement $\varepsilon_{\sigma=\max}$. At this time, visible cracks and fractures appear and begin to expand. During this process, there must be energy conservation. W_s is the work expended in fracturing the material.

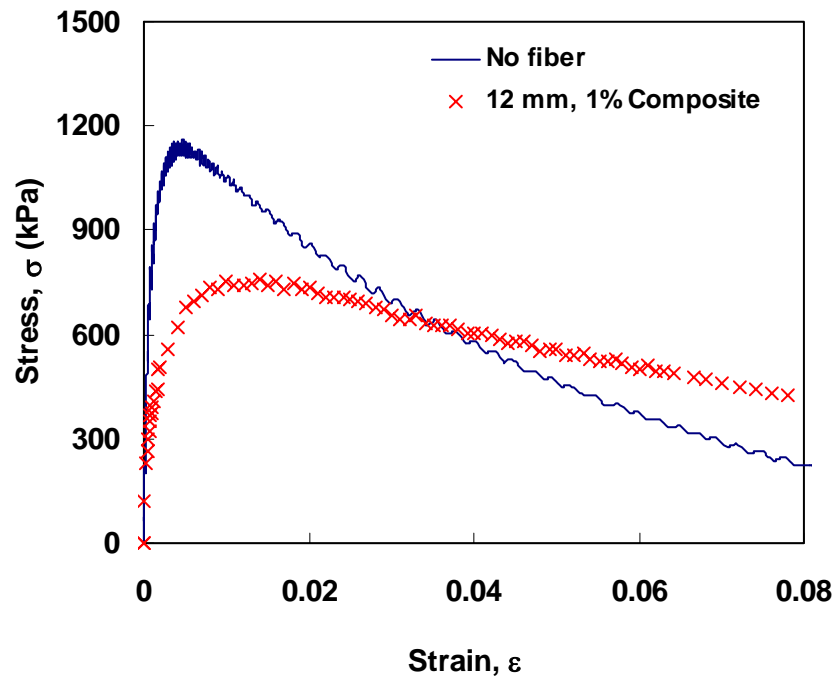


Figure 7.9 Tensile Stress-Strain Curve for a Fresh and a Fiber Composite (12 mm L_f , 1% V_f) Specimen

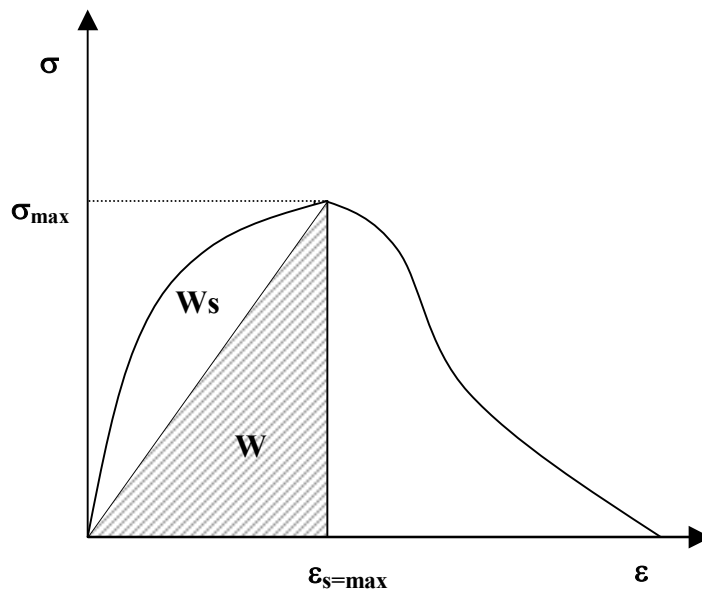


Figure 7.10 Schematic for Work Potential Theory

It is important that the resistance of asphalt concrete to fatigue cracking can be quantified through resistance to structural deformation using strain energy and/or damage using dissipated energy. The resistance to fatigue cracking of an elastic material is better because most of the work is subject to deforming the material prior to fracture. Thus, it was observed by Wen (2001) that the total energy, the sum of strain energy and dissipated energy, worked as a good indicator for the resistance of asphalt concrete to fatigue cracking. This total energy was referred as “*Fracture Energy*” according to Wen. Figure 7.11 represents the rank in total energy of the composite AC mix. As a result, the total energy of 8.5 kPa for the fiber reinforced AC specimens with 12 mm of fiber length (L_f) and 1% of fiber volume fraction (V_f) is approximately 85% larger than 4.6 kPa of fresh aspect concrete. Interestingly enough, as shown in Figure 7.12, the magnitude of dissipated energy of 12 mm of L_f and 1% of V_f composite increased 89% higher than that of specimens of 1.8 kPa without fibers and approximately 82% higher in the magnitude of strain energy. Table 7.2 summarizes data measured for IDST investigation. Figure 7.13 provides the relationships between fatigue cracking and fracture energy (Wen, 2001), which consists of strain energy and damage energy. This regression analysis is based on the amount of fatigue cracking at 5 million ESALs and fracture energy is obtained from IDST at a rate of ram movement 50.8 mm per minute at 20°C.

Table 7.2 IDST Resulted Data

Fiber Length, L_f (mm)	Volume Fraction, V_f (%)	Tensile Strength, σ_{max} (kPa)	Fracture Energy, W_T (kPa)	Strain Energy, W_s (kPa)	Damage Energy, W (kPa)
No Fiber	0	1029	4.57	1.82	2.75
	0.25	997	6.44	2.62	3.82
12	0.5	963	7.13	2.88	4.25
	1	849	8.47	3.41	5.06
	0.25	928	6.03	2.42	3.62
6	0.5	1013	7.18	2.93	4.25
	1	891	6.52	2.61	3.90

Note: Bold letters present the maximum values

A simultaneous statistical analysis was performed to evaluate the effect of two factors, a length (L_f) and a volume fraction (V_f) of fibers, on composites regarding fracture energy. Table 7.3 shows the results of the pairwise comparison testing. The general linear method (GLM) procedure constructs a linear model according to the specifications in the MODEL statement, the CONTRAST statement enables custom hypothesis tests by specifying the multivariate hypothesis; $H_0: \mu_1 = \mu_2$. As a result, adding 12 mm fibers to 1% V_f had significant effects on increasing the fracture energy within the 99.8% confidence limit against no fiber composite. In the case of 6 mm fibers, the hypothesis was rejected in the 99.3% confidence level. The fracture energies of two composites of 6 and 12 mm fibers L_f with 1% V_f are significantly different with the 80.1% confidence limit. Thus, it is concluded that there is a statistically significant difference in the fracture energy by including 12 mm fibers of 1% V_f as apposed to asphalt concrete without fibers.

Table 7.3 Statistical Analyses for Fiber Effect

		Probability (Pr)					
	Length (mm)	6			12		
Length (mm)	Volume (%)	0.25	0.5	1	0.25	0.5	1
0	0	0.111	0.0116	0.0072	0.0213	0.0019	0.0017
6	0.25		0.1476	0.0955	0.1991	0.0601	0.0487
	0.5			0.7476	0.7692	0.1991	0.3076
	1				0.5783	0.5509	0.1991
12	0.25					0.1476	0.0955
	0.5						0.7476
	1						

Note: If $|t| > Pr$, reject H_0

The typical parameter used in indirect tension strength testing is the maximum tensile stress calculated using Eq. 7.3. Figure 7.15 shows the rank in this parameter of the seven mixes. Although the AC concrete without fiber inclusion resulted in the highest tensile strength of 1,029 kPa, according to Wen (2001), this parameter does not serve as a good indicator of resistance to fatigue cracking.

Finally, it is concluded that the reinforced specimens with fibers in 12 mm L_f and 1% V_f conditions showed the best fatigue cracking resistance among the seven fiber composite mixes evaluated.

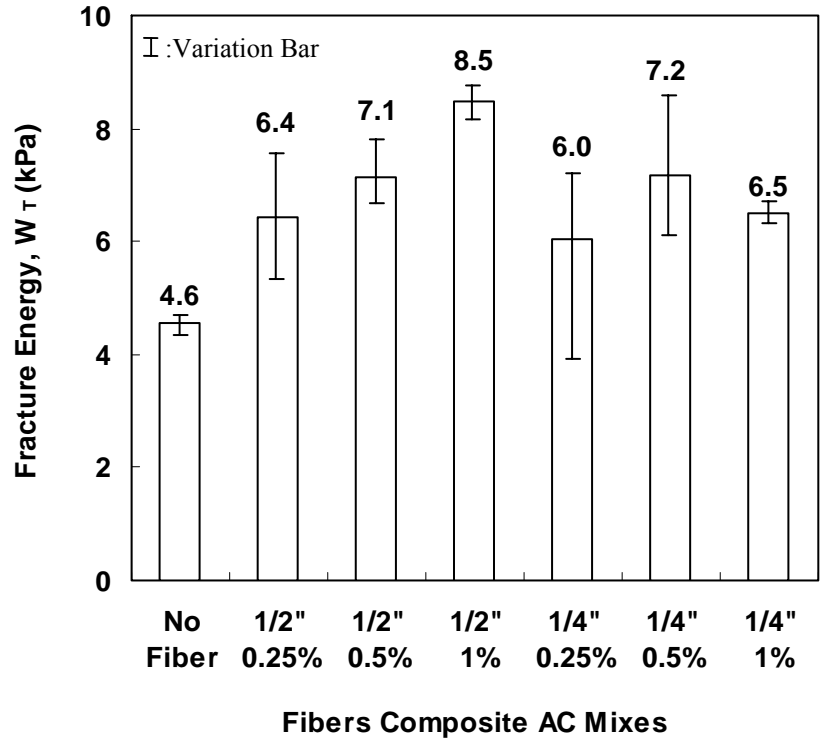


Figure 7.11 Total (or Fracture) Energy of Fiber Composite Asphalt Concrete

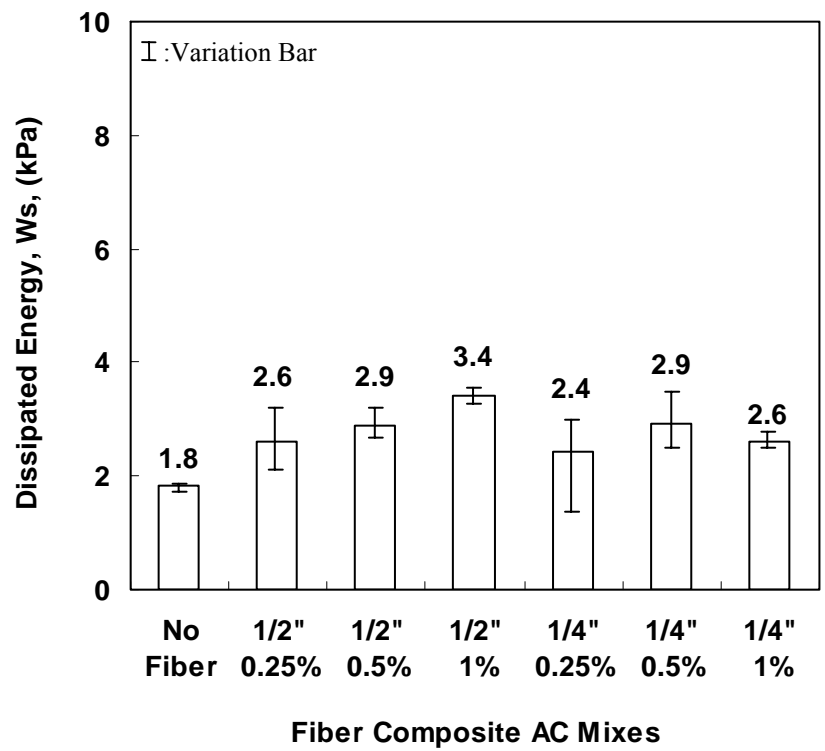


Figure 7.12 Dissipated Energy of Fiber Composite Asphalt Concrete

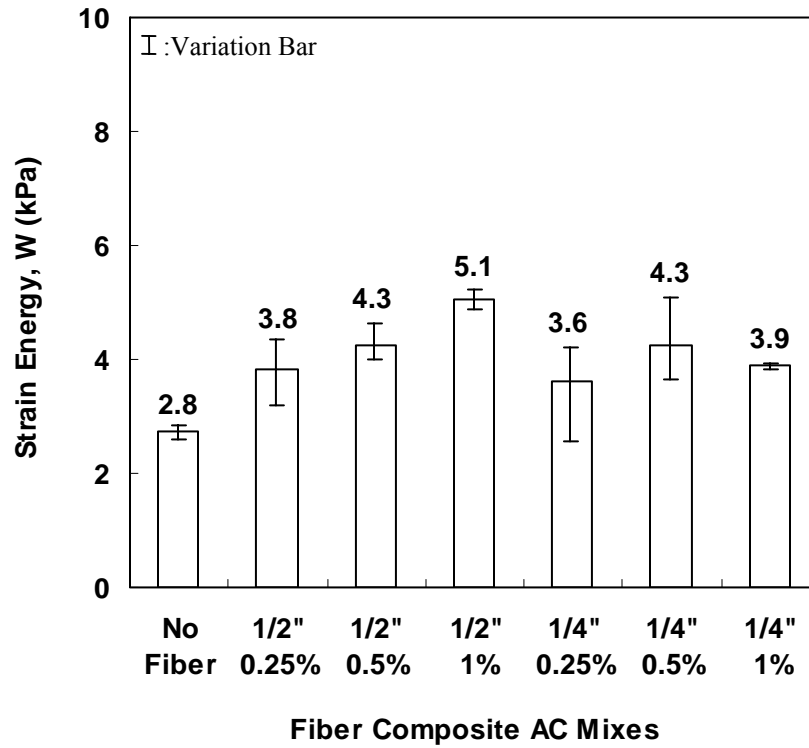


Figure 7.13 Strain Energy of Fiber Composite Asphalt Concrete

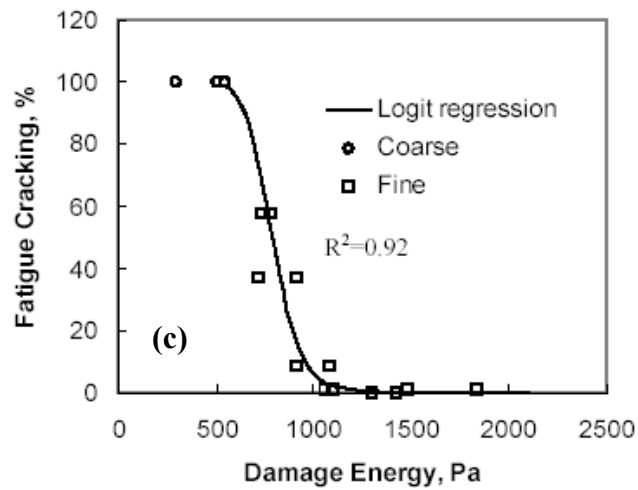
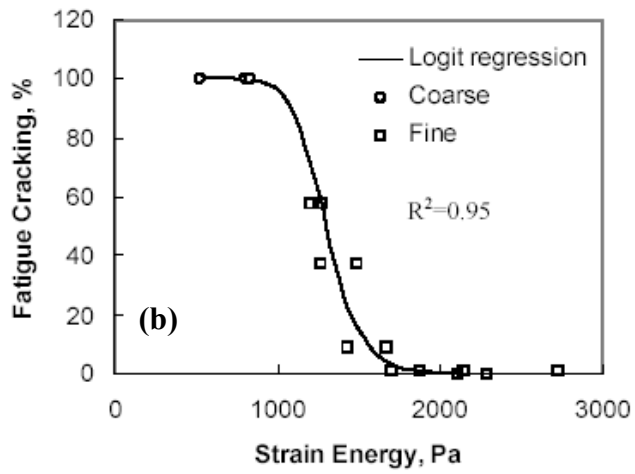
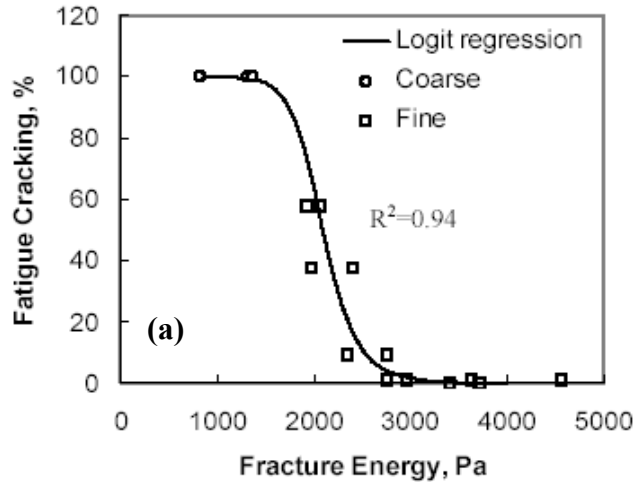


Figure 7.14 Relationships between Field Performance and Energy (Wen, 2001):

(a) Fracture Energy; (b) Strain Energy; and (c) Damage Energy

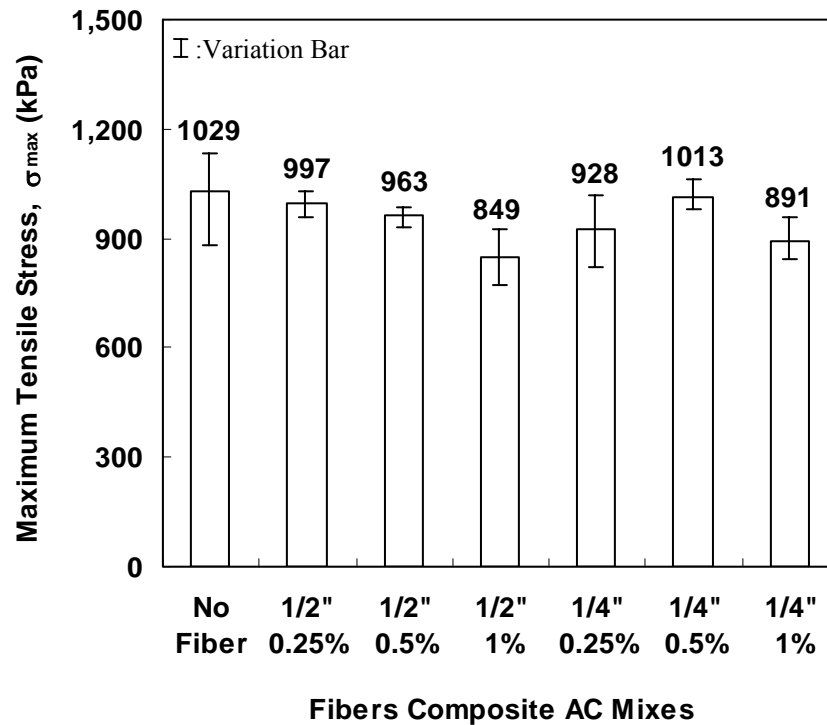


Figure 7.15 Maximum Tensile Stress of Fiber Composite Asphalt Concrete

7.6 SUMMARY

The critical embedded fiber length was shown to be approximately 9.7 mm, at which length a single nylon fiber started to rupture in pullout testing. Mechanical properties of fiber reinforced asphalt concrete demonstrated that fracture energy of 12 mm L_f and 1% V_f fiber reinforced concretes was larger than that of others. Thus, it is expected that this fiber condition shows the better crack resistance due to higher fracture energy.

CHAPTER 8

CONCLUSIONS AND RECOMMENDATIONS FOR FURTHER RESEARCH

8.1 CONCLUSIONS

Accelerated Pavement Testing (APT) using the third scale Model Mobile Loading Simulator (MMLS3) was performed to investigate both fatigue and rutting phenomena on model asphalt concrete pavements at N. C. State University. To accomplish the research objectives outlined in chapter 1, indirect tension tests and cyclic triaxial compression tests were incorporated. In addition, the fiber composite asphalt concrete study demonstrates the influence of fiber concentration and length on the fatigue crack resistance. Finally, performance prediction algorithms for fatigue and rutting behavior are proposed.

Once appropriate pavement construction technique and testing conditions including instrumentation were established, based on the data obtained from this study, the following conclusions are drawn for different performance measures:

Fatigue

1. The MMLS3 with wheel wandering system can induce realistic cracks fatigue (alligator pattern) on the asphalt concrete pavements with model structure. The model pavement layered structure consisted of an approximately 40 mm thick surface AC layer and a 75 mm neoprene rubber layer placed on a 25 mm thick steel plate. All model pavements in this configuration failed within 160,000 wheel applications (29 hours).

2. Using the wavelet correlation method (WCM), it was observed that during initial stages of loading, before visible cracking occurred at 12,000 wheel repetitions, in fatigue testing pavements showed a relatively high healing rate during rest periods. However, rest periods do not result in a greater magnitude of microdamage healing once macro-cracks have developed.
3. Damage growth of laboratory fatigue pavements including a thin (40 mm) AC layer can be evaluated using mechanical responses, such as tensile strain, phase velocity, and cracks, that are properly measured throughout the testing period. The change of stiffness of the AC layer, which decreases as the number of load cycles increases, was observed using WCM. Surface cracks arise when the phase velocity of pavement decreases to approximately 50% of that of the intact pavement.
4. Knowing that MMLS3 loading incorporates a wandering mechanism, pavement damage growth using linear cumulative damage theory was assessed employing a multi-layer elastic program, EverStress 5.0 program, and a fatigue life prediction model from the Asphalt Institute.
5. The algorithm for the fatigue life prediction of laboratory pavements during MMLS3 testing is established using IDT testing program. Once IDT program provides prediction model coefficients, k_1 and k_2 , and dynamic modulus, $|E^*|$, through cumulative damage analysis, k_3 in Eq. 5.19 is found using Asphalt Institute model.
6. Single nylon fiber pullout test, which is performed under loading condition of constant rate elongation at 20°C, can determine the critical fiber embedded length

from the observation of debonding and pulling behavior. A fiber rupture during a pullout test occurs on approximately 9.2 mm, or longer, fibers embedded in an AC binder.

7. Asphalt concretes containing nylon fibers can improve fatigue cracking resistance by increase of the fracture energy, a fundamental mechanical property through IDT strength tests. The fracture energy of the fiber composite asphalt concrete with fiber length of 12 mm and volume fraction of 1% increases about 85 % than that of fresh AC concretes.

Rutting

1. Accelerated pavement testing using the MMLS3 allows a rapid assessment of the rutting potential of 3 different asphalt mixtures under controlled conditions. Once pavement construction, composed of two lifts (60 mm each) of an AC layer and a steel plate, and testing method for rutting is effectively established, measured surface profiles is evaluated for rutting performance.
2. Using parametric study from Eq. 6.1 is capable to evaluate effect of material properties and testing conditions on performance:
 - “a” term increases by approximately 86% as the temperature was raised from 40°C to 55°C but “b” term increases only by 15% for RI1 mix;
 - “a” term does not show considerable variation to air void content, however, “b” increases approximately 22% as the air void content increases from 8.7% to 10.2% for I19C-A mix;

- Increase of aging period from 4 hours to 7 hours for I19C mix, “a” term decreases by approximately 39% but “b” term decreases only by 8%.
3. Cyclic triaxial compression testing program was incorporated to predict the permanent deformation of the MMLS3 tests. Once the prediction algorithm was formulated based on 4-layered pavement structure for I19C-A pavement, the developed algorithm successfully predicts rutting.

8.2 RECOMMENDATIONS FOR FURTHER RESEARCH

Future research is recommended to develop an easy-to-conduct test procedure that can improve the accuracy for measurement as well as analysis. The following recommendations are made concerning future research:

1. In AC layer construction, instead of current wood molds, steel compaction molds would be helpful for better control of model pavements density.
2. As described in Chapter 6, actual temperature measurements are crucial to predict rutting performance using the algorithm. It is recommended to install more thermocouples at different depth. Wireless temperature measurement may be available.
3. As for fiber reinforced asphalt concrete, even though the current research was used the available mix design regardless of fibers, the optimized mix design considering fiber inclusion will give better contribution to improve the fatigue cracking performance.

4. Indirect tension fatigue testing for fiber reinforced asphalt concrete enables to observe the influence of fibers on fatigue service life. Practically, nylon fibers from recycled carpets can be applicable to investigate the fatigue performance.

REFERENCES

ASTM Standard PS 131-01 (2001), *Standard Provisional Test Method for Bulk Specific Gravity and Density of Compacted Bituminous Mixtures Using Automatic Vacuum Sealing Method*, Philadelphia, USA

Beaudoin, J. J. (1990), *Handbook of Fiber-Reinforced Concrete – Principles, Properties, Developments and Applications*, Noyes Publications, Park Ridge, New Jersey, USA

Bentour, A. and S. Mindess (1990), *Fibre Reinforced Cementitious Composites*, Elsevier Science, New York, NY, USA

Bonaquist, R., J. and K. Stuart Sherwood (1998), *Accelerated Pavement Testing at the Federal Highway Administration Pavement Testing Facility*, Asphalt Paving Technology, Vol. 67, p 690-712

Brown, E. R., Kandhal, R. S. and Zhang, J. *Performance Testing for Hot Mix Asphalt*, NCAT Report No. 01-05

Chang, D. T., N. H. Ho, H. Y. Chang and H. S. Yeh (1999), *Laboratory and Case Study for Geogrid-Reinforced Flexible Pavement Overlay*, Transportation Research Record 1687, p 125-130

Epps, A.L., Ahmed, T., Little, D.C., and Hugo (2001), F., *Performance Prediction with the MMLS3 at WestTrack*, FHWA/TX-01/2134-1

Grant, E. L., W. G. Ireson, and R. S. Leavenworth (1982), *Principles of Engineering Economy*, 7th ed. John Wiley and Sons, Inc., New York

Harris, Bryan (1999), *Engineering Composite Materials*, 2nd Ed., IOM Communications Ltd., London

Hondros, G. (1959), *Evaluation of Poisson's Ratio and the Modulus of Materials of a Low Tensile Resistance by the Brazilian (Indirect Tensile) Test with Particular*, Austr. J. Appl. Sci., Vol. 10, No. 3, p 243-268

Huang, Yang H. (1993), *Pavement Analysis and Design*, Prentice-Hall, Inc., Englewood Cliffs, NJ

Huet, M., A. DE Boissoudy, J. C. Gramsammer, A. Bauduin, and J. Samanos (1990), *Experiments with Porous Asphalt on the Nantes Fatigue Test Track*, Transportation Research Record 1265, p 54-58

Hugo, F. (1994), *Some Factors Affecting the Design and Use of the Texas Mobile Load Simulator*, Vehicle-Road Interaction, ASTM STP 1225, American Society for Testing and Materials, Philadelphia, pp 67-88

Hugo, F., B.F. McCullough, and B. Van der Walt (1990), *Development of a Strategy for the Implementation of Full-Scale Accelerated Pavement Testing for the Texas Highway Department*, Research Report 1246-2F, Center for Transportation Research, The University of Texas at Austin, November

Jenq, Y. S., C. Liaw, and P. Liu (1993), *Analysis of Crack Resistance of Asphalt Concrete Overlays – A Fracture Mechanics Approach*, Transportation Research Record 1388, p 160-166

Jiang, Y. and R. S. McDaniel (1993), *Application of Cracking and Sealing and Use of Fibers to Control Reflective Cracking*, Transportation Research Record 1388, p 150-159

Kim, K. W., Y. S. Doh, and S. Lim (1999), *Mode I reflection cracking resistance of strengthened asphalt concretes*, Construction and Building Materials 13, p 243-251

Kim, S. M., Fredrick Hugo and Jose Roesset (1998), *Small Scale Accelerated Pavement Testing*, Journal of Transportation Engineering, Vol. 124, p 117-122

Kim, Y. Richard, J. S. Daniel, H. Wang (2001), *Fatigue Performance Evaluation of Westrack Asphalt Mixtures Using Viscoelastic Continuum Damage Approach*, N.C. Department of Transportation Final Report, Research Project No. HWY-0678

Kim, Yongon and Y. R. Kim (1996), *Evaluation of Microcrack Damage Growth and Healing of Asphalt Concrete Pavements Using Stress Wave Method*, Proceedings of Engineering Mechanics, Vol. 1, ASCE, p 612-615

Kwak, K. H. and Kim, J. J (1995), *Fatigue Strength in Polymer-Reinforced Concrete Beams under Cyclic Loading*, Nuclear Engineering and Design, Vol. 156, p 63-73

Leahy, R.B. and Witzak, M.W. (1991), *The Influence of Test Conditions and Asphalt Concrete Mix Parameters on Permanent Deformation Coefficients Alpha and Mu*, Journal of Association of Asphalt Paving Technologists, Vol.59.

McDaniel, Mark (1997), *Use of the MMLS to Investigate Fatigue of Asphalt Pavements at Low Temperatures*, Master's Thesis, University of Texas at Austin

Kim, Nakseok (1994), *Development of Performance Prediction Models for Asphalt Concrete Layers*, Ph.D. Dissertation, North Carolina State University

NCHRP Report 465, *Simple Performance Test for Superpave Mix Design*, National Research Council

NCHRP Synthesis 235 (1996), *Application of Full-Scale Accelerated Pavement Testing*, Transportation Research Board

Qi, X. and Witzzak, M. W., Time-dependent permanent deformation models for asphaltic mixtures, TRR 1639 pp 83-93

Road Transportation Research (1992), *Dynamic Loading of Pavements*, OECD, Paris

Romeo, R. A. and J. Perez (1992), *First Test on the Centro De Estudios de Carreteras Test Track*, Transportation Research Record, Washington D.C.

Roque, R. and Buttlar W.G. (1992), *The Development of a Measurement and Analysis Systems to Accurately Determine Asphalt Concrete Properties Using the Indirect Tensile Mode*, Proceedings, The Association of Asphalt Paving Technologist, p 304-333

Serfass, J. P. and J. Samanos (1996), *Fiber-Modified Asphalt Concrete Characteristics, Applications and Behavior*, The Association of Asphalt Paving Technologists, Vol. 65, p 193-230

Van Dijk, W. (1975), *Practical Fatigue Characterization of Bituminous Mixes*, The Association of Asphalt Paving Technologists, Vol. 44

Wang, Y., A.H. Zureick, B.S. Cho, and D.E. Scott (1994), *Properties of Fiber Reinforced Concrete Using Recycled Fibers from Carpet Industrial Waste*, Journal of Materials Science, Vol. 29, No. 16, p 4191-4199

Wang, Y., H.C. Wu and V.C. Li (2000), *Concrete Reinforcement with Recycled Fibers: A Review*, Journal of Materials in Civil Engineering, Vol. 12, No. 4, p 314-319

Wang, Y., S. Backer, and V.C. Li (1987), *An Experimental Study of Synthetic Fiber Reinforced Cementitious Composites*, Journal of Materials Science, Vol. 22, p 4281-4291

Wen, Haifang (2001), *Fatigue Performance Evaluation of WesTrack Asphalt Mixtures Based on Viscoelastic Analysis of Indirect Tensile Test*, Ph. D. dissertation, NCSU

Kim, NakSeok (1994), *Development of Performance Prediction Models for Asphalt Concrete Layers*, Ph.D. dissertation, NCSU

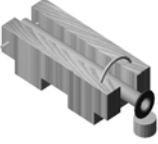


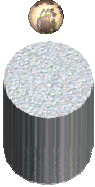

Barkdale, R.D. (1971), *Compressive Stress Pulse Times in Flexible Pavements for Use in Dynamic Testing*, Proceedings, Highway Research Board, Vol.345

APPENDICES

Appendix A

IMPACT METHOD AND GENERATED FREQUENCY RANGES FOR STRESS WAVE

Table A.1 Generated Frequency Ranges

Impact Devices	Impact Description	Frequency Band
	Spring operated impact stand device striking aluminum disk	5 ~ 8 kHz
	Spring operated wooden impact striking the asphalt slab	1 ~ 3 kHz
	.5567 kg fishing weight	0.1 ~ 0.5 kHz
	Marble impact on cylindrical steel	0.5 ~ 1 kHz 15 ~ 20 kHz
	200 mm tall marble stand	10 ~ 12 kHz

Appendix B

DYNAMIC MODULUS TEST

The frequency sweep test consists of a haversine loading applied to the specimen, as shown in Figure B.1. The load amplitude is adjusted based on the material stiffness, temperature, and frequency to keep the strain response within the linear viscoelastic range. The load is applied until steady-state is achieved, at which point several cycles of data are collected. The frequencies can be applied from the fastest to the slowest.

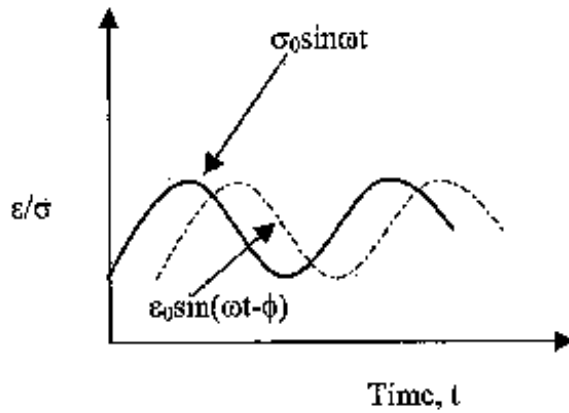


Figure B.1 Haversine Loading Pattern for Dynamic Modulus Test

From the frequency sweep test, the complex modulus, E^* , the dynamic modulus, $|E^*|$, and the phase angle, ϕ , can be determined. The complex modulus is composed of the storage and loss moduli in the following manner:

$$E^* = E' + iE'' \quad (\text{B.1})$$

where

E' = storage modulus,

E'' = loss modulus, and

$$i = (-1)^{1/2}$$

The dynamic modulus is the amplitude of the complex modulus and is defined as follows:

$$|E^*| = \sqrt{(E')^2 + (E'')^2} \quad (\text{B.2})$$

The values of the storage and loss moduli are related to the dynamic modulus and phase angle as follows:

$$E' = |E^*| \cos \phi \quad (\text{B.3})$$

$$E'' = |E^*| \sin \phi \quad (\text{B.4})$$

Figure B.2 shows the graphical relationship between all of these parameters. As the material becomes more viscous, the phase angle increases and the loss component of the complex modulus increases. Conversely, a decreasing phase angle indicates more elastic behavior and a larger contribution from the storage modulus. The dynamic modulus at each frequency is calculated by dividing the steady state stress amplitude (σ_{amp}) by the strain amplitude (ε_{amp}) as follows:

$$|E^*| = \frac{\sigma_{amp}}{\varepsilon_{amp}} \quad (\text{B.5})$$

The phase angle, ϕ , is related to the time lag, dt , between the stress input and strain response and the frequency of testing:

$$\phi = 2\pi f \Delta t \quad (\text{B.6})$$

where f is the loading frequency.

As the testing temperature decreases or the loading rate (frequency) increases the dynamic modulus will increase and the phase angle will decrease due to the time dependence or viscoelasticity of the material.

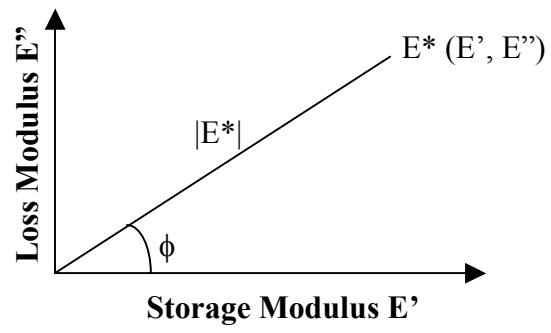


Figure B.2 Complex Modulus Schematic Diagram

Appendix C

FATIGUE FAILURE ANALYSIS

C.1 Cumulative Damage Analysis

Table C.1 8.9% Cumulative Damage Analysis Chart

position	Period		Strain	Total Wh	E* (MPa)	E* (psi)	sum(D _i)
	Total sec	905.70 wheel		111,532 Nfi	4473.71 Fraction	648,857 Ni	1.63 Di
0	15.52	25.87	101.10	140,960	0.029	3,185	0.023
10	14.37	23.95	124.20	104,210	0.026	2,949	0.028
17	17.62	29.37	140.50	86,956	0.032	3,616	0.042
24	18.43	30.72	155.50	74,926	0.034	3,783	0.050
25	19.32	32.20	157.40	73,602	0.036	3,965	0.054
29	17.83	29.72	164.70	68,863	0.033	3,659	0.053
33	37.55	62.58	170.80	65,284	0.069	7,707	0.118
38	36.47	60.78	176.80	62,057	0.067	7,485	0.121
42	37.38	62.30	180.20	60,346	0.069	7,672	0.127
46	38.09	63.48	182.20	59,376	0.070	7,818	0.132
50	38.74	64.57	182.90	59,043	0.071	7,951	0.135
54	38.09	63.48	182.20	59,376	0.070	7,818	0.132
58	37.38	62.30	180.20	60,346	0.069	7,672	0.127
62	36.47	60.78	176.80	62,057	0.067	7,485	0.121
67	37.55	62.58	170.80	65,284	0.069	7,707	0.118
71	17.83	29.72	164.70	68,863	0.033	3,659	0.053
75	19.32	32.20	157.40	73,602	0.036	3,965	0.054
76	18.43	30.72	155.50	74,926	0.034	3,783	0.050
83	17.62	29.37	140.50	86,956	0.032	3,616	0.042
90	14.37	23.95	124.20	104,210	0.026	2,949	0.028
100	15.04	25.07	101.10	140,960	0.028	3,087	0.022

Table C.2 9.8% Cumulative Damage Analysis Chart

	position	Period		cal. Str	Total Wh	E* (MPa)	E* (psi)	sum(D _i)
		Total	905.70		85957	4024.75	583,740	1.87
		sec	wheel		Nfi	Fraction	Ni	Di
1	0	15.52	25.87	107.90	81,780	0.029	2,455	0.030
2	10	14.37	23.95	132.90	64,144	0.026	2,273	0.035
3	17	17.62	29.37	150.60	55,446	0.032	2,787	0.050
4	24	18.43	30.72	166.90	49,186	0.034	2,915	0.059
5	25	19.32	32.20	169.00	48,475	0.036	3,056	0.063
6	29	17.83	29.72	176.90	45,961	0.033	2,820	0.061
7	33	37.55	62.58	183.60	44,012	0.069	5,940	0.135
8	38	36.47	60.78	190.10	42,263	0.067	5,769	0.136
9	42	37.38	62.30	193.70	41,349	0.069	5,913	0.143
10	46	38.09	63.48	195.90	40,808	0.070	6,025	0.148
11	50	38.74	64.57	196.70	40,615	0.071	6,128	0.151
12	54	38.09	63.48	195.90	40,808	0.070	6,025	0.148
13	58	37.38	62.30	193.70	41,349	0.069	5,913	0.143
14	62	36.47	60.78	190.10	42,263	0.067	5,769	0.136
15	67	37.55	62.58	183.60	44,012	0.069	5,940	0.135
16	71	17.83	29.72	176.90	45,961	0.033	2,820	0.061
17	75	19.32	32.20	169.00	48,475	0.036	3,056	0.063
18	76	18.43	30.72	166.90	49,186	0.034	2,915	0.059
19	83	17.62	29.37	150.60	55,446	0.032	2,787	0.050
20	90	14.37	23.95	132.90	64,144	0.026	2,273	0.035
21	100	15.04	25.07	107.90	81,780	0.028	2,379	0.029

Table C.3 10.4% Cumulative Damage Analysis Chart

	position	Period		Strain	Total Wh	E* (MPa)	E* (psi)	sum(D _i)
		Total	905.70		37697	3749.86	543,871	1.05
		sec	wheel		Nfi	Fraction	Ni	Di
1	0.00	15.52	25.87	112.70	57,750	0.029	1,077	0.019
2	10.00	14.37	23.95	139.00	47,178	0.026	997	0.021
3	17.00	17.62	29.37	157.70	41,773	0.032	1,222	0.029
4	24.00	18.43	30.72	174.90	37,805	0.034	1,278	0.034
5	25.00	19.32	32.20	177.20	37,332	0.036	1,340	0.036
6	29.00	17.83	29.72	185.50	35,720	0.033	1,237	0.035
7	33.00	37.55	62.58	192.50	34,467	0.069	2,605	0.076
8	38.00	36.47	60.78	199.40	33,317	0.067	2,530	0.076
9	42.00	37.38	62.30	203.30	32,700	0.069	2,593	0.079
10	46.00	38.09	63.48	205.60	32,348	0.070	2,642	0.082
11	50.00	38.74	64.57	206.40	32,227	0.071	2,687	0.083
12	54.00	38.09	63.48	205.60	32,348	0.070	2,642	0.082
13	58.00	37.38	62.30	203.30	32,700	0.069	2,593	0.079
14	62.00	36.47	60.78	199.40	33,317	0.067	2,530	0.076
15	67.00	37.55	62.58	192.50	34,467	0.069	2,605	0.076
16	71.00	17.83	29.72	185.50	35,720	0.033	1,237	0.035
17	75.00	19.32	32.20	177.20	37,332	0.036	1,340	0.036
18	76.00	18.43	30.72	174.90	37,805	0.034	1,278	0.034
19	83.00	17.62	29.37	157.70	41,773	0.032	1,222	0.029
20	90.00	14.37	23.95	139.00	47,178	0.026	997	0.021
21	100.00	15.04	25.07	112.70	57,750	0.028	1,043	0.018

Table C.4 10.4% Cumulative Damage Analysis

	position	Period		Strain	Total Wh	E* (MPa)	E* (psi)	sum(Di)
		Total sec	905.70 wheel		28872 Nfi	3451.94 Fraction	500,661 Ni	1.06 Di
1	0	15.52	25.87	118.40	39,118	0.029	825	0.021
2	10	14.37	23.95	146.40	33,511	0.026	763	0.023
3	17	17.62	29.37	166.30	30,538	0.032	936	0.031
4	24	18.43	30.72	184.60	28,300	0.034	979	0.035
5	25	19.32	32.20	187.00	28,035	0.036	1,026	0.037
6	29	17.83	29.72	195.80	27,111	0.033	947	0.035
7	33	37.55	62.58	203.30	26,378	0.069	1,995	0.076
8	38	36.47	60.78	210.70	25,700	0.067	1,938	0.075
9	42	37.38	62.30	214.80	25,341	0.069	1,986	0.078
10	46	38.09	63.48	217.20	25,137	0.070	2,024	0.081
11	50	38.74	64.57	218.10	25,061	0.071	2,058	0.082
12	54	38.09	63.48	217.20	25,137	0.070	2,024	0.081
13	58	37.38	62.30	214.80	25,341	0.069	1,986	0.078
14	62	36.47	60.78	210.70	25,700	0.067	1,938	0.075
15	67	37.55	62.58	203.30	26,378	0.069	1,995	0.076
16	71	17.83	29.72	195.80	27,111	0.033	947	0.035
17	75	19.32	32.20	187.00	28,035	0.036	1,026	0.037
18	76	18.43	30.72	184.60	28,300	0.034	979	0.035
19	83	17.62	29.37	166.30	30,538	0.032	936	0.031
20	90	14.37	23.95	146.40	33,511	0.026	763	0.023
21	100	15.04	25.07	118.40	39,118	0.028	799	0.020

C.2 MATHEMATICAL EXPRESSION OF N_f FOR MMLS3 SYSTEM

$$N_{fi} = k_1 \varepsilon_i^{-k_2} |E^*|^{k_3}$$

$$\rho_i = \frac{\text{Number of loading at } i^{\text{th}} \text{ station in wandering period}}{\text{Total number of loading in one period (= 905.70)}}$$

$$\sum_{i=1}^{21} (\rho_i) = 1$$

$$N_i = N_f \cdot \rho_i$$

At failure,

$$\text{Damage Ratio (D)} = \sum_1^{21} D_i$$

$$\sum_{i=1}^{21} \frac{N_i}{N_{fi}} = 1$$

$$\sum_{i=1}^{21} \frac{N_f \rho_i}{N_{fi}} = \sum_{i=1}^{21} \frac{N_f \rho_i}{k_1 \varepsilon_i^{-k_2} |E^*|^{k_3}} = 1$$

So,

$$N_f = \frac{1}{\sum_{i=1}^{21} \frac{\rho_i}{k_1 \varepsilon_i^{-k_2} |E^*|^{k_3}}}$$

C.3 MATHEMATICAL EXPRESSION OF k_3 FOR MMLS3 SYSTEM

N_f (in algorithm) = N_f (in Asphalt Institute Model)

$$\frac{1}{\sum_{i=1}^{21} \frac{\rho_i}{k_1 \cdot \varepsilon_{ti}^{-k_2} |E^*|^{k_3}}} = \frac{1}{\sum_{i=1}^{21} \frac{\rho_i}{C \cdot f_1 \cdot \varepsilon_{ti}^{-f_2} |E^*|^{f_3}}}$$

$$\frac{k_1 |E^*|^{k_3}}{\sum_{i=1}^{21} \frac{\rho_i}{\varepsilon_{ti}^{-k_2}}} = \frac{C f_1 |E^*|^{f_3}}{\sum_{i=1}^{21} \frac{\rho_i}{\varepsilon_{ti}^{-f_2}}}$$

$$|E^*|^{k_3} = c \left(\frac{f_1}{k_1} \right) \left(\frac{\sum_{i=1}^{21} \frac{\rho_i}{\varepsilon_{ti}^{-k_2}}}{\sum_{i=1}^{21} \frac{\rho_i}{\varepsilon_{ti}^{-f_2}}} \right) |E^*|^{f_3}$$

$$k_3 \log |E^*| = \log(C) + \log\left(\frac{f_1}{k_1}\right) + \log\left(\frac{\sum_{i=1}^{21} \frac{f_i}{\varepsilon_{ti}^{-k_2}}}{\sum_{i=1}^{21} \frac{f_i}{\varepsilon_{ti}^{-f_2}}}\right) + f_3 \log |E^*|$$

$$k_3 = \frac{1}{\log |E^*|} \left[\log(C) + \log\left(\frac{f_1}{k_1}\right) + \log\left(\frac{\sum_{i=1}^{21} \frac{f_i}{\varepsilon_{ti}^{-k_2}}}{\sum_{i=1}^{21} \frac{f_i}{\varepsilon_{ti}^{-f_2}}}\right) \right] + f_3$$

Appendix D

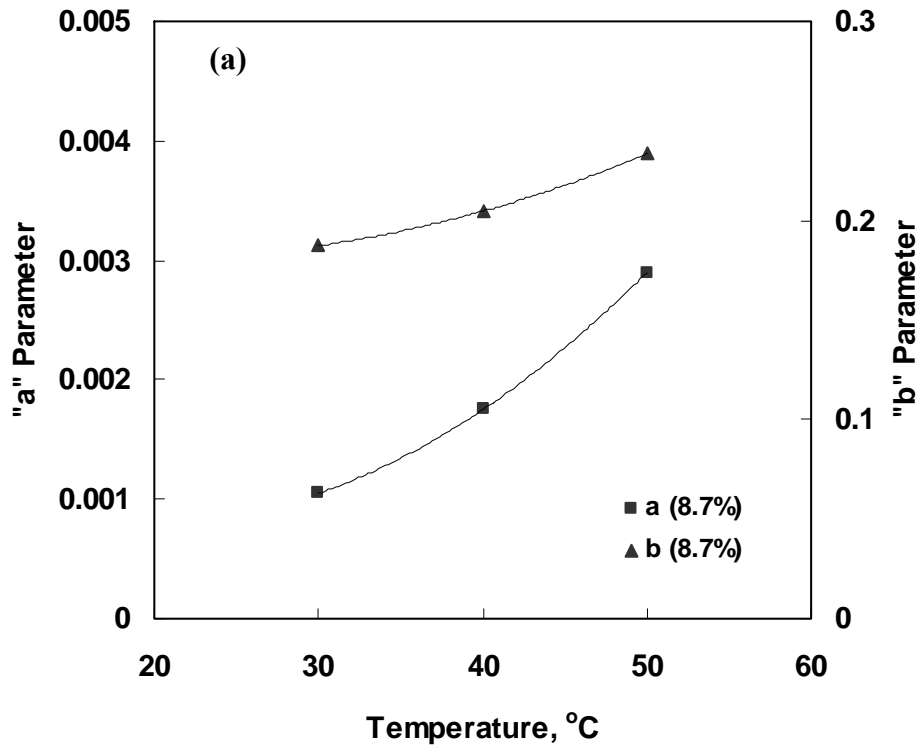
PERMANENT DEFORMATION REGRESSION PARAMETER DETERMINATION

From the triaxial testing program in ranges of temperatures: 50°C, 40°C, and 30°C, parameters, “a” and “b”, can be determined as a function of air void content and temperature.

- $a = 0.0036553841 + 0.0000045846 AV \times T - 0.0002113755 T + 0.0000031389 T^2$
- $b = -0.1529731289 + 0.0002866283 AV \times T + 0.0132840242 T - 0.0001671877 T^2$

Note: T stands for temperature

AV stands for air void content



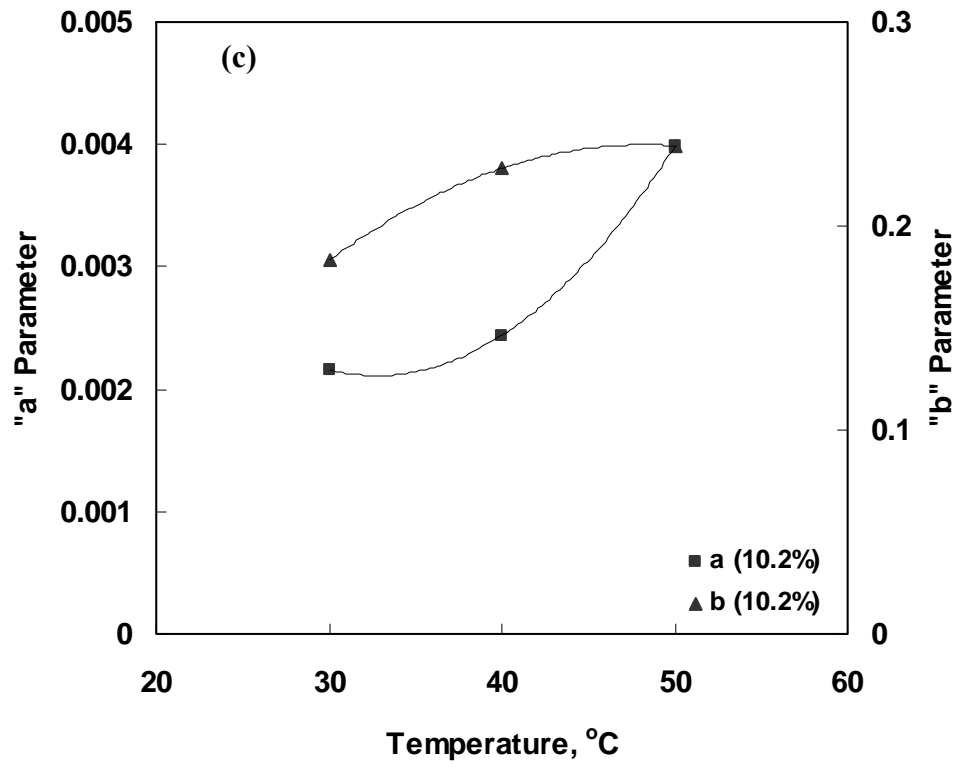
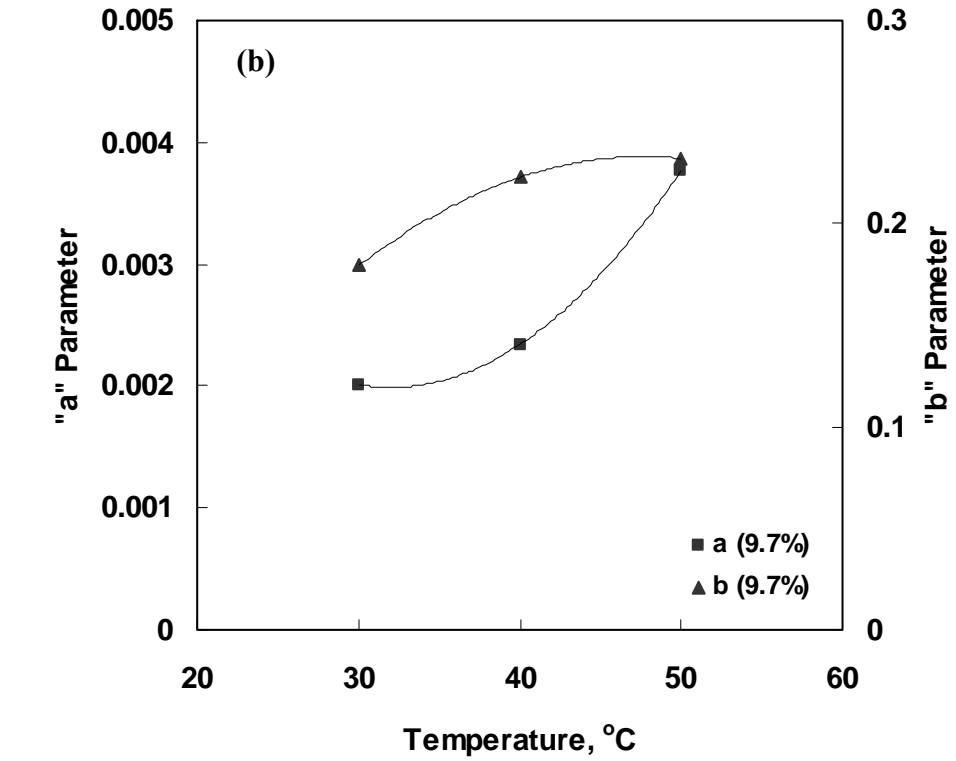


Figure D.1 Relationships between Temperatures and Parameters at Air Void Contents of: (a) 8.7%, (b) 9.7%, and (c) 10.2%